Delft University of Technology

Trapped-Victim Detection
in Post-Disaster Scenarios using Ultra-Wideband Radar

Amer Nezirović

International Research Centre for Telecommunications and Radar,
Faculty of Electrical Engineering, Mathematics and Computer Science,
Delft University of Technology,
Delft, The Netherlands.

Trapped-Victim Detection
in Post-Disaster Scenarios using Ultra-Wideband Radar

PROEFSCHRIFT

ter verkrijging van de graad van doctor
aan de Technische Universiteit Delft,
op gezag van de Rector Magnificus prof. ir. K.C.A.M. Luyben,
voorzitter van het College voor Promoties,
in het openbaar te verdedigen
op 10 maart 2010 om 10.00 uur

door

Amer NEZIROVIĆ

Master of Science in Electrical Engineering,
Kungliga Tekniska Högskolan, Zweden
geboren te Doboj, Bosnië en Herzegovina.

Dit proefschrift is goedgekeurd door de promotoren:

Prof. dr. ir. L.P. Ligthart
Prof. dr. sci. A.G. Yarovoy

Samenstelling promotiecommissie:

Rector Magnificus	voorzitter
Prof. dr. ir. L.P. Ligthart	Technische Universiteit Delft, promotor
Prof. dr. sci. A.G. Yarovoy	Technische Universiteit Delft, promotor
Prof. dr.-ing. habil. R.S. Thomä	Technische Universität Ilmenau
Prof. dr. ir. F. le Chevalier	Technische Universiteit Delft
Prof. ir. P. Hoogeboom	Technische Universiteit Delft
Dr. habil. K. Witrisal	Technische Universität Graz

SUPPORT
The research for this thesis was financially supported in part by the FP6 STREP project EUROPCOM (IST-004154) and in part by the Radiotect project (COOP-CT-2006-032744).

Typesetting system: LaTeX.
Printed in The Netherlands by Ipskamp Drukkers BV, Enschede.

ISBN/EAN: 978-94-6113-001-3

Author e-mail: amer_nezir@hotmail.com

Dedicated to my family

Contents

1 Introduction

Collapse of man-made structures, such as buildings and bridges, occur with varying frequency across the world. In such a case, survived human beings are often trapped in the cavities created by collapsed building material. Common cause of such collapses is overload due to faulty construction, faulty design, fire, gas explosions, terrorist acts, but the single most common and devastating cause of collapse of man-made structures is earthquake. Large-scale earthquakes with magnitudes larger than 7.0 on the Richter scale often result in more or less severe damage to buildings. The United States Geological Survey (USGS) estimates that, since 1900, there have occurred an average of 18 major earthquakes (magnitude 7.0-7.9) and one great earthquake (magnitude 8.0 or greater) per year, and that this average has remained relatively stable [1]. Although some of the causes of collapse of man-made structures can be reduced in the foreseeable future, they cannot be fully eliminated, particularly not the magnitude and the frequency of earthquakes. Thus, the case of trapped victims buried under rubble is a continuous threat that the mankind has to cope with.

1.1 Urban search-and-rescue (USAR)

In situations of survivors trapped under piles of rubble, urban search-and-rescue (USAR) crews have a very limited or no knowledge on the presence and location of the survivors [2]. The approach to localise trapped victims consists of three major steps. The first step is to conduct an extensive and detailed on-site gathering of all the relevant information from the local authorities, survivors, witnesses etc, which is later used for further USAR planning. The second step is to perform a confined-area search using specially trained USAR dogs, typically three in number. If at least two dogs mark a presence of a human being buried under rubble, the USAR crew needs to localise the victim. The dogs cannot provide the USAR crew reliable enough information on the location of the victim, due to the possibility of the scent of the victim being registered at another location than straight above the actual one. Therefore, the USAR crews need

to rely on other tools.

The most common and efficient approach so far has been to implement highly sensitive audio devices which are placed in direct contact with the rubble and listen for any sound coming from the trapped victim(s) [3].

Another very common way is to use combined audio-visual equipment that is inserted into the rubble. Such equipment consists of a highly sensitive microphone, a video camera and a flashlight, all mounted on a thin rod. The information picked up by the microphone and the camera is passed to an operator that makes judgment on the possible location of the victim. However, this last step in a typical trapped-victim detection operation is inaccurate, tedious, prone to strong audio interference and is further time- and labour consuming [3].

A third possibility involves localisation of the radiated electromagnetic energy coming from the cellular phone belonging to the victim. This approach, however, is only viable if there is enough power in the battery of the cellular phone. Furthermore, is does not guarantee that the victim is still alive nor that the cellular phone is actually carried by the victim.

Due to various shortcomings of all mentioned approaches so far, there is a strong need for implementation of a method for a safe, reliable, time- and labour-efficient, and most importantly, more exact estimation of the location of trapped victims.

1.2 Radar-based trapped-victim detection

Radar is considered to be a solution to the problem of efficiently, accurately and reliably detecting and locating victims buried under rubble [4]. Since time is a crucial factor, the priority during such trapped-victim detection is given to detecting living victims. The operational mode of a search-and-rescue radar is to generate and radiate electromagnetic energy into the rubble and from the received backscattered radiation extract any motion produced by the victim. A typical radar-based trapped-victim detection scenario is depicted in fig. 1.1.

1.2.1 Priorities during radar-based trapped-victim detection operations

The trapped victims can be divided into two types. The first type of victims are conscious and are able to make their location known either by responding to the USAR crew or slamming the surrounding rubble with their fists and possibly even with their feet. For these types of victims, generally the use of search-and-rescue radar is deemed unnecessary since the location of the victim can be performed by simply listening to the sound produced by the victim. The second type of trapped victims comprises those that are unable to respond or give away their location, due to their weak medical state, or those that are simply unconscious. For such scenarios, the most feasible approach to victim

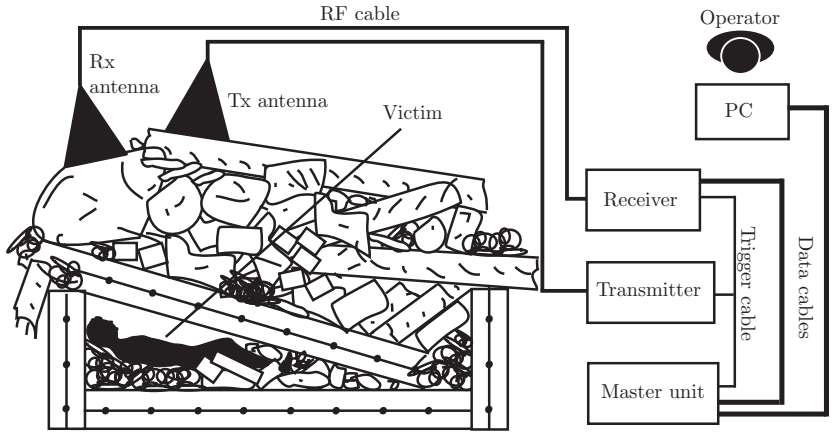

Figure 1.1: *Typical set-up during post-disaster trapped-victim detection operation using radar*

detection is to extract the only motion that is produced by an unconscious victim: respiratory- and cardiac motion.

1.2.2 Victim detection and challenges during radar-based trapped-victim detection operations

Radar-based motion detection is based on extracting changes in frequency, phase and arrival time of the backscattered response from the victim. The response from the victim is hidden in the reflections from stationary objects, or clutter, which can be orders of magnitude stronger, as well as hidden in the background noise [4]. In addition, one is very often faced with the presence of non-stationary clutter, which has two distinctly different origins:

- amplitude instability of the data acquisition equipment,
- motion of rescue workers, rescue dogs, heavy machinery, rattling leaves due to wind etc.

On top of that, depending on the operational frequency band, the acquired data could potentially be contaminated with narrowband interference from various radio sources, such as TV, radio, emergency radio etc.

1.2.3 Narrowband radar and its deficiencies

There are two different types of radar technology that have so far been used for the purpose of USAR: narrowband radar and ultra-wideband (UWB) radar. Narrowband radars can further be divided into two types:

- interferometric radar, which is a continuous wave radar technology, measures the phase shift between transmitted and received signals and extracts periodic modulation of this phase shift due to respiratory- or cardiac motion. Due to its zero bandwidth, it is solely capable of providing an indication on the presence of a trapped victim and not its range [5].

- Pulse-Doppler radar. Such radar technology measures the Doppler effect by using a coherent train of pulses where there is a fixed phase relationship between the carrier frequency between each successive pulse. The phase (frequency) shift $\Delta\phi$ (according to the Doppler effect), which is proportional to the radial velocity of the human chest:

$$v(\Delta\phi) = \frac{\Delta\phi \; c \; \text{PRF}}{4\pi f_o} \qquad \Delta\phi \in [-\pi, \pi) \tag{1.1}$$

  where PRF is the pulse repetition frequency, f_o is the operational frequency of the radar and c is the propagation speed of the electromagnetic waves inside the rubble.

In the case of narrowband radar, the use of a relatively small bandwidth results in poor down-range resolution (with limited capability of discriminating between two closely spaced targets) and inability to accurately determine the range of the victim. Due to the same reason, it is not capable of separating target from various sources of non-stationary clutter. Lastly, it is considered very sensitive to narrowband interference, in case the respective operational frequency bands of radar and interferer overlap. In order to mitigate the deficiencies of narrowband search-and-rescue radar, one needs to consider UWB technology, which is described below.

1.3 Ultra-wideband technology and its application in radars

UWB is a promising technology which has been implemented so far for various purposes and fields, for instance, automotive collision-detection systems, wireless communications, indoor positioning, sensor networks etc. According to the Federal Communications Commission (FCC) [6], devices implementing UWB technology would be required to have a -10 dB bandwidth $B_{\text{-10dB}} > 500$ MHz or fractional bandwidth $B_{fr} = 2 \cdot \frac{(f_h - f_l)}{(f_h + f_l)} > 0.2$, where f_l is the lower frequency at -10dB level and f_h is its higher equivalent.

1.3.1 UWB radar

According to the FCC "UWB technology can be employed for radar systems, permitting the precise measurement of distances, the detection of objects within

a defined range of distances, or high resolution imaging of objects that are behind or under other surfaces" [6]. UWB technology has been successfully implemented in radar, since it provides the necessary bandwidth for resolution of closely spaced scatterers and generally does not experience the deficiencies of the narrowband radar. It has so far been implemented in particular in ground-penetrating radar (mine- and utility detection, forensic search, archeology) [7], as well as for through-wall radar applications (security and surveillance) [8], monitoring of respiratory motion of patients in hospitals [9] etc. Due to its large potential, it is therefore the considered radar technology for UWB-radar-based trapped-victim detection in this PhD thesis. There exist four types of UWB radars which achieve ultra-wide bandwidth by various means:

- **Stepped-Frequency Continuous Wave (SFCW) radar** transmits a sequential series of individual frequencies whose amplitude and phase are accurately known.
- **Frequency-Modulated Continuous Wave (FMCW) radar** transmits a chirp signal, which is a continuous wave signal whose frequency is gradually increased to cover the desired bandwidth.
- **Pseudo-random noise radar** achieves ultra-wide bandwidth by periodically transmitting sequences consisting of pulses with pseudo random polarity and performing correlation in the receiver with the transmitted sequence.
- **Time-domain impulse radar** transmits ultra-short pulses (thus obtaining ultra-wide bandwidth) with a fixed pulse repetition frequency.

It is worth mentioning that the methods of achieving ultra-wide bandwidths for the first two UWB radar technologies are commonly implemented also in narrowband or wideband radar, while the last two methods are typically associated with UWB radar only.

1.3.2 Advantages of using UWB radar for trapped-victim detection

The advantages of UWB radar over narrowband radar are listed below [10]:

- UWB radar exhibits very fine range resolution due to its large bandwidth, resulting in its ability to separate individual multipaths originating from various scatterers in the scene. This enables extraction of target features which are much smaller than the target size (e.g. respiratory motion), as well as resolving two or several closely located victims. Furthermore, due to its large bandwidth, it allows for increased separation of the target response from the non-stationary clutter responses compared to narrowband radar.

- Typical power transmission levels for short-range UWB radar systems are in the milliwatt range, although levels in the watt range are not uncommon. This leads to minor if any effects on crucial radio services, such as emergency radio.

- High tolerance to external narrowband interference, depending on the UWB radar technology.

1.3.3 Challenges faced in using UWB radar for trapped-victim detection operations

The challenges that are commonly faced in using UWB radar for trapped-victim detection operations and the conventional solutions to mitigate the problems are presented below:

Low signal-to-noise ratio conditions

One of the main challenges faced in trapped-victim detection operations using UWB radar (but not limited to UWB radar only) is the fact that the SNR conditions are generally low. There are multiple reasons for low SNR conditions:

- The spectral power levels are typically lower than for narrowband radar.

- A tiny fraction of the transmitted pulse energy penetrates the rubble, reflects from the human body, passes through the rubble again and is registered by the receive antenna. It may also be subject of attenuation in the order of tens of decibels.

- Analogue-to-digital converters (ADC) employed in time-domain UWB radar typically use lower number of bits and therefore possess lower dynamic range than in the case of narrowband radar.

- Sampling of UWB signal returns requires a high sampling frequency, which, for this application, cannot be realised by using real-time sampling due to too high requirements on sampling speed and digitisation accuracy. Non-optimal sampling methods are then employed, which reduce the highest possible value of coherent averaging. This then leads to a further increase in noise floor and thereby further decrease in SNR.

- Displacement of the chest of the victim due to respiratory- or cardiac motion results in specific responses in the processed data set. Such responses are used as the only target feature that enable detection of a trapped victim. As such, the magnitude of such responses is significantly lower than that of the backscattered responses from the chest of the victim.

- The magnitude of the motion responses of the victim are dependent on the position and orientation of the victim with respect to the receive and transmit antennas. Certain body positions can produce significantly lower magnitudes of motion responses compared to other positions.

A common practice in the approach to improve the SNR conditions is to perform matched filtering at the receiver side. The matching filter waveform should be highly correlated with the waveform of the motion responses of the victim. Unfortunately, due to a strong frequency dependency of the transmission coefficient of the rubble material as well as the reflection coefficient of the human body, the received waveform of the motion responses differs significantly from the radiated waveform. This makes the matched filtering operation highly impractical without appropriate pre-processing of the waveforms.

Narrowband interference

It has been observed that UWB radar is prone to external, non-stationary, narrowband interference. The level of interference to the system depends on the UWB radar technology, the carrier frequency and bandwidth of the NBI, as well as the resulting signal-to-interference-ratio. In the case of impulse radar, the narrowband interference can be (partially) randomised into coloured Gaussian noise (depending on the sampling frequency), thereby reducing the SNR conditions. A common approach to reduce the effect of the narrowband interference is to implement an analogue notch filter in front of the ADC, tuned to the carrier frequency of the interferer. This, however, results in ringing of the motion response waveform, which then reduces the down-range resolution of the system.

Non-stationary clutter and residues

The backscattered responses from the victim are overlapped with clutter which can be orders of magnitude stronger. Stationary clutter is a large source of interference; it therefore needs to be removed in order to obtain the motion responses of the victim. Although the stationary clutter can be removed in a straightforward manner, there is nevertheless commonly a presence of unwanted responses, which can result in false alarms or missed detection. The unwanted responses can be divided into:

- Residues originating from instability in the equipment.
- External non-stationary clutter originating from motion of leaves in nearby bushes and trees, motion of rescue workers and the radar operators, loose reinforcement bars (rebars) on the pilse of rubble, operating excavation equipment in the vicinity and slight motion of the antennas or propagation cables due to strong wind.

One approach to mitigate the effect of non-stationary clutter is to set the unambiguous range larger than the range at which the non-stationary clutter occurs. By means of range gating (ignoring farther ranges) one can then typically avoid such sources of interference. Another is to consider a frequency range in which it highly likely that the target responses are located. Despite such measures, though, the unwanted responses persist, both in range and frequency range of interest.

Spectral power emission and its regulation

If the necessity to comply with spectral emission regulations is taken into account, the spectral power and allowed bandwidth are strictly limited by a spectral emission mask. For non-licensed UWB radar surveillance systems, FCC regulations state that the spectral power should not exceed -41.3 dBm/MHz in the 2-11.6 GHz frequency range [6]. Aside from the regulatory issues, the solution to the problem of typically low SNR conditions is not simply to increase the transmit power. The following consideration should be taken into account:

- At present, there is a practical limit on the achievable transmit power for a given bandwidth and time of waveform generation in impulse radar.
- The dynamic range of the receiver might not support increased transmit power, due to strong cross-talk between the transmit and receive antenna. This commonly results in time-instability of the equipment and thereby unwanted responses. Only limited reduction of cross-talk can be achieved since perfect shielding is practically impossible to achieve.
- It is desirable to minimise interference originating from the UWB signals into the frequency-overlapping radio communication services in the vicinity, in particular emergency radio (e.g. Tetra).
- The magnitude of non-stationary clutter is proportional to the transmit power.
- The magnitude of the useful signal energy highly depends on the magnitude of the observed motion of the victim.

Although the effects of the first three points stated above can very well be mitigated and improved in future (which is out of the scope of the research presented in this thesis), it is nevertheless important to emphasise the limitation of practically achievable transmit powers in UWB radar systems of today. It is expected that in the future there would be more room for improvement of SNR conditions during UWB-radar-based trapped-victim detection operations simply by increasing the transmit power. But as long as the abovementioned issues remain unsolved, increasing transmit power does not represent a simple and final solution to increasing the general SNR conditions.

Discrimination capabilities of closely spaced victims

Another issue in any radar-based trapped-victim detection operation is the potential difficulty when discriminating between two closely spaced victims that might be separated by a concrete slab. It might be particularly problematic to deal with the masking effect of the first victim on the second one in case they are aligned in the boresight direction. A common solution to solve such problem is to implement a multi-static radar mode (a radar that make use of several receive and/or transmit antennas). It is worth adding that this issue is even more problematic for narrowband radar that experiences lower down-range resolution.

1.3.4 State of the art

At the start of the research studies presented herein, there were several research groups that have been previously involved in the field of human being (respiratory and, in some cases, heartbeat) detection. This section briefly highlights the approach and the outcome of their research, but also points out their respective deficiencies, which altogether give ground for motivation of the research presented herein.

- One of the pioneers of human being detection using UWB radar is Staderini of Tor Vergata University of Rome, Italy [9]. He has demonstrated the use of UWB radars in medicine, for non-intrusively monitoring the respiratory and heart beat of a patient in a hospital bed [11]. The radar is placed above the patient's bed under line-of-sight (LOS) conditions. With their radar they have demonstrated the possibility of not only respiratory monitoring but also remote cardiography, i.e. heart-beat monitoring. Despite the publicity that this work has incurred, it cannot be seen as a particularly useful work for study of UWB-radar-based detection of victims buried under rubble, as the latter scenario is fundamentally different and presents considerable number of additional challenges.

- One of the first elaborate studies on the development of a victim detection radar was performed by Haddad at the Lawrence Livermore National Laboratory in 1997 [12]. The developed system was an impulse radar operating at the centre frequency of 2 GHz and having a bandwidth of 2-3 GHz. The approach to respiratory motion detection was based on observing the respiratory motion responses at the expected respiratory frequency. The system was tested using a reinforced concrete slab and a large sewage pipe in which the test person was placed. The research presented therein can be characterised as a feasibility study of detecting humans under rubble, the results of which, although reasonably satisfactory for that time, cannot be regarded as state-of-the-art of today.

- Ossberger et al. of the Johannes Kepler University in Linz, Austria, have presented a method for through-wall vital parameter detection using an UWB pulse radar [13]. In their experimental verification the group considered a scenario where a person was standing behind a 20 cm brick wall and facing the radar. However, this study is performed in highly idealistic conditions and differs strongly from radar for trapped-victim detection (20cm brick wall and standing test person).

- The group under Immoreev from Moscow Aviation Institute, has presented similar results, both for line-of-sight (LOS) and non-line-of-sight (NLOS) conditions [14]. Experimental verification demonstrated the possibility to detect respiratory motion of a person standing behind a 45 cm thick brick wall. The radar was located at the other side of the wall at a distance of about 1 m from it. The range of the radar is 0.1-3 m and its estimated range resolution is 50 cm. Although the conditions are slightly more realistic for trapped-victim detection, nevertheless, the main objective of the research is to perform a feasibility study on respiratory detection of a concealed standing person. Furthermore, it was obvious from the provided radiograms that the SNR conditions are considerably higher than in the case of using an UWB radar for detection of a buried victim.

- Geozondas Ltd. and the International Research Center for Telecommunications and Radar (IRCTR) jointly developed a human being detection UWB radar system for respiratory detection [4]. It has been found that the reflectivity of a body in the frequency band from 0.5-10 GHz decreases with frequency, and that for electromagnetic waves polarised along the human body, the reflectivity is higher than for the waves with orthogonal polarisation. A novel motion/respiratory detector has been used in the radar. The detector is based on measurements of spatial variations in the radar returns. The detector does not require separation of a body reflection signal from the background and works reliably in multi-path indoor environments. Although minor additional results were presented compared to previous research in this field, the presented research is essentially yet again a feasibility study on respiratory detection of a standing person in a room.

- Chernyak from Moscow Aviation Institute, Russia, conducted an elaborate study on signal processing for localisation of trapped victims using UWB radar [15]. He presented required parameter values for data acquisition and provided a suggestion of a clutter-rejection, respiratory motion detection (BMD) and angle-of-arrival algorithms. The study can be regarded very valuable as a starting point for further research in this area, as it covers some fundamental issues that need to be taken into account, but its main drawback is the assumption of idealised conditions and lack of experimental verification.

- The group of K.M. Chen from the Michigan State University, USA, has built two systems operating at different frequencies [16]. The first system operated at 450 MHz, and the second at 1150 MHz. Although not classified as UWB radars, this group investigated detection of trapped victims in real life-like rubble and presence of operators in the vicinity of the rubble site. The results of their experiment showed that both respiratory and heart-beat motion of a lying person was detected through 1.8m of rubble constructed out of bricks, cinder blocks and steel rebars. One of the stated shortcomings of the radar systems are the effects of interference created by the environment and operators.

- An interferometric trapped-victim detection operation radar system was built by the group of I. Arai from the University of Electro- Communications, Japan, operating on a 1215 MHz carrier frequency [17]. The continuous wave is switched by a 10 ns pulse with a certain repetition frequency to obtain a pulsed signal that is transmitted to the survivor. Experimental verification conducted in a collapsed building showed that respiratory detection was possible from a rubble-covered person lying in three different positions: face-up, face-down and on the side. However, as mentioned earlier, the interferometric radar is not a suitable radar technology for trapped-victim detection as it does not provide necessary range resolution.

- During the year 2007 a product emerged on the marked named LifeLocator [18], from UltraVision Security Systems Inc., USA. The product is a compact, standalone, UWB trapped-victim-detection radar which communicates wirelessly with a device held by the operator. According to the company, LifeLocator detects fractions of motion, even extremely shallow respiratory, so that even the most injured victim of a building collapse, avalanche, mine disaster, mudslide or any natural or man-made disaster that can trap living beings can now be located. The alleged depth of respiratory detection is 4.5 m (the type of rubble is not specified). Although the company states that product seems successful in detecting trapped human beings in rubble, reports from independent use of the device under challenging real-life scenarios is non-existent. Due to the scarcity of the available information regarding the exact design and the performance of the LifeLocator, its introduction on the market has no effect on the choice of research topics described in this PhD thesis.

- In 2008, a research group of Sachs of TU Ilmenau in Germany presented work on experimental verification of human being detection using a pseudo-random noise UWB radar [19]. The test person was placed in a concrete tunnel under 30 to 120 cm of wet soil, depending on the position of the antennas. In the case of wet soil, the wave penetration is quite reduced, thus the sensing signals are largely attenuated. This results in

an inability of the radar operator to clearly distinguish the respiratory motion pattern by visual inspection of the data. After post-processing in the frequency domain, the response of the respiratory test person was detected. The group of Dr. Sachs did not consider the presence of the non-stationary clutter nor did they include any assessment on the detection performance.

1.4 Research motivation

At the time of the start of the research presented in this thesis, there were a multitude of unsolved issues and unanswered questions. This section presents the motivation behind the research topics that have been chosen for further investigation and which are based on those unsolved issues.

- A method for dealing with low SNR conditions and presence of non-stationary clutter has not been previously reported, as all the relevant research dealt with idealistic conditions and feasibility studies of detection of concealed humans. Although Chernyak has presented the theoretical performance of a respiratory-motion detection method for realistic SNR conditions, there had been no previously published scientific papers on the performance of an RMD algorithm applied on experimentally acquired data using UWB radar. The presence of non-stationary clutter has been completely ignored in previous research.

- A consideration of external narrowband interference has been completely avoided in the previous research.

- In order to reduce the interference into vital radio communication systems such as Tetra, but also to limit the amount of system noise, there is a need to determine the necessary bandwidth and the appropriate centre frequency for detection of one or several closely trapped victims, in particular in the case of real-life-like rubble. This question has not been answered in previous research in this field. Since the rubble by definition is built up by debris of random orientation, material, size and shape, one should investigate the attenuation of a small number of realistic examples of physical rubble. Such rubble should be constructed using reinforced, randomly oriented concrete slabs, which is considered the most challenging rubble type to deal with and one that is most interesting to be evaluated.

- There have not been any reports in previous literature on the nature of the two only possible target features for UWB-radar-based trapped-victim detection: respiratory- and cardiac motion responses. It is therefore of large interest to investigate their respective feasibility as a target feature under both easy and challenging conditions. What is further of interest is

to characterise their magnitude as function of the following parameters: orientation and position of the body with respect to the antennas and the antenna-pair polarisation.

- The results of using different UWB radar technologies for the purpose of UWB-radar-based trapped-victim detection operations are expected to be different. The question that is yet unanswered is: "What is the UWB radar technology that yields highest SNR values based on an experimental study using identical settings?". The fact that one available UWB radar device differs from another in terms of its state-of-the-art status, makes a definitive conclusion almost impossible; the answer to the question should therefore be merely an indication. The results of the study should serve as a basis for further investigations using other available UWB radar devices and thus striving for a more definitive conclusion.

1.5 Research objectives and delimitation

Having a better understanding on the necessary research tasks in order to answer the above-mentioned questions, this section details what the research presented herein aims for. This section will also state a major issue which is not covered in this research and the are given reasons why. The objectives of the research presented in this thesis can be divided into five main tasks:

1. Assess the preferred UWB radar technology for trapped-victim detection operations by analysing the results of an experimental study involving available UWB radar equipment. The study should be performed under identical conditions, as far as that is achievable.

2. Improve the knowledge and gain deeper understanding of the radar-induced human motion responses, as main target feature of the human body, in order to increase the chances of detection. This includes the investigation of the magnitude of the observed respiratory motion responses as function of body position and orientation, bi-static angle and antenna-pair polarisation.

3. Develop an efficient and novel method for detection of trapped victim(s) in quasi real-life conditions, such as presence of non-stationary clutter and low SNR conditions.

4. Assess the optimal operational frequency band for use on the commonly available types of concrete rubble.

5. Improve the probability of detection of trapped victim(s) by reducing the effect of the external narrowband interference.

1.5.1 End-user requirements

The research presented in this PhD thesis is not driven by strict end-user requirements. However, during talks with the USAR team from the Swedish Rescue Services Agency, which can be considered as an end-user of any type of device for detection and localisation of trapped victims, the members of the team expressed several desired features and functions of a victim-search radar, based on the needs with their work and experience. The USAR team stated that the desirable features of a search-and-rescue radar are:

- Immunity of the system to moving objects in the vicinity of the rubble site, as such activity cannot be fully avoided in real-life situations.
- A rugged and reliable (in terms of detection rate) system that would be easy to operate. However, weight and size are not major issues, since they are prepared to sacrifice that for increased performance.
- Ability to image reasonably well the rubble which would assist in planning for the excavation route inside the rubble.

Their first wish relates to the objective of mitigating the negative influence of the non-stationary clutter. This problem is seen as a grave one and the solution towards its mitigation receives significant attention in the thesis. The second desired feature can only partly be fulfilled. Reliability relates to the level of detection- and false-alarm rate. The development of a dedicated respiratory motion detection algorithm reflects this desire. The algorithm makes the decision on target classification easier for the radar operator. However, the research in this thesis does not aim for a final product or a prototype and therefore cannot take the desire for constructing the radar. The third desired feature is clearly out of scope of this research, since it deals with imaging, which is not covered by the research conducted in this thesis.

1.5.2 Delimitation

As mentioned earlier, the research presented herein focuses on signal processing aspects of detection of trapped victims and does not aim for a product or a prototype.

An important research topic that this thesis will not investigate concerns angle-of-arrival estimation of the responses from the trapped victim(s). The reasons are twofold: a) such research could take considerable amount of time for doing this and, most importantly, b) there have been some firm indications based on a measurement campaign performed on real-life-like concrete rubble using state-of-the-art equipment and respiratory motion detection algorithm, that the maximum achievable detection range is not more than two meters. Due to these reasons, the angle-of-arrival-estimation functionality is not a priority in this research.

Implementation of multi-static radar configuration is regarded as more favourable than bi-static configuration, but also more cumbersome to implement. The research opportunities that emerged for the bi-static approach were deemed a large enough challenge.

1.6 Novelty of approach

The novelty of the chosen approach in the research presented in this PhD thesis is the following:

- Comparison of several available UWB radar technologies and their respective suitability for UWB-radar-based trapped-victim detection.
- Analysis of the radar-induced motion responses in both time- and frequency domain.
- Characterisation of respiratory motion responses as function of body orientation and position, bi-static angle and antenna-pair polarisation.
- Investigation of detectability of trapped victims as function of employed bandwidth and centre frequency.
- Analysis of the presence of non-stationary clutter.
- Analysis of the presence of narrowband interference.
- Investigation on the typical rubble attenuation as function of frequency.
- Test of detection algorithm in real-life-like rubble and under realistic conditions.

Realistic assumptions are made such as:

- The trapped victim(s) are alive, but are not able to give away their location to the USAR crew due to their weak condition or unconscious state.
- The number, orientation and size of the trapped victim(s) are not a priori known.
- Respiratory rate of the victim(s) is not known a priori; only a qualified guess can be made on the frequency range in which it is located.
- Backscattered response from the victim is unknown a priori.

1.7 Main achieved results

The main achieved results are summarised below:

- Development and experimental verification of an efficient algorithm that is able to detect motion responses from trapped victims in low SNR conditions overlapped with stationary and non-stationary clutter. The algorithm performs better than an existing motion detection algorithm, in particular for suppression of non-stationary clutter.

- Performance comparison of three stationary-clutter subtraction methods on an experimentally acquired data set.

- Development and assessment of the performance of four approaches to narrowband interference suppression in UWB impulse radar.

- Experimental acquisition of an extensive and unique database of respiratory motion responses from a single human being, as function of body orientation, bi-static angle, body position and antenna-pair polarisation.

- Analysis of the obtained data in the database and assessment of the detectability of the human respiratory motion responses.

- Analysis of experimentally acquired respiratory- and cardiac-motion responses in time- and frequency domain. Assessment of the feasibility of use of each target feature under challenging real-life conditions.

- Provision of an indication of appropriate bandwidth and centre frequency for detection of trapped victims for various types of rubble.

It is important to emphasise that part of the achieved results have been acquired by assistance of a small number of MSc students, at the time conducting their studies at the IRCTR. Sorina Baldea, a visiting student from the Bucharest Military Academy in Romania, acted as the test person during the measurement campaign aiming for the assessment on the detectability of human respiratory motion responses. She has, to a small extent, contributed toward the initial classification and processing of the acquired data. Solomon Tesfay Abraha and Shenario Ezhil Valavan Amaldoss assisted with additional processing of the data acquired during the same measurement campaign. Their engagement resulted in a joint conference publication [20]. The results detailed in chapter 6 were obtained in co-operation with Imre Damen. The majority of the main ideas and approaches came from the author himself, whereas Imre's contribution was mostly confined to computer simulation of the chosen approaches and obtaining the performance of each proposed NBI suppression method. His engagement resulted in a joint conference publication [21].

1.8 Research framework

The research presented herein was conducted in the framework of two projects:

1. **EUROPCOM**
   The EUROPCOM project is a European Commission (EC)-funded FP6 project which the main focus on research technologies and methods which allow for efficient management and coordination of rescue operations in disaster zones (e.g. in buildings, which have partly collapsed due to fire or earthquake). However, a small (and for this thesis most relevant) part of the EUROPCOM project dealt with fundamental research in the field of detection by means of UWB radar of human beings trapped under rubble.

2. **Radiotect**
   The Radiotect project is an EC-funded FP6 project whose overall goal is to support four SMEs to become more innovative, to adapt their technology, to develop transnational cooperation and to extend their cooperative relations. The technical/scientific goals of the project are "to develop high resolution radar (with bandwidth of up to 5 GHz) and ultra high-resolution radar (with bandwidth of more than 10 GHz) for three application scenarios to be concentrated upon in the project: sensor network for building monitoring; handheld sensor for local building inspection, body scanning" [22].

1.9 Thesis outline

The thesis is organised as follows:

Chapter 2 thoroughly explains the main principle of a trapped-victim detection operation using UWB radar. It further describes four types of UWB radar technologies, their inherent properties and feasibility for use in UWB-radar-based trapped-victim detection operations. In the same chapter, experimental evaluation of the performance of three available types of UWB radars is performed under identical NLOS conditions.

Chapter 3 analyses the respiratory- and cardiac-motion responses in time- and frequency domain and performs a feasibility study on their respective use during UWB-radar-based trapped-victim detection operations. It further details the data acquisition, data processing and results of the measurement campaign for estimation of detectability as function of bi-static angle, body position and orientation and antenna-pair polarisation.

Chapter 4 details an approach and results of a measurement campaign with the

goal to provide approximate indication on the appropriate operational frequency band. Aside from the limitation in the hardware, the choice of frequency band depends on the reflective properties of the human body as well as the rubble material.

Chapter 5 presents the developed respiratory motion detection algorithm, the motivation for its development and its performance relative to an existing algorithm. The respiratory motion detection algorithm is applied on experimentally acquired data under real-life-like conditions and its performance is assessed. The chapter further investigates the performance of three common stationary-clutter suppression methods on a single experimentally acquired data set.

Chapter 6 focuses on development and performance comparison of four narrowband interference rejection methods. The methods are specifically tailored for use in impulse radar systems using stroboscopic sampling.

Chapter 7 provides conclusions and recommends future research tasks.

References

[1] United States Geological Survey. FAQ – Common Myths about Earthquakes. [Online]. Available: http://earthquake.usgs.gov/learning/faq.php?categoryID=6&faqID=110

[2] UK Fire Services Search & Rescue Team. Earthquake Rescue - Learning from Disaster. [Online]. Available: http://www.ukfssart.org.uk/earthquake%20rescue.htm

[3] C. Bäckström and N. Christoffersson, "Urban Search and Rescue - an evaluation of technical search equipment and methods," Master's thesis, Department of Fire Safety Engineering, Lund University, 2006. [Online]. Available: http://www.raddningsverket.se/upload/Om%20verket/examensarbete/usar_report.pdf

[4] A. Yarovoy, J. Matuzas, B. Levitas, and L. Ligthart, "UWB radar for human being detection," *IEEE Aerosp. Electron. Syst. Mag*, vol. 21, Mar. 2006, pp. 10–14.

[5] M. Bimpas, K. Nikellis, N. Paraskevopoulos, D. Economou, and N. Uzunoglu, "Development and testing of a detector system for trapped humans in building ruins," in *Proc. IEEE Microwave Conference*, vol. 3, Oct. 2003, pp. 999–1002.

[6] FCC, "Revision of part 15 of the commission's rules regarding ultra-wideband transmission systems," *First report and order, ET Docket 98-153, FCC 02-48*, Feb. 2002, pp. 1–118.

[7] W. Shrader and V. Gregers-Hansen, *MTI Radar*, ser. Radar Handbook. McGraw Hill, 2008, vol. 3, ch. 2.1–2.9.

[8] Time Domain Corporation. Safety Solutions. [Online]. Available: http://www.timedomain.com/government.php

[9] E. Staderini. (2001) Everything you always wanted to know about UWB radar: A practical introduction to the Ultra Wideband Technology. http://www.uniroma2.it/fismed/faculty/Stadero/papers/osee.pdf.

[10] I. Immoreev, *Main Features of UWB Radars and Differences from Common Narrowband Radars*, ser. Ultra-wideband Radar Technology. CRC Press, 2001, vol. 2, pp. 1–19.

[11] E. Staderini, "UWB radars in medicine," *IEEE Aerosp. Electron. Syst. Mag*, vol. 17, no. 1, Jan. 2002, pp. 13–18.

[12] W. S. Haddad, "The rubble rescue radar (RRR): A low power hand-held microwave for the detection of trapped human personnel," Lawrence Livermore National Laboratory, Tech. Rep., Apr. 1997. [Online]. Available: http://www.osti.gov/bridge/servlets/purl/571102-d7WBku/webviewable/571102.pdf

[13] G. Ossberger, T. Buchegger, E. Schimback, A. Stelzer, and R. Weigel, "Non-invasive respiratory movement detection and monitoring of hidden humans using ultra wideband pulse radar," in *Proc. of the International Workshop on Ultrawideband Systems and Technologies*, May 2004, pp. 395–399.

[14] I. Immoreev, S. Samkov, and T.-H. Tao, "Short-distance ultra wideband radars," *IEEE Aerosp. Electron. Syst. Mag*, vol. 20, Jun. 2005, pp. 9–14.

[15] V. Chernyak, "Signal processing in multisite UWB radar devices for searching survivors in rubble," in *Proc. EuRad 2006*, Sep. 2006, pp. 190-193.

[16] K.-M. Chen, Y. Huang, J. Zhang, and A. Norman, "Microwave life-detection systems for searching human subjects under earthquake rubble or behind barrier," *IEEE Trans. Bio-Med. Eng.*, no. 1, Jan. 2000, pp. 105–114.

[17] I. Arai, "Survivor search radar system for persons trapped under earthquake rubble," in *Proc. IEEE Microwave Conference*, vol. 2, Dec. 2001, pp. 663-668.

[18] UltraVision Security Systems. (2007-2008) LifeLocator - Sensing life in a heartbeat. http://www.ultravisionsecurity.com/pdf/UVSS_LL3_12_5_08.pdf.

[19] J. Sachs, M. Aftanas, S. Crabbe, M. Drutarovsky, R. Klukas, D. Kocur, T. Nguyen, P. Peyerl, J. Rovnakova, and E. Zaikov, "Detection and tracking of moving or trapped people hidden by obstacles using ultra-wideband pseudo-noise radar," in *Proc. EuRad 2008*, Oct. 2008, pp. 408–411.

[20] A. Nezirovic, S. Tesfay, S. E. Amaldoss, and A. G. Yarovoy, "Experimental study on human breathing cross section using UWB impulse radar," in *Proc. EuRad 2008*, Oct. 2008, pp. 1–4.

[21] A. Nezirovic, I. J. Damen, and A. G. Yarovoy, "Narrowband interference suppression in UWB impulse radar for human being detection," in *Proc. ICUWB 2007*, Sep. 2007, pp. 56–61.

[22] S. Crabbe, "Ultra wideband radar for through wall detection from the RADIOTECT project," in *Fraunhofer Symposium, Future security: 3rd Security Research Conference Karlsruhe*, Sep. 2008, p. 299.

2

Data acquisition hardware

Any study on detection of trapped human beings should involve experimentally acquired data in order to gain understanding of relevant features of the human body or to verify the performance of a detection algorithm. The most widely used tools for acquisition of experimental data in this PhD thesis are two technologies of UWB time-domain radars: impulse radar and pseudo-random noise (PRN) radar. The first radar technology is well-proven and offers scalability in terms of data acquisition parameters. The PRN radar is a newer technology and its operational mode differs significantly from that of the impulse radar. Furthermore, it does not offer much choice in data acquisition parameters and is therefore not suitable for certain technologies of measurement scenarios. A subset of stepped-frequency continuous wave (SFCW) radar, a vector network analyzer (VNA), was used in this chapter in order to investigate its potential and advantages over the time-domain radar when used for UWB-radar-based trapped-victim detection operations. The second frequency-domain radar technology, frequency-modulation continuous wave (FMCW) radar, was not used in the comparison due to its unavailability. The first four sections of this chapter provide a short description on the operational mode and the data acquisition of the respective UWB radar technology. The fifth section details the comparison of the relevant inherent features of each UWB radar technology as well the used UWB radar devices. It further presents the approach and the results of a small-scale experimental verification involving a single test person with the aim to compare the available UWB radar devices in terms of achieved signal-to-noise ratio (SNR) performed under identical conditions.

2.1 Time-domain impulse radar

The operational mode of an ultra-wideband, time-domain impulse radar system consists of transmission of a sequence of ultra-short pulses with fixed time

interval T, also called pulse repetition interval (PRI):

$$s(t) = \sum_{n=0}^{N-1} u(t - nT) \tag{2.1}$$

where $s(t)$ denotes a sequence of N pulses $u(t)$. The most common pulse widths and magnitudes are in the order of tens of picoseconds and tens of volts, respectively [1]. The generated pulses propagate through a radio frequency (RF) cable with negligible dispersive properties. The pulses are then radiated by an UWB antenna, reflected from scatterers in the rubble including trapped victim(s) (if present) and recorded by a receive antenna. The most commonly generated pulse shapes are monopulse (Gaussian-like pulse), monocycle (first-order derivative of the monopulse) and ramp pulse [1]. The received range profile $r(t)$ is expressed as:

$$\begin{aligned} r(t) &= \sum_{n=0}^{N-1} \sum_{m=1}^{M} h_m(t) * u\left(t - nT - \tau_m\right) + i(t) + \theta(t) + w(t) \qquad (2.2) \\ &= \sum_{n=0}^{N-1} h_v(t) * u\left(t - nT - \tau_v\right) + \sum_{n=0}^{N-1} \sum_{m=1, m\neq v}^{M-1} h_m(t) * u\left(t - nT - \tau_m\right) \\ &+ i(t) + \theta(t) + w(t) \end{aligned}$$

where $h_m(t) = g_{tx}(t) * a_m(t) * g_{rx}(t)$ is the a-priori unknown combined impulse response, where $a_m(t)$, $g_{tx}(t)$ and $g_{rx}(t)$ denote the impulse responses of the m-th reflection, transmit and receive antenna, respectively; τ_m denotes the time-of-arrival of the m-th reflection; v is the index of the reflection from the victim; M is the number of reflections; '$*$' represents convolution operation; $w(t)$, $\theta(t)$ and $i(t)$ respectively denote the additive white Gaussian noise (AWGN), non-stationary, unwanted amplitude fluctuations and external narrowband interference (NBI), if present. The adverse effects of $\theta(t)$ and $i(t)$ are mitigated in chapters 5 and 6 of this thesis, respectively. The AWGN is comprised of quantisation noise, thermal noise and external atmospheric noise, with the quantisation noise being the dominant noise component.

2.1.1 Data acquisition

Ultra-wide bandwidth in time-domain impulse radar system is achieved by means of generating a pulse train of ultra-short, carrierless electromagnetic pulses. Due to the ultra-short pulse duration of the pulses, a sampling frequency 2.5-3 times higher than the Nyqvist rate is required for proper sampling of the backscattered waveforms [1]. Employing real-time samplers does not represent a feasible solution, mainly due to issues such as limited dynamic range, high cost, large size and weight. Furthermore, the most typical use of real-time

samplers is for sampling non-repetitively generated baseband signals, which is not the case here. A typical sampling method in impulse radar technology is stroboscopic sampling (or equivalent-time sampling), where N pulses are transmitted in order to obtain N sampled points per range profile, during which transmit and receive units are synchronized in order to obtain coherent sampling. For each transmitted pulse, the sampling interval (which is identical with T) is offset with the effective sampling time t_s, see fig. 2.1. The principle of a stroboscopic sampler is, therefore, a down-conversion of the radio frequency signal in the nanosecond time region to an equivalent version in the micro- or millisecond time region [1].

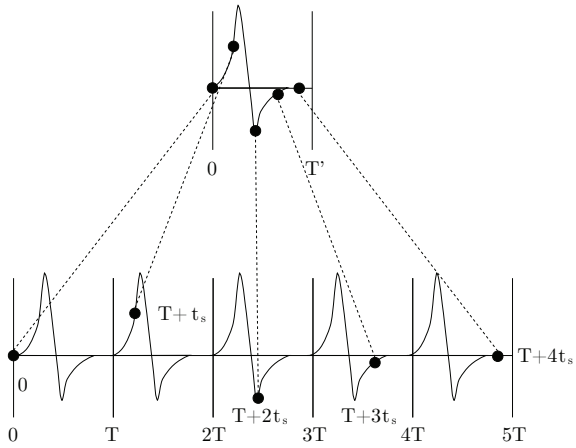

Figure 2.1: *The principal idea behind stroboscopic sampling; example shows samples over the pulse duration.*

Assuming no presence of the non-stationary scatterers and NBI, the sampled range profile $\mathbf{r}[n] = [r[1], r[2], \ldots, r[N]]^T$, where $[\cdot]^T$ denotes the transpose operation, $n \in \mathcal{N}$ and $\mathcal{N} = \{1 \ldots N\}$ is the sampling index, is expressed as:

$$\mathbf{r}[n] = \mathbf{h}[n] + \mathbf{c}[n] + \mathbf{w}[n] \qquad (2.3)$$

where

$$\mathbf{h}[n] = \begin{cases} 0 & \text{if } 1 \leq n \leq n^* - 1 \\ \mathbf{h}^*[n] & \text{if } n^* \leq n \leq n^* + N^* - 1 \\ 0 & \text{if } n^* + N^* \leq n \leq N \end{cases}$$

$\mathbf{h}^*[n] = [h^*[1], h^*[2], \ldots, h^*[N^*]]^T$ is the N^*-sized array representing the human target response (the backscattered response from the trapped victim), where $N^* \ll N$; n^* is the a-priori unknown position in the range profile of $\mathbf{h}^*[n]$; $\mathbf{c}[n] = [c[1], c[2], \ldots, c[N]]^T$ represents all the stationary reflections, i.e. those that are time-invariant, known as stationary clutter.

2.1.2 Averaging

The acquisition time of a single range profile $T_{a,1} = N \cdot T$ is several orders of magnitude shorter than the human respiratory motion (breathing) period T_h. This therefore provides an opportunity to coherently average a large number of range profiles in time domain:

$$\bar{\mathbf{r}}_k[n] = \frac{1}{L} \sum_{l=1}^{L} \mathbf{r}_l[n] \qquad \boxed{2.4}$$

thus obtaining $10 \cdot \log_{10}(L)$ dB reduction in AWGN power [1]. The integer $l \in \{1, \ldots, L\}$, L denotes the averaging value and $[\ \bar{\cdot}\ ]$ denotes the averaging operation. It can be shown that for $T_a < T_h/6$ the energy loss due to coherent averaging does not exceed 0.5 dB [2]. A single averaged range profile is acquired within the acquisition time $T_a = T_{a,1} \cdot L = TNL$ seconds, which is usually in the range of tenths of a second. This is regarded as an appropriate acquisition time in order to adequately describe the human respiratory motion. The integer $k \in \{1, \ldots, K\}$ is the index of the acquisition time, where K denotes the number of acquired averaged range profiles. This dimension is typically called the slow-time dimension and is orthogonal to the fast-time (or range) dimension. The averaged range profiles are stored in a $K \times N$ data matrix $\mathbf{R} = \mathbf{R}[k, n]$, see fig. 2.2.

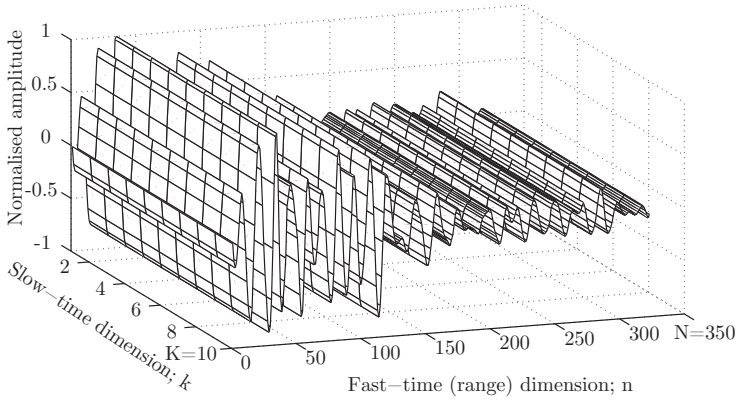

Figure 2.2: *A 3-dimensional representation of 10 averaged range profiles with normalised amplitude.*

2.1.3 Unambiguous range

The backscattered response from the victim arrives at the radar receiver at the time $\Delta t = 2r^*/c_m$, where r denotes the range and $r = r^*$ is the distance to

the victim; c_m is the propagation speed of the pulse in the propagation medium (most commonly debris with pockets of air, i.e. rubble). The range of the victim r^* should be within the unambiguous range of the radar r_{max}, which is the maximum range of a scatterer that can be unambiguously determined. It is defined as $r_{max} = c_0/(2T)$, where $c_0 = 3 \cdot 10^8$ m/s is the speed of light. Any strong, non-stationary scatterer located at the range $r' = r_{max} + r^*$, will overlap in range with the response from the victim. This can be seen as sort of aliasing in range. Although it is favourable to employ larger values of T in order to obtain larger r_{max}, the largest allowed averaging value thereby becomes smaller, hence giving rise to higher AWGN power.

2.2 Pseudo-random noise radar

The operational mode of a PRN radar consists of a clock with frequency f_c periodically pushing a high-speed digital shift register, which generates N sequences $u(t)$ (so called m-sequence). The m-sequence exhibits a very short triangular auto-correlation function [3]. Each $u(t)$ consists of $2^{n_p} - 1$ pseudo-random rectangular waveforms, or chips, where n_p is an integer value (typically 9). In contrast to the classical impulse excitation, the m-sequence distributes its energy over the complete length of $u(t)$ (i.e. having a unitary duty cycle), thus avoiding signals with a high peak value which are normally difficult to handle [4]. Each m-sequence $u(t)$ is passed through an anti-aliasing filter having $f_c/2$ cut-off frequency before being radiated by the transmit antenna into the rubble. Under the assumption of the presence of a victim, the radiated waveform is reflected from the trapped victim and the surrounding objects and is recorded by the receive antenna.

Due to the ultra-wideband characteristic of the noise-like waveforms in $r(t)$, stroboscopic sampling is used in order to lessen the requirements on the analogue-to-digital converter (ADC). The received wideband signal directly pushes the ADC and the track-and-hold (T&H) circuit, where the T&H captures the wideband signal and provides it to the ADC which can work at the suitably low sampling frequency $f_s = f_c/2^{n_p}$ [4]. Impulse compression is then performed either by implementing Fast Hadamard Transform (FHT) (i.e. a cross-correlation referring to the ideal m-sequence) or by Fast Fourier Transform [3]. This is performed before sampling in order to avoid impulse-like waveforms, thereby obtaining higher effective dynamic range. The block scheme in fig. 2.3 shows the principal operational mode of a PRN radar.

2.3 Stepped-Frequency Continuous Wave radar

Radars that acquire data in the frequency domain and transmit continuously (transmitter always on) are known as continuous wave (CW). Stepped-frequency

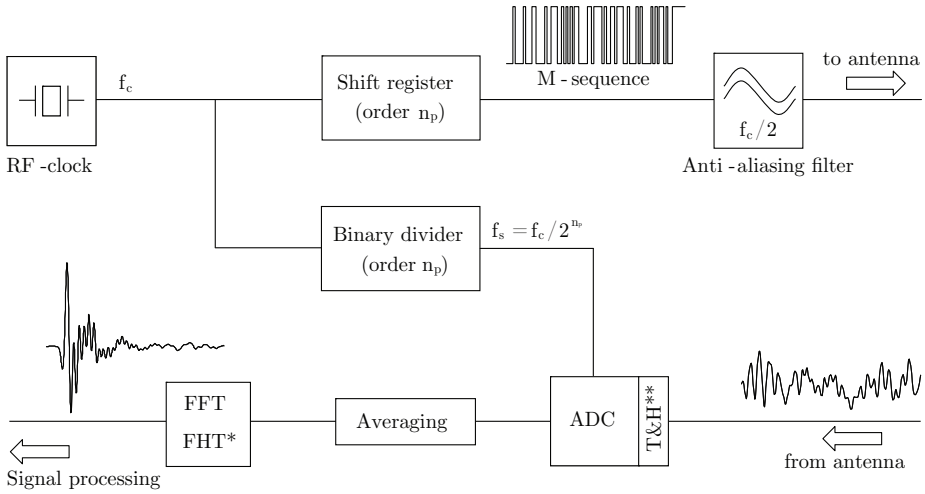

* FHT - Fast Hadamard Transform

** T&H - Track-and-Hold circuit

Figure 2.3: *Typical functional blocks of a PRN radar [3]*

continuous wave (SFCW) is a frequency-domain radar technology that incorporates successive transmission of N sinusoids separated in frequency by Δf Hz. At each frequency the backscattered signals are received and fed to a mixer via a low noise amplifier (LNA), where they are mixed with the coupled part of the transmitted sinusoid to an intermediate frequency (IF). An IF filter is implemented in order to filter out-of-band noise. The bandwidth of the IF filter is thus proportional to the overall dynamic range (by varying the noise floor), but inversely proportional to the acquisition time. This is trade-off and it is a subject of optimisation, depending on application. Most implementations use the Inverse Discrete Fourier Transform (IDFT) to transform the data into time domain. This yields a synthesised pulse [1]. Vector network analyzer (VNA) can be seen as a subset of a SFCW radar, although VNA is an instrument which is primarily used for the analysis of the properties of electrical networks and not as a radar device per se. In the absence of a dedicated SFCW radar, however, a high-end VNA is used in the next section for the feasibility study on its use as a radar technology for UWB-radar-based trapped-victim detection operations. Before the use of a VNA, calibration needs to be performed in which high-end test cables are used. This results in the measurement reference plane to be moved to the very ends of the test cables. The importance of correct calibration procedure will become apparent later in the chapter.

2.4 Frequency-Modulated Continuous-Wave radar

The second type of the frequency-domain radar technology is called frequency-modulated continuous-wave (FMCW) radar. Its operational characteristics is based on transmitting a continuous wave, which is linearly modulated in frequency, covering a bandwidth B during the sweep repetition interval T. The process is then repeated, thus creating a sawtooth behaviour in frequency domain, or a series of so called chirp signals in time domain, see fig. 2.4. In the receiver, the time-delayed backscattered responses are deramped, i.e. multiplied with the coupled transmitted signal and subsequently low-pass filtered. The frequency of the resulting signal after deramping is called the beat frequency, which can be expressed as [5]:

$$f_b = \frac{B}{T}\Delta t = \frac{2rB}{c_m T} \tag{2.5}$$

Thus, for given B, T and c_m, the target range $r = r^*$ can be directly obtained through measuring f_b.

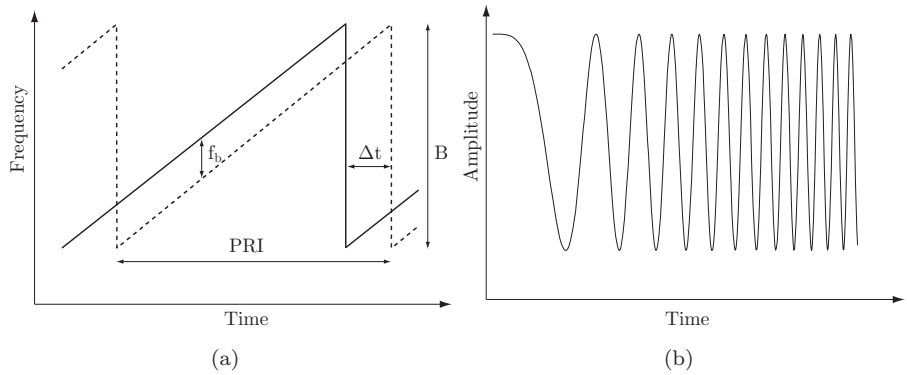

Figure 2.4: *The principle of operation of an FMCW radar in a) frequency domain and b) time domain.*

2.5 Comparison of available UWB radar technologies for trapped-victim detection

Having reviewed the four available UWB radar technologies, it is of interest to investigate which UWB radar technology is favourable for UWB-radar-based trapped-victim detection operations. This comparison is done both by comparing relevant features and characteristics of each UWB radar technology, as well as by means of a direct comparison of experimentally acquired data using state-

of-the-art, commercially available equipment (excluding FMCW radar technology, due to lack of its availability at the time).

2.5.1 Advantages and disadvantages of each UWB radar technology

The previous section detailed the different approaches each UWB radar technology employs for achieving ultra-wide bandwidths. There are therefore inherent characteristics of each technology that might be of advantage or disadvantage that are relevant for the purposes of detection of trapped victims. These are highlighted in table 2.1.

After examining table 2.1 it soon becomes evident that the CW UWB radar technology (FMCW and SFCW) is favourable to the time-domain radar technology due to high dynamic range, stability, full occupancy of the bandwidth, as well as scalability in signal generation. Those parameters are all better, or in the worst case, equal to either of the other two time-domain technologies. The only minor disadvantage with CW UWB radar technology is the need for linearity in ADC and signal generation, which impulse radar in particular is not sensitive to. However, with the advance of highly linear direct digital synthesis (DDS) for signal generation in CW UWB radar technology, such disadvantages are becoming less important. The major drawback with impulse radar is its inefficient use of the available dynamic range and the occupied bandwidth, whereas this is not the case with PRN radar technology. However, due to the possibility of range gating as well as relative immunity to non-linearity of impulse radar, it can avoid the antenna cross-talk component and use the available dynamic range fully on the late-time components. This should result in higher performance in terms of SNR.

Given the high potential of CW UWB radar technology, it is of outmost interest to compare the performance of a radar device using such technology to two readily available time-domain devices, despite the unavailability of a dedicated SFCW or FMCW radar device.

2.5.2 Previous studies

A theoretical study has been conducted by Yarovoy et al. [8] on the requirements for detection of human beings behind a 40 cm concrete wall and up to 20 m away. The study concluded that, for certain requirements on the radar system performance, a dynamic range of 140 dB is needed to enable detection [8]. All aforementioned radar technologies were investigated in terms of the feasibility of their use. The study came to the conclusion that the CW UWB radar technology can potentially offer such dynamic range.

Table 2.1: *List of advantages and disadvantages of impulse-, PRN- and CW UWB radar technology [1, 3, 6, 7].*

UWB radar technology	**Advantage**	**Disadvantage**
Impulse radar	- Readily available and widely used technology. - Offers scalability of the measurement parameters. - Relaxed requirements on the linearity range of the receiver electronics. - Allows for range gating.	- Typically requires stroboscopic sampling. - No scalability in signal generating parameters. - Low average transmit power. - Limited precision of ADC - Inefficient use of bandwidth and dynamic range. - Low duty cycle.
Pseudo-random noise radar	- Relatively immune to narrowband interference. - High timebase stability if not close to saturation. - No impulse-like waveforms; makes better use of the available dynamic range. - Typically makes better use of the occupied bandwidth than the impulse radar. - Full duty cycle. - Relatively cheap technology.	- Typically requires stroboscopic sampling. - No scalability in signal generating parameters. - Limited scalability in signal measurement parameters. - Sensitive to non-linearities in the receiver electronics. - Reduction in down-range resolution due to high sidelobes. - Limited precision of the ADC. - No possibility of range gating.
CW UWB radar	- Complete use of the occupied bandwidth. - Very high dynamic range and ADC precision. - Stable. - Offers high transmit power. - Full duty cycle. - Scalability of signal generating parameters.	- Confined to the linear range of the ADC. - Need for highly linear signal generation. - Inability to make the full use of the available power due to potential restrictions. - Presence of intermodulation products reduces dynamic range. - No possibility of range gating.

Although the requirements in the referenced study are more stringent than they need to be in the case presented herein, it confirms that the CW UWB radar technology is, from theoretical point of view at least, the most promising technology for the purpose of UWB-radar-based victim detection.

2.5.3 Features comparison of available UWB radar devices

For the features comparison of the selected UWB radar devices, five different parameters which are of large importance for the overall performance are taken into account: dynamic range, resolution of the ADC, average transmit power, duty cycle (fraction of time that a system is in the "active" state) and spectral occupancy (capability of the radar device to occupy the designated spectrum). Table 2.2 shows reported parameter values of the following UWB radar devices:

- time-domain impulse radar (Geozondas SD-303NF sampling converter + GZ1117AN pulse generator + LNA),
- pseudo-random noise radar (Meodat m-sequence) and
- vector network analyzer (VNA; Agilent E8364B).

The Agilent E8364B is a weather sensitive, bulky, heavy and a very expensive device and is therefore not very well suited for outdoor use. Furthermore, it is not built specifically for use as an UWB radar device. That notwithstanding, the values of the parameters suggest that the VNA has a large advantage over the two time-domain radar technologies since its values are equal or better and should therefore result in higher SNR values. The Meodat m-sequence PRN radar shows somewhat similar values as the Geozondas impulse radar, so a definitive conclusion cannot be drawn on the preference of either time-domain radar device solely based on the shown parameters.

2.5.4 Measurement scenario and set-up

For the experimental comparison stage, data was acquired under identical conditions, using the same set-up, antennas and position of the test person. The aim was to use the same measurement parameters (see tab. 2.2) as far as possible for all three radar technologies, in order to obtain as fair comparison as possible. In the case of the PRN radar, there exists no freedom of choice regarding the time window and the number of sampling points. This made it impossible to have exactly the same measurement parameters since the time window of the impulse radar cannot be set to 113 ns. Instead, a maximum time window of 80 ns was selected.

The equipment that was used during the experimental verification stage described in the next section is listed in the Appendix A. The data acquisition was

Table 2.2: *The parameters of the used radar technologies and their respective measurement parameters*

Parameter name	**Impulse radar**	**PRN radar**	**VNA**
Dynamic range	65 dB	78 dB	117 dB (10 Hz IF bandwidth)
ADC resolution in bit	12	12	N/A
Av. transmit power	10 dBm	6 dBm	10 dBm
Spectral occupancy	67% (freq.: DC - $B_{\text{-10dB}}$)		100%
Duty cycle	2%	100%	
Measurement parameters			
Time window T	80 ns	113 ns	
Nr. of points N	511		
Equivalent f_s	6.38 GHz	4.51 GHz	
Acquisition time T_a	0.23 s		
Nr. of acquisitions K	400		
IF bandwidth	N/A		3 kHz
Op. freq. band	395 – 1600 MHz (bandpass-filtered)		300 – 2560 MHz (yields $T = 113$ ns)

performed in a controlled environment (a cellar surrounded by 1.2 m reinforced concrete walls). The test person was resting in a horizontal position 80 cm behind and facing a 60 cm thick, reinforced concrete wall which acts as the obstacle, and directly in front of another 60 cm thick concrete wall. The attenuation of the wall as function of frequency can be seen in fig. 4.2(b). The height of the chest was roughly at same height (1 m) as the antennas located on the other side of the wall, which are put in direct contact with the wall and pointing toward the test person. Absorbing material was inserted between the antennas in order to reduce the cross-talk. For the measurements using impulse radar, an LNA (see A.5) was used in order to have the largest possible signal at the input of the ADC, while still being within the stable region of the receiver electronis. The PRN radar was equivalently pushed to its limits in terms of transmission power and linearity level (the saturation level was 77%).

The acquired data for each radar technology was processed in the same way: stationary clutter removal was followed by a FFT and windowing in the slow-time dimension (see section 5.6 for further details on these processing steps). The criterion that is used for comparing the technologies in the experimental verification phase is the resulting SNR value (see eq. 5.19 for the definition of SNR).

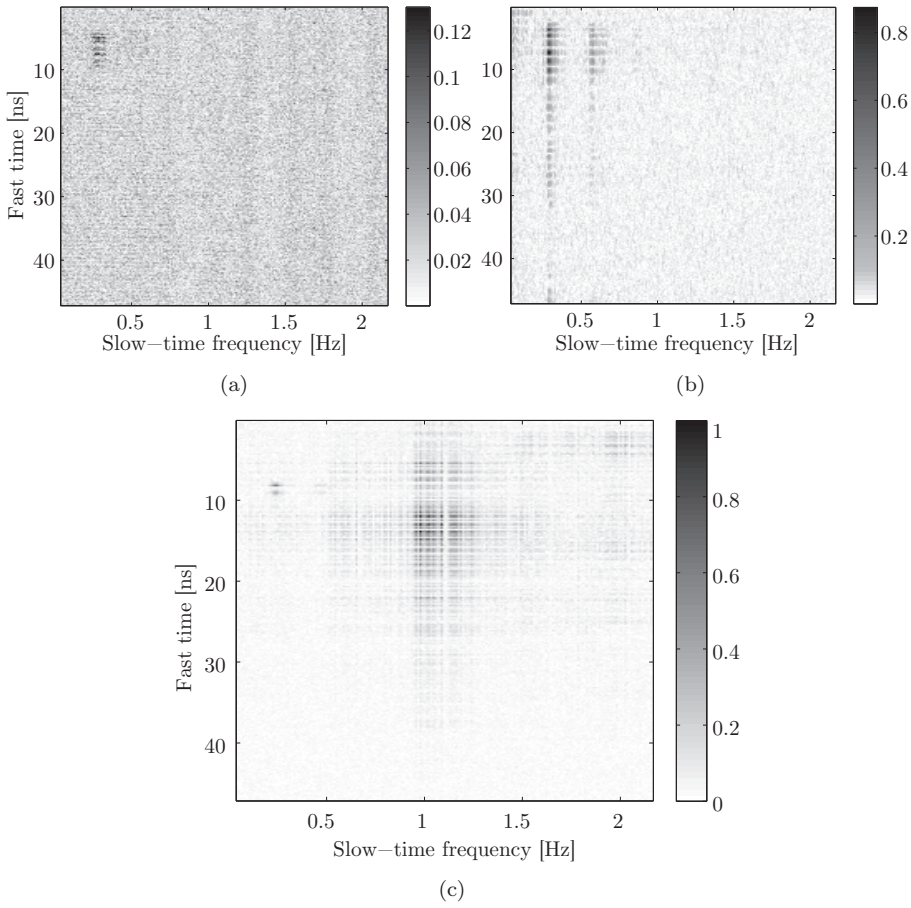

Figure 2.5: *Result of data processing for a) Meodat m-sequence radar, b) Geozondas SD-303NF + GZ1117AN + LNA and c) Agilent E8364B VNA. The noise variance is equalised for all three datasets. Amplitudes are normalised to the highest value of all datasets (peak value of the cardiac motion (heartbeat) response shown in c)).*

2.5.5 Results of the experimental verification

The result of the data processing can be seen in fig. 2.5. The resulting noise variance is equalised and the values normalised to the highest occurring value for all datasets. This is done in order to facilitate the comparison of the results. In all three subfigures the respiratory motion response is located at ca. 0.25 Hz, which is considered a normal rate of respiration. From fig. 2.5(a) it is obvious that the SNR for the PRN radar is the lowest of all three. This can be also seen from fig. 2.6, which shows the spectrum in the slow-time dimen-

sion that contains the strongest occurring respiratory motion response for the respective radar technology. What is obvious from both figures is that the impulse radar produces the respiratory motion response experiencing the highest SNR value, contrary to the judgment based on the theoretical features of the respective technology. The achieved SNR for the impulse radar is 14.4 dB, followed by 7.0 dB for the vector network analyzer and 5.1 dB for the PRN radar.

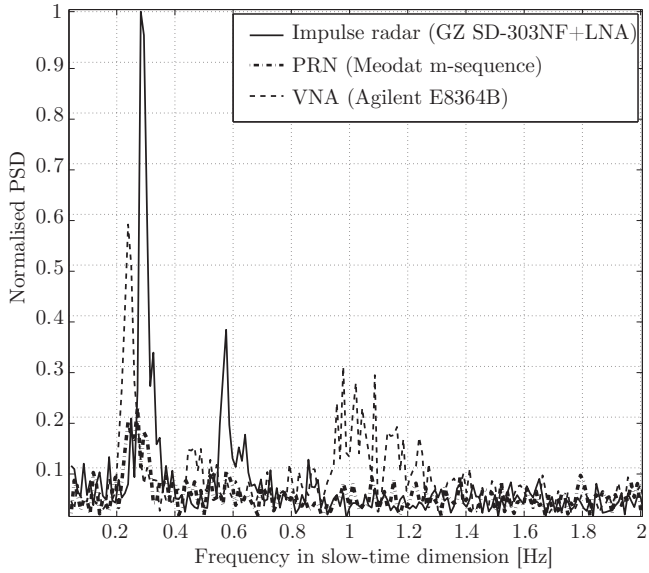

Figure 2.6: *Spectra in slow-time dimension of the strongest occurring respiratory motion response for each radar technology. The spectra were scaled for equal noise variance.*

A surprising result emerged after processing the data acquired using the VNA. The dispersed response located at ca. 1.1 Hz is the response of the cardiac motion. The achieved SNR of the cardiac motion response is 19.4 dB, which is significantly higher than the achieved SNR belonging to the respiratory motion response (7.0 dB). This unexpected result can with high probability be attributed to the fact that the calibration of the VNA did not include the addition of RF cables and antennas, thus creating an impedance mismatch. The mismatch results in a standing wave with the frequency of ca. 300 MHz, as can be seen from fig. 2.7, which shows normalised, average power spectral density of the range profiles for the respective radar technology. It is clear that the PSD of the VNA experiences notches that are equally spaced across the frequency spectrum, whereas this behaviour is not so profound for the other two radar technologies. The notches are particularly profound for frequencies

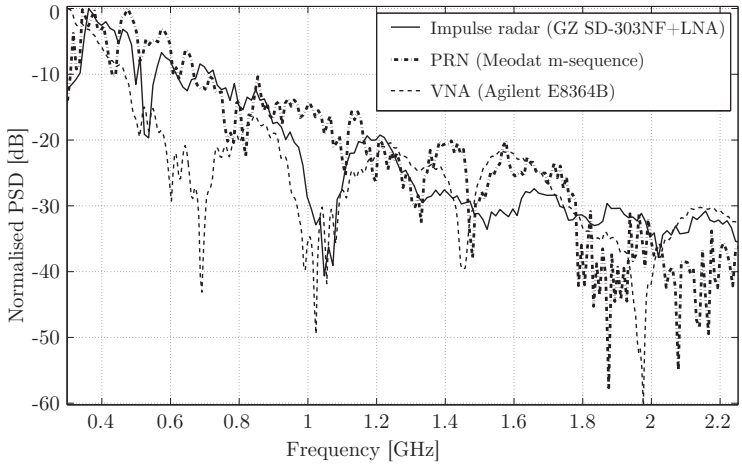

Figure 2.7: *Averaged, normalised power spectral density in the fast-time dimension of the three radars. Equally spaced notches due to impedance matching are clearly visible across the whole frequency range for the VNA-acquired data.*

below ca. 1.2 GHz which leads to a significant loss of transmitted energy in that frequency range. This is also the reason that the SNR of respiratory motion response using impulse radar is higher than the respective response when using VNA. However, it seems that the cardiac motion responses are not affected as much as the respiratory motion responses are, which indicates that the energy loss is most profound in the lower frequency range.

Another interesting feature of fig. 2.5 is that the cardiac motion responses are dispersed both in frequency and in range. The reason for the frequency dispersion can be understood if one keeps in mind the relative instability of the cardiac motion over time (compared to the respiratory motion), in particular if the test person had not been resting for a long period of time prior to the data acquisition (which was the case during this particular data acquisition). Naturally, in real-life scenarios it is expected that the cardiac motion responses would be somewhat more focused in the frequency domain since the victim had been motionless for a long period of time. Furthermore, the acquisition time t_a of the used VNA was observed to be unstable, most probably due to inadequacies in the triggering unit. t_a can be characterised as a random variable with the mean value $\mu = 230$ ms and standard deviation $\sigma = 9.7$ ms. This can be yet another contribution to the spreading of the cardiac motion responses in the slow-time frequency dimension.

Fig. 2.8(a) shows normalised PSD of the acquired data using the VNA as function of slow time. It is seen that the respiratory motion responses are located around 500 MHz (particularly visible at slow-time frequency 0.25 Hz

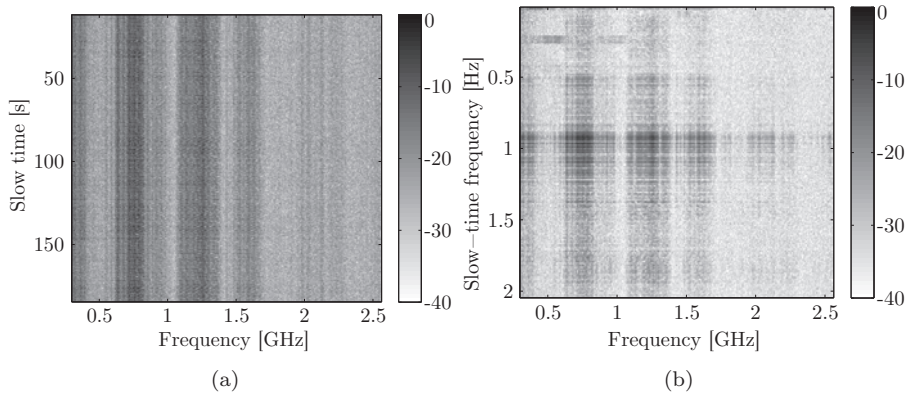

Figure 2.8: *Normalised spectrum of the data acquired using the VNA as function of a) slow-time and b) frequency in slow-time dimension. Decibel scale.*

in fig. 2.8(b)), whereas frequencies in fig. 2.8(a) stretching until ca. 1.7 GHz are attributed to the cardiac motion responses. This becomes even clearer if one observes the subfigure fig. 2.8(b) which shows the same data set, but this time as function of frequency in the slow-time dimension. The dispersion in range, however, is more difficult to explain. One possible explanation is the fact that the cardiac motion results in the whole torso and adjacent body parts to minutely pulsate with the motion of the heart, thereby contributing to the dispersed responses seen in fig. 2.5c). The time-of-arrival difference between the respiratory- and cardiac motion responses of ca. 3 ns corresponds to 50 cm in range, which fits very well with the physical dimensions of the human body. As the test person was resting on the side in direct contact with a concrete wall, it is possible that reverberations of the sensing waveforms had occurred between the body and the wall. This typically results in multiple responses in the acquired data set. Since presumably a large part of the body was pulsating as result of the cardiac motion, and thus covering a larger area for reverberations than in the case of respiratory motion, this probably caused further spreading in range of the cardiac motion responses.

The fact that the SNR of the cardiac motion responses using the VNA was particularly high, indicates that a VNA, due to its extremely large dynamic range, is able to detect even the weakest motion from the human body located behind a thick concrete wall. Provided that the large energy loss in the lower frequency range is avoided by appropriate calibration, it can be concluded that a large dynamic range system has a large potential for use in UWB-radar-based trapped-victim detection operations. As previously mentioned, a VNA is not intended for such usage given the need for proper calibration, its acquisition-time instability and its weather sensitivity. However, it shows that there is a need

for development of a purpose-built high-dynamic-range SFCW radar device for use in UWB-radar-based trapped-victim detection operations.

2.5.6 Important remarks on the obtained results

Having in mind the results obtained in this chapter, there are five important remarks that should be highlighted. Firstly, this study was conducted at a very late stage. By the time the reasons for the peculiar behaviour of the results using VNA were realised, it was too late to attempt to circumvent the issues of impedance mismatch, if at all possible, or to use another SFCW radar device. Secondly, it is very important to state that the results herein do not affect the choice of the radar technology/device in the following chapters. Their choice is simply a matter of practical issues, most importantly the availability of the radar equipment. The third remark is that the analysis in this chapter was based on three categories of commercial radar technologies available to us. Other commercially available radars falling into one of the three categories, in particular the very recent models, might very well produce different results. Fourthly, there are other factors than achievable SNR that influence the final choice of UWB radar technology for this application, such as scalability of measurement parameters (e.g. variable pulse repetition interval), short- and long-term time base stability, weather sensitivity, price etc. Lastly, the study involved a single data set acquired from a single person using a single wall acting as the obstacle. In conclusion, this study is not thorough nor definitive, hence the results presented herein should be merely interpreted as guidelines for future use and further studies on the topic.

2.6 Conclusion

In this chapter we have presented three ultra-wideband radar technologies, each achieving ultra-wide bandwidths in three significantly different ways. The first UWB radar technology is time-domain impulse radar which transmits a pulse train of ultra-short pulses with fixed pulse repetition interval. The second UWB radar technology is pseudo-random noise radar, which achieves ultra-wide bandwidths by transmitting a short burst of pulses with quasi-random polarity and performing correlation at the receiver end after sampling. The third UWB radar technology, stepped-frequency continuous wave, transmits a sinusoid with known amplitude and phase, but with fixed frequency increments in increasing order. Lastly, the fourth reviewed UWB radar technology, frequency-modulated continuous wave, achieves ultra-wide bandwidths by continuously increasing the frequency of a sinusoid. At the receiver end, the backscattered sinusoid is mixed with the transmit signal to produce a beat frequency. The two CW UWB radar technologies exhibit very promising features for UWB-radar-based trapped-victim detection purposes. Due to the lack of availability of a dedicated

FMCW and SFCW radar device, a vector network analyzer was utilised as an alternative to SFCW. Although the VNA is a very stable and precise system with high amount of dynamic range, its use in the field is limited due to its need of proper calibration, but mainly due to its weather sensitivity, high cost, large size and weight. The impulse radar has been the most widely used radar technology so far, both in this thesis and elsewhere, since it is a well-proven technology and was readily available during the course of the research studies. It is furthermore flexible, as it provides many degrees of freedom in terms of measurement parameters. The PRN radar had not been used earlier for this particular application, as it became perfected and available commercially only in the past couple of years. In order to investigate and compare the performance of each radar technology for radar-based trapped-victim detection operations, a measurement campaign was conducted under challenging NLOS conditions using the same measurement set-up and parameters (similar to as high degree as possible), as well as subsequent data processing.

The performed measurement campaign shows that out of the three investigated radar technologies the PRN radar performs the worst in terms of achieved SNR. It is therefore considered the least preferred radar technology for UWB-radar-based trapped-victim detection operations. The impulse radar, used together with an LNA at the receiver end, achieves the highest SNR values: 7.4 dB higher than the VNA and 9.3 dB higher then the PRN radar. However, it is interesting to note that the data acquired by the VNA exhibits SNR belonging to the cardiac motion response amounting to 19.4 dB, whereas there was absence of cardiac motion responses in the data acquired by the two time-domain radar devices. It can be concluded that a VNA is a high-dynamic-range device which is able to resolve even the weakest motion of the human body under challenging conditions. Unfortunately, calibration of the used VNA prior to the data acquisition did not include the RF cables and antenna, thereby leading to a standing wave in the time domain, which translates to notches in the frequency domain. These, in turn, translate to the loss of transmit energy, particularly in the lower frequency range, which ultimately results in the attenuation of the backscattered responses at those frequencies. Circumventing this problem, though, and adapting the VNA for use in UWB-radar-based trapped-victim detection operations, one obtains a highly capable radar system for that application, which outperforms the impulse radar and the pseudo-random noise radar technology in terms of obtained SNR.

It should be noted that the study presented herein is not definitive and all-encompassing and hence the presented results should merely be seen as guidelines for future studies on the topic.

References

[1] D. J. Daniels, *Modulation Techniques*, 2nd ed. The Institution of Electrical Engineers IEE, 2004.

[2] V. Chernyak, "Signal processing in multisite UWB radar devices for searching survivors in rubble," in *Proc. EuRad 2006*, Sep. 2006, pp. 190–193.

[3] J. Sachs, R. Herrmann, M. Kmec, and P. Peyerl, "Modified M-Sequence UWB-Radar," in *Proc. of German Microwave Conference*, Mar. 2006.

[4] J. Sachs, P. Peyerl, R. Zetik, and S. Crabbe, "M-Sequence Ultra-Wideband-Radar: State of Development and Applications," in *Proc. of Radar Conference, 2003*, Sep. 2003, pp. 224–229.

[5] A. Meta, "Signal processing of FMCW synthetic aperture radar data," Ph.D. dissertation, Delft University of Technology, Oct. 2006.

[6] S. Koppenjan, *Ground Penetrating Radar Systems and Design*. Elsevier Science, 2008.

[7] R. Fry and D. Gray, "CLEAN deconvolution for sidelobe suppression in random noise radar," in *Proc. EuRad 2008*, Sep. 2008, pp. 209–212.

[8] A. Yarovoy, X. Zhuge, T. Savelyev, and L. Ligthart, "Comparison of UWB technologies for human being detection with radar," in *Proc. EuRAD 2007*, Oct. 2007, pp. 1574–1577.

3

Experimental characterisation of small-scale movements of the human body using UWB radar

3.1 Introduction

Small-scale movements in unconscious victims, such as the respiratory and cardiac motion are the only externally observable movements produced by an unconscious or an incapacitated human body that indicate that the victim is still alive. Although such movements are of periodic nature, their extraction is nevertheless regarded challenging due to various reasons. One of the main reasons is that such motion is characterised by small magnitude of displacement, as well as relatively small area within which this displacement occurs. Although the respiratory motion constitutes the most feasible target feature for UWB-radar-based detection of trapped victims due to its larger displacement, it is nevertheless necessary to obtain a typical value of the ratio between the energy of the radar-induced respiratory- and cardiac motion responses, respectively. This is evaluated in the first section of this chapter. The displacement of the chest due to respiratory- and cardiac motion, respectively, and their respective SNR values, is experimentally evaluated for three positions of the body and presented in the second section. As the respiratory motion is considered the primary target feature, there is a need for as large understanding as possible of the radar-induced respiratory motion responses. The third section of this chapter therefore analyses a large number of respiratory motion responses from a human body under line-of-sight conditions and for various parameters, such as aspect angle, antenna-pair polarisation, body position and bi-static angle (the angle subtended between the transmit antenna, the human body and the receive antenna). The aim is to obtain a measure on the detectability of the human respiratory motion responses as function of the mentioned parameters. It further analyses the respiratory motion responses in both time- and frequency

domain for various parameters. The obtained results provide better basis for a respiratory-motion detection algorithm, facilitates further research into multi-static radar configuration modes and the choice of the antenna-pair polarisation. The novelty of the approach lies in the fact that the respiratory motion is characterised as function of a multitude of parameters, which cover a significant number of likely real-life situations. To the author's best knowledge, the obtained database is unique in its scope and the investigated parameters.

3.2 Evaluation of target features for UWB-radar-based trapped-victim detection

Since the respiratory- and cardiac motion are the only available target features for use in an UWB-radar-based trapped-victim detection operation, one needs to investigate the feasibility of their extraction during the victim detection stage. The chosen approach is to acquire a dataset containing respiratory motion of a test person under LOS and non-line-of-sight NLOS conditions for various positions of the body. The procedure is then repeated with the aim of acquiring cardiac motion responses only under identical conditions. A respiratory-to-cardiac-motion-response energy ratio E_{rc} for respective body positions and conditions, is obtained, thereby providing insight in the feasibility of using each target feature for detection. Although such analysis does not provide a statistical distribution of the energy ratio, it is nevertheless regarded as a representative one of a typical human body. It is therefore suitable for assessment on the feasibility of each target feature for detection of trapped victims.

3.2.1 Data acquisition and equipment

The data acquisition was performed in a large and spacious cellar surrounded by 1.2 m reinforced concrete walls located in the Electrical Engineering building of the Delft University of Technology. The subterranean location of the cellar along with its thick walls provides good isolation from external narrowband interference, which is necessary in order to obtain high quality data. The data acquisition was performed under LOS and NLOS conditions, with a 60 cm reinforced concrete wall acting as an obstacle, in the latter case. The attenuation as function of frequency of the wall roughly models attenuation of a typical pile of rubble and is shown in 4.2(b). The equipment that was used comprised of the SD-303NF sampling converter (see A.1.1), GZ-1117AN pulse generator (see A.1.3), SU-3126M sampling head (see A.1.1), two identical dielectric wedge antennas (see A.4.2), an analogue band-pass filter with passband 395-1600 MHz (see A.5) in order to suppress low-frequency narrowband interference and an LNA (see A.5). The measurement parameters are shown in table 3.1. The antenna cross-talk needed to be accommodated within the linear range of the

ADC in order to avoid non-linear responses, thereby effectively limiting the transmit power. In the case of NLOS, however, an additional 8 dB power was transmitted since the magnitude of the antenna cross-talk was reduced due to the direct contact of the antennas with the wall.

Table 3.1: *Measurement parameters*

Parameter name	**Value**
Effective sampling frequency f_s	100 GHz
Number of samples per range profile K	1024
Acquisition frequency f_a	8 Hz
Observation time T_{obs}	91 s (respiratory); 67 s (cardiac; average)
Digital filter cut-off frequency	3700 MHz

3.2.2 Measurement scenarios

A normal-sized, male test person, breathing in a relaxed manner, was resting on a polystyrene foam in as close contact as possible with a concrete wall, both under LOS and NLOS conditions. The antennas were placed in the horizontal-horizontal position (HH) facing the test person and placed 2.5 m from it in both cases. For each case, three body positions were investigated: lying on the side and facing the antennas (for future reference named "front" position), lying on the stomach ("stomach" position) and lastly lying on the side with the back turned to the antennas ("back" position). These positions were chosen in order to model the position of the body relative to the antennas while lying under rubble. For each position of the body, a single data set of respiratory and cardiac motion was acquired. In order to obtain cardiac motion data, the test person stopped breathing for ca. 15 s, then took several deep breaths and stopped breathing again for ca. 15 s. This was repeated during a period of ca. 90 s. The short time intervals during the intensive breathing were discarded in the subsequent data processing stage.

3.2.3 Data processing

Due to the stationarity of various reflectors in the scene, such as the wall and the floor, the resulting clutter is stationary as well and thus manifests itself as a DC-component in the slow-time direction. On each acquired data set, stationary clutter removal and low-pass filtering (high-frequency noise suppression) in range dimension was performed. For a mathematical description of such steps, see section 5.4. The one-sided amplitude spectrum of the respiratory and cardiac motion for each position was computed on the slow-time vector which produces the largest response. In order to obtain a fair comparison, each am-

plitude spectrum is scaled by the number of acquired range profiles K during the given T_{obs}.

3.2.4 Target feature evaluation under LOS conditions

Human respiratory motion responses as function of (slow-)time in a relaxed state for the three body positions is shown in fig. 3.1(a). The waveforms of the respiratory motion responses were low-pass filtered in range in order to suppress high-frequency noise, which allows for better discernibility.

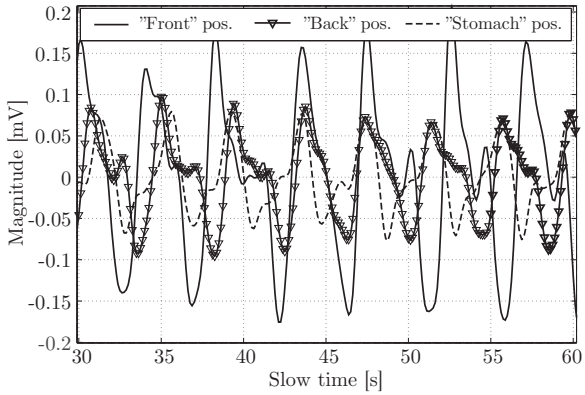

(a) Respiratory motion responses in slow-time domain; low-pass filtered.

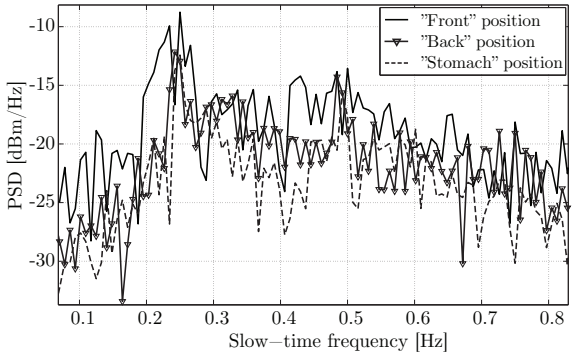

(b) Amplitude spectrum of the respiratory motion responses. Decibel scale.

Figure 3.1: *Responses of the respiratory motion under LOS for three body positions.*

The first obvious result from fig. 3.1(a) is that the "front" position results in the strongest responses. This is explained by the fact that for such position the chest displacement is the strongest and the area of reflection is the largest.

Although it does not exhibit purely sinusoidal behaviour, the majority of the energy in the amplitude spectrum of the respiratory motion responses is located at the fundamental respiratory frequency f_h, see fig. 3.1(b). The response at the first harmonic, located at ca. $2f_h$, is in average 7 dB weaker than the response at f_h. Due to the presence of higher harmonics as well (particularly visible for the "front" position) the conclusion is that the human respiratory motion $\boldsymbol{\delta}[k]$ can be fairly well modeled by the absolute value of a sinusoid: $\boldsymbol{\delta}[k] = -|a_h \cdot \sin[2\pi f_h k + \phi_h]|$, where '$|\cdot|$' denotes the absolute value operation; a_h and ϕ_h are respiratory motion amplitude and phase, respectively. In order to avoid aliasing of higher order harmonics of the respiratory motion, the acquisition frequency f_a should therefore be at least an order of magnitude higher than the expected f_h, i.e. $f_a > 3$ Hz.

Fig. 3.2(b) shows that the human cardiac motion is located at higher frequency (ca. 1.1 Hz) than f_h and that the magnitude of the cardiac motion responses is significantly weaker than that of the respiratory motion responses, in average 13 dB. For the "front" position, the energy ratio $E_{rc} = 14$ dB, for the "stomach" position $E_{rc} = 12$ dB and for the "back" position $E_{rc} = 13$ dB. Fig. 3.2(b) further shows that, in contrast to the frequency domain behaviour of the respiratory motion responses, the magnitude of the higher order harmonics for cardiac motion responses is comparable in size to that of the fundamental frequency of the cardiac motion.

3.2.5 Target feature evaluation under NLOS conditions

Under NLOS conditions, the responses of the respiratory motion are still visible, although in average ca. 40 dB weaker than under the LOS conditions (taking into account the additional 8 dB of transmitted power), see fig. 3.3(a). However, this is not the case for cardiac motion responses, as they cannot be discernible, see fig. 3.3(b). This is the case despite the fact that additional 8 dB of power was transmitted and the fact that the "front" position is shown in fig. 3.3(b), which is expected to produce the strongest responses. The conclusion from the evaluation of the detectability of the respiratory and cardiac motion under LOS and NLOS conditions is that the human cardiac motion is not a reliable target feature for detection of trapped victims buried under rubble, at least not under the severe conditions that commonly occur in real life. This conclusion is valid if using time-domain equipment having comparable dynamic range as the equipment used herein. However, UWB radar devices having significantly larger dynamic range might very well yield different results, as shown in section 2.5.5 using a high-dynamic-range device (the VNA). Due to the unavailability of a dedicated high-dynamic-range radar device, this hypothesis cannot not be fully experimentally verified.

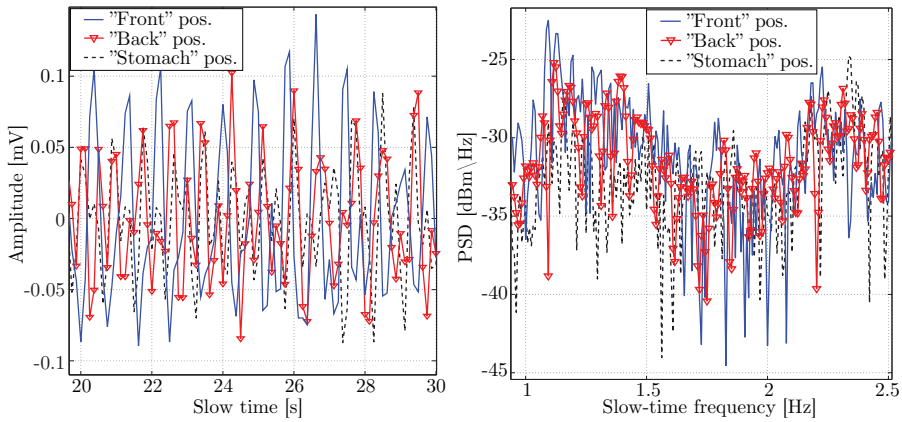

(a) Cardiac motion responses in slow-time domain; low-pass filtered in range.

(b) Amplitude spectrum of the cardiac motion responses.

Figure 3.2: *Responses of the cardiac motion under LOS for three body positions.*

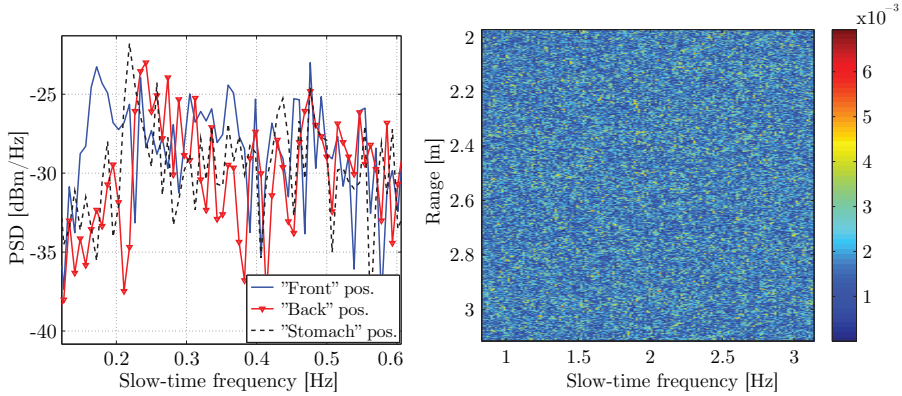

(a) Amplitude spectrum of the respiratory motion responses for three body positions

(b) Radargram of the cardiac motion response for the "front" body position

Figure 3.3: *Results of data processing acquired under NLOS conditions.*

3.2.6 Assessment of the chest displacement due to respiratory and cardiac motion

The insight into the approximate magnitude of the human chest displacement due to respiratory and cardiac motion is needed in order to answer the question concerning what average SNR is obtained for a certain chest displacement and

for a given set of circumstances. The data sets that are used for this assessment are the same as the ones used in the previous section, although processed differently. The phase difference $\Delta\phi$ that arises due to the respiration of the test person is proportional to the difference in the time of arrival Δn^* of the backscattered response from the test person and thereby directly proportional to the chest displacement ΔR according to:

$$\Delta\phi = 2\pi f' \cdot \Delta n^* = 2\pi f' \cdot \frac{2\Delta R}{c_0} = 4\pi f' c_0 \cdot \Delta R \qquad \boxed{3.1}$$

where f' is the frequency that corresponds to the largest value of $\Delta\phi$. The phase variations as function of time are shown in fig. 3.4. The figure shows that the magnitude of the phase offset $|\Delta\phi|$ due to chest displacement is by far the largest for the position for which the chest of the test person is facing the antennas ("front" position), followed by the "stomach" position and the "back" position. The mean magnitude of the phase offset $\overline{|\Delta\phi|}$ for each body position is inserted in eq. 3.1, thus obtaining $|\Delta R| = 3$ mm ("front"), $|\Delta R| = 0.95$ mm ("stomach") and $|\Delta R| = 0.48$ mm ("back"). The average SNR value that has been obtained for the "front" position is 12.8 dB, for the "stomach" position 5.3 dB and 7.4 dB for the "back" position.

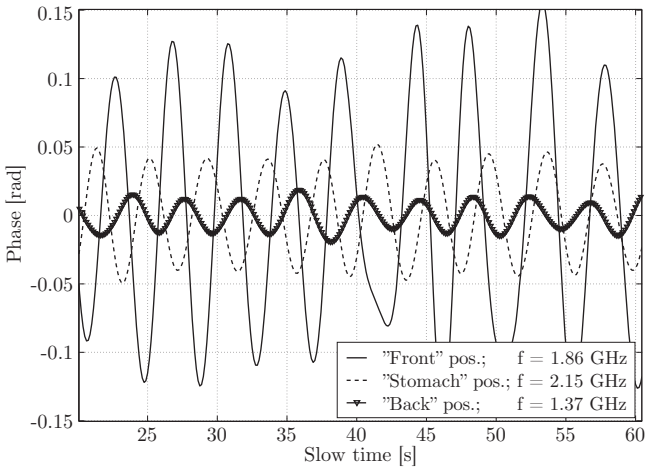

Figure 3.4: *Phase variation as function of time for three body positions*

The reason that the "stomach" position exhibits a lower SNR value than the "back" position despite larger chest displacement, might be due to the fact that the energy of the backscattered response for the "stomach" position was to a larger extent distributed in the range profile, but also that the reflective area is smaller than for the "back" position. Nevertheless, these results indicate that the SNR is directly proportional to the chest displacement, although the

exact SNR value will vary depending on the shape and the exact orientation of the test person, as well as the nature of the breathing of the test person. The assessment of the chest displacement due to cardiac motion could not be carried out since $\overline{|\Delta\phi|}$ could not be estimated due to too low SNR values. It is therefore expected that the chest displacement due to cardiac motion is on the sub-millimeter level.

3.3 Characterisation of the human respiratory motion response as the sole target feature

As we have observed so far, the cardiac motion does not represent a feasible target feature for the detection of trapped victims buried under rubble if using readily available UWB radar equipment. Therefore, the focus needs to be shifted solely on the human respiratory motion as the only available target feature for this particular application. As shown earlier, the magnitude of the response from the chest displacement is proportional to the resulting SNR, which in turn is a monotonic function of the probability of detection of a trapped victim. However, the resulting SNR does not solely depend on the chest displacement, but also on the reflective area of the displacement, as well as the aspect angle θ_a, bi-static angle θ_b and the antenna-pair polarisation p. The obtained respiratory motion responses are analysed both in the frequency- and in time domain (in the range dimension). We further investigate their magnitude (or detectability) as function of θ_a, θ_b, body position and antenna-pair polarisation.

3.3.1 Measurement scenarios

The measurements were conducted in the same cellar as the previous measurements in this chapter. However, the measurement set-up is different and can be seen in fig. 3.5.
Next, a description of the measurement procedure and set-up is given:

- A female test person was placed in horizontal position on a 1m-high polystyrene support centred 2.5 m from a single transmit antenna and four identical receive antennas. The measurement set-up can be seen in fig. 3.5. The test person breaths in a relaxed manner and is otherwise motionless. She starts inhaling on the count of three at which moment the data acquisition begins. Such approach assures that the respiratory starts with the same state of lung for all individual measurements.

- Antennas were directed toward the test person at bi-static angles $\theta_b = -30°$, $\theta_b = -15°$, $\theta_b = 45°$ and $\theta_b = 60°$ with respect to the transmit antenna.

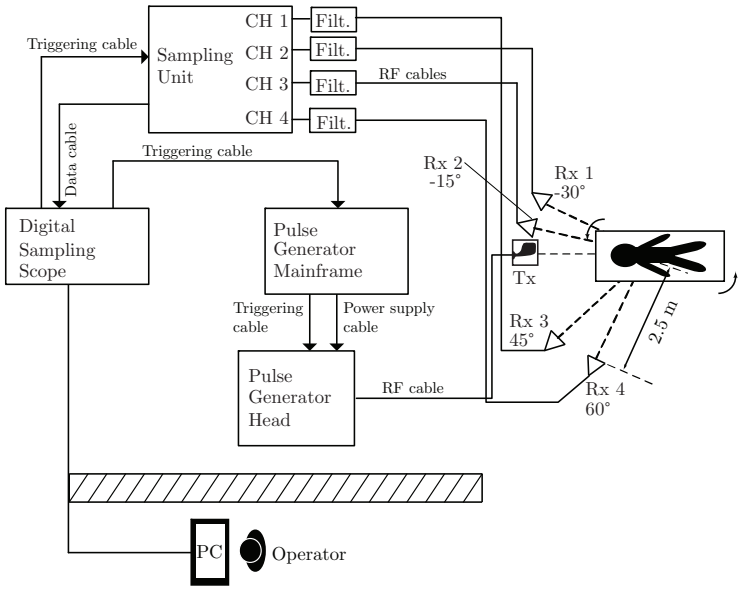

Figure 3.5: *Measurement set-up and main components of the equipment.*

- Each of the four receive channels acquires 64 range profiles. This procedure is repeated for each aspect angle, position of the body and antenna-pair polarisation. The test person is then instructed to turn her body in counter-clockwise direction with 10° angular increment after each set of 64 acquisitions.

- Due to time constraints, it was decided to acquire HH, HV and VV polarised responses. HV is useful only to confirm previously observed results which showed that respiratory motion is significantly weaker for cross-polarised antenna pairs. Thus, acquisition of VH cross-polarised responses do not provide much added value, since there is no significant expected difference between the results for HV and VH.

- Due to availability of only 4 receive antennas, the data for HH and HV antenna-pair polarisations were acquired simultaneously for $\theta_b = -30°$ and $\theta_b = 45°$. The same procedure was later repeated for $\theta_b = -15°$ and $\theta_b = 60°$. The starting position for the receive antenna pairs $\theta_b = -30°$ and $\theta_b = 45°$ and $\theta_b = -15°$ and $\theta_b = 60°$, respectively, was such that the feet of the test person were pointing toward the $\theta_b = -30°$ and $\theta_b = -15°$ receive antenna, respectively. All the considered θ_b were acquired simultaneously for VV antenna-pair polarisation, for which the starting position was feet pointing towards the $\theta_b = -30°$ receive antenna.

- Symmetry is assumed for body positioned on the stomach and the back, so that only a half plane is considered during the supervision (0°-180°: 19 aspect angle positions out of 27 available). For the side position, however, this assumption does not hold in the same way, thus the full plane has to be taken into account. However, because of the symmetry of the human body, it is assumed that the results are independent on which side the test person is resting, thus only one side (left) has been investigated.

- The aspect angle $\theta_a = 0°$ for any given θ_b, represents the position such that the feet of the test person are pointing to the given receive antenna, see fig. 3.6 for $\theta_b = -30°$.

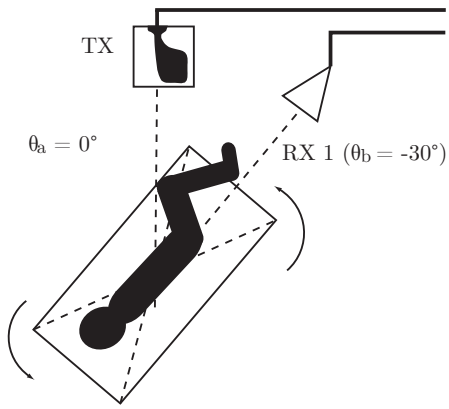

Figure 3.6: *The position of the test person for $\theta_a = 0°$, side position and $\theta_b = -30°$.*

3.3.2 Measurement equipment and parameters

The measurement equipment consisted of Geozondas SD10806 digital sampling converter (see A.1.2), the Geozondas pulse generator GZ1117DN-25 (see A.1.3), the Vivaldi antenna serving as the transmit antenna (see A.4.1), four identical dielectric wedge antennas used as receive antennas (see A.4.2) and four identical analogue band-pass filters (see A.5). The measurement parameters that were used during data acquisition are summarised in table 3.2.

3.3.3 Data processing

Each acquired data matrix $\mathbf{R} = \mathbf{R}[n, k]$ is processed in the same manner as in section 3.2.3: stationary clutter suppression was followed by the linear filtering operation in the range dimension in order to suppress out-of-band noise. However, for the assessment of detectability of the respiratory motion responses

Table 3.2: *Measurement and data processing parameters*

Parameter name	**Value**
Effective sampling frequency f_s	200 GHz
Time window T_w	10 ns
Number of samples/range profile N	2000
Number of range profiles/dataset K	64
Acquisition frequency f_a	2.22 Hz
Averaging L	256
-10dB bandwidth B	880 MHz
Digital frequency band	200 MHz-1800 MHz

(described in section 3.3.6), two additional data processing steps were added. This had to be performed due to the fact that the SNR is very low for a significant number of data matrices $\mathbf{R}$, thus the noise needs to be reduced in order to more accurately assess the magnitude of such weak responses.

The first processing step applies a rectangular window in the slow-time frequency domain in order to suppress the energy at frequencies which do not contain the respiratory motion response, i.e. that contain only the noise energy. For additional noise suppression, the singular value decomposition (SVD) method was used with the order $J = 3$, resulting in the processed data matrix $\mathbf{H}_{J=3}[n, k]$. The energy of the respiratory motion responses found in $\mathbf{R}$ is preserved in $\mathbf{H}_{J=3}$, due to the chosen value of J. For the detailed explanation and the motivation for the use SVD, as well as the mathematical description of the two additional data processing steps, see sections 5.6 and 5.7. The significant benefit from the data processing steps can be seen in fig. 3.7.

3.3.4 Respiratory motion responses in time domain

Time-domain representation of respiratory motion responses illustrates how the respective waveforms, as well as the late-time multiple responses, vary for various measurement conditions. We have chosen to show the strongest occurring respiratory motion responses for the side position of the body for four bi-static angles, as well as for HH and VV co-polarisation, respectively, see fig. 3.8. Each graph was offset with respect to the others in order to avoid overlap.

What can be observed is that for HH co-polarisation the magnitude of the shown responses varies to a lesser degree than for the VV co-polarisation. Regarding the shape of the early-time waveforms it can be noted that although the polarity of the waveforms can differ, there is nevertheless some degree of correlation across all the shown waveforms. This is not surprising since we only consider a single test person. It is expected that other persons might produce somewhat stronger or weaker respiratory responses, depending on the breathing pattern, chest displacement and reflective area. However, the difference in shape

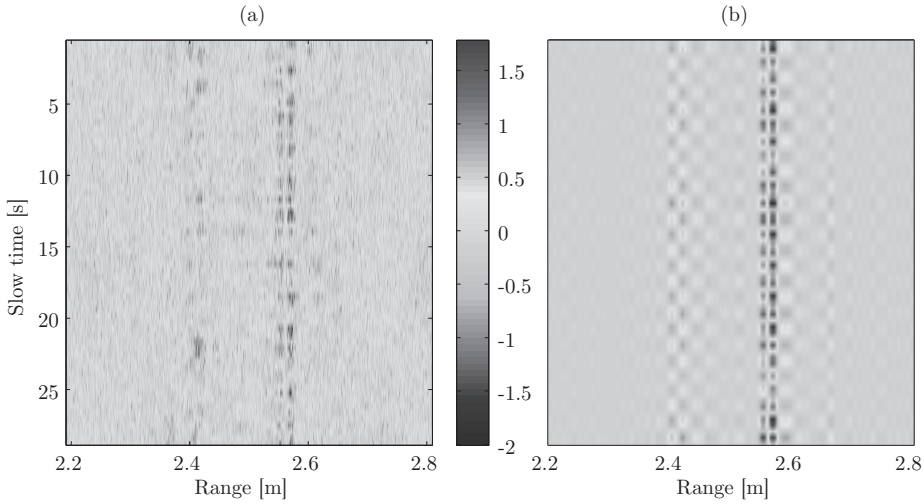

Figure 3.7: *Comparison between: a) a segment of unprocessed data matrix* $\boldsymbol{R}$ *and b) the equivalent segment of the processed data matrix* $\boldsymbol{H}_{J=3}$*; amplitude in* mV*.*

of the respective waveforms under the exact same conditions should be minor. This is motivated by the fact that all humans share the same tissue properties, which can typically only vary in size and shape. The late-time responses seen in fig. 3.8 do differ as well, although there is an obvious strong correlation between e.g. $\theta_b = -30°$ and $\theta_b = 60°$ for VV co-polarisation.

The late-time responses are a result of multiple reflections from the moving parts of the body due to breathing (chest, abdomen) and the adjacent body parts (arms, legs). The magnitude of the late-time reflections depends much on the position of the body and the position of the body parts (such as arms) in relation to the chest and the abdomen. Due to this reason, the arms, for instance, can experience a slight periodic motion due to breathing, depending on the position of the body. This can then result in a reflection centre aside from the one originating from the chest or abdomen and which occurs earlier or later in time, depending on the position of the body in relation to the antennas. This is illustrated in fig. 3.7 where the first reflection centre occurs at the range of 2.4 m and the second one at ca. 2.6 m. Despite the fact that the late-time responses experience a long time of duration under LOS conditions, their time of duration in rubble is expected to be significantly shorter. This is expected since the attenuation factor of rubble is considerably higher than that of free space, resulting in significantly stronger attenuation of the late-time responses. This is in fact beneficial since the late-time responses can interfere destructively with the respiratory response waveform of a potential, nearby trapped victim, thus making its detection increasingly difficult.

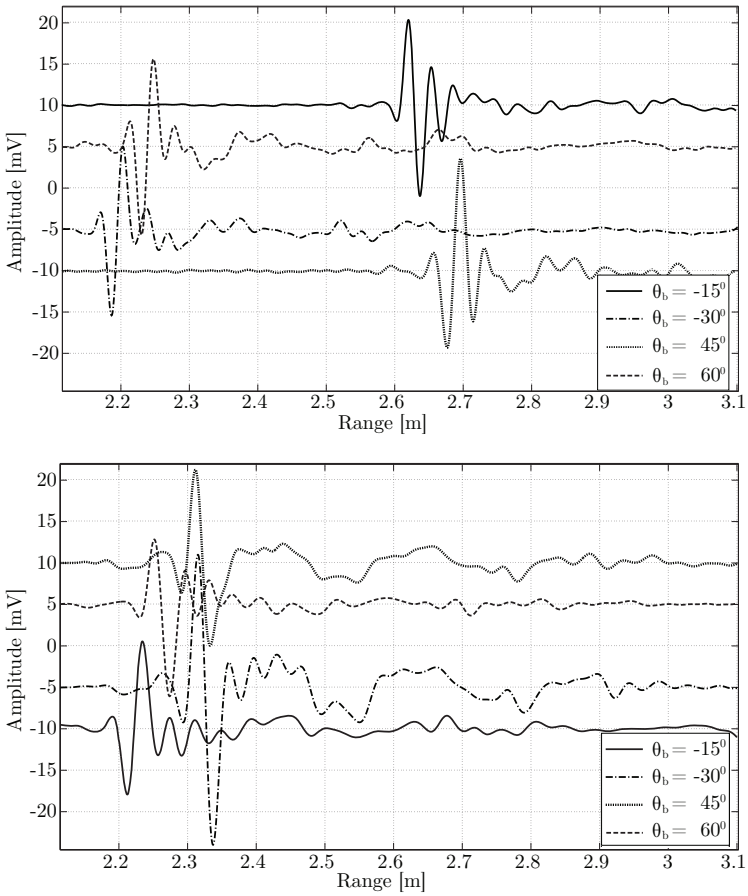

Figure 3.8: *Range profiles containing the strongest occurring respiratory motion responses for the side position, all θ_b and a) HH and b) VV co-polarisation*

3.3.5 Respiratory motion responses in frequency domain

In this section we have chosen to present the spectrum in the frequency range of interest (0.5 - 5 GHz) of a number of respiratory motion responses for a small number of varying measurement conditions. This is done in order to show which part of the spectrum the respiratory motion responses are occupying and which frequencies are most affected by varying the measurement conditions. We have chosen to consider $p = \text{HH}$ and $\theta_b = -30°$. Fig. 3.9(a,c,e) shows the normalised spectrum as function of θ_a for HH co-polarisation for all three body positions. Each row in a subfigure of fig. 3.9 represents the average spectrum of $\mathbf{H}_J$ for a given θ_a.

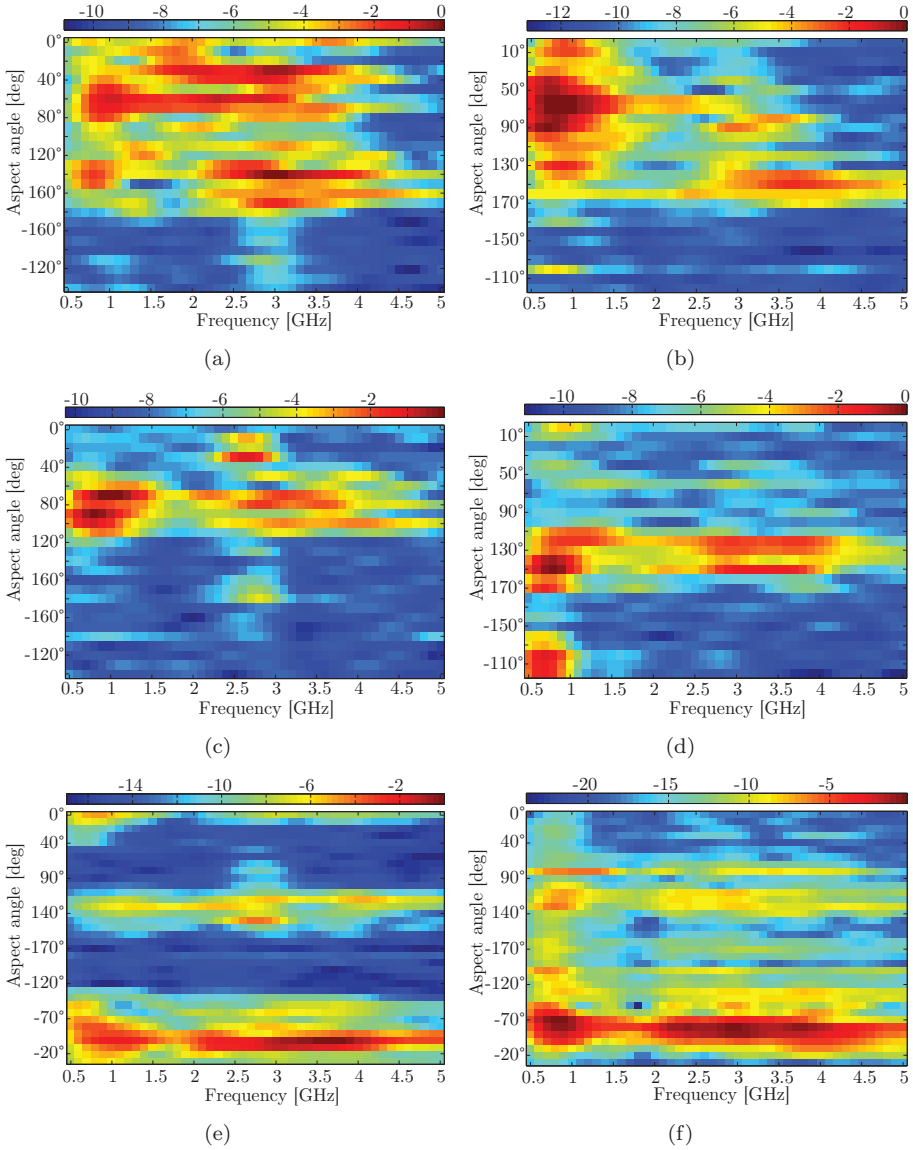

Figure 3.9: *Normalised spectrum in dB as function of θ_a for the: "stomach" position, (a) p=HH and (b) p=VV; "back" position (c) p=HH and (d) p=VV; "front" position, (e) p=HH and (f) p=VV; $\theta_b = -30°$*

In case the respiratory motion responses are present (which are aspect-angle dependent), the frequency range in which the majority of the energy is confined

can be divided in two: from ca. 0.5 GHz until ca. 1.5 GHz and from ca. 2.5 GHz until ca. 3 GHz. The lower frequency range is the most interesting one for detection of trapped victims since the rubble attenuation for that frequency range is expected to be lower than for the higher frequency range. Similar behaviour can be observed for the VV co-polarisation as well (see fig. 3.9(b,d,f)), where the spectrum in the lower frequency range is even more dominating than in the case of HH co-polarisation. This leads to the conclusion that all the frequencies not belonging to the lower frequency range should be filtered out by means of an analogue filter (or equivalently using a radar system operating in that frequency band).

3.3.6 Detectability of respiratory motion responses

In this section we investigate how detectable the target is, i.e. we investigate the magnitude of the respiratory motion responses as function of θ_a, θ_b, p and the body position. Since the magnitude of the respiratory motion responses is directly proportional to the chance of detecting the victim, it is a very important feature of the target for which more knowledge needs to be obtained. The analogous term to detectability in the realm of the conventional radar systems is the target radar-cross section. However, in our case, the magnitude of the useful target feature is not only the combination of the reflectivity of the moving parts of the target, its area and the directivity of the reflections from the moving parts of the target, but it is also directly proportional to the displacement of the movement. This does not apply to the case of conventional radar targets. This aspect, along with the fact that the measurements are done under near-field conditions (in particular for lower frequencies), makes the expression of the detectability in terms of area, as in the case of conventional radar targets, less meaningful. Instead, we have chosen to put all the averaged magnitude values of the respiratory motion responses in a relation to the largest average magnitude value that has been observed. Thereby, the choice of the definition of detectability D of the radar-induced respiratory motion responses is the following:

$$\mathbf{D}_{\theta_b,b,p}(\theta_a) = 20 \cdot \log_{10}\left(\frac{1}{K}\sum_{k=1}^{K} \max_{n\in\{n_v \pm N^*/2\}} \{|\mathbf{H}_J[n,k]|\} / D_{max}\right) \qquad \boxed{3.2}$$

where the index b denotes the position of the body and n_v is the range index of the respiratory motion response. The peak value of each range profile in $|\mathbf{H}_J|$ is obtained from the same N^*-sized range bin as the respiratory motion response. The normalisation factor D_{max} is the maximum obtained detectability value for all $\mathbf{H}_J$, including all body positions, antenna-pair polarisations, θ_b and θ_a. This value corresponds to the "front" body position with the chest facing the $\theta_b = -30°$ receive antenna (i.e. $\theta_a = -70°$) for VV antenna co-polarisation. By definition, this position is associated with the detectability value $D = 0$ dB.

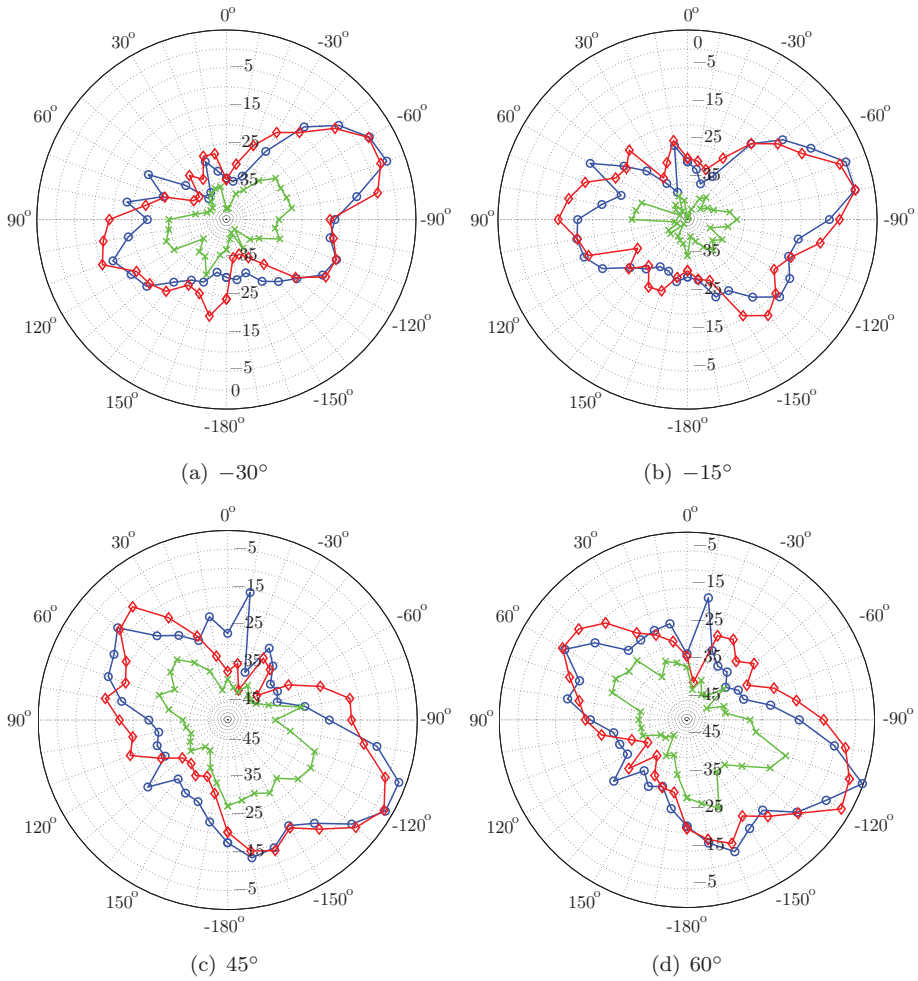

Figure 3.10: *Detectability as function of θ_a for the "front" body position and: (a) $\theta_b = -30°$, (b) $\theta_b = -15°$, (c) $\theta_b = 45°$ and (d) $\theta_b = 60°$; HH is described by the diamond-shaped marker, VV by the circular-shaped marker and HV by the cross-shaped marker.*

Detectability of respiratory motion responses when lying on the side

The position such that the test person is lying on the side, i.e. $b =$ "front", has been found to produce the strongest detectability values D, for all p. This is seen from fig. 3.10 (a-d) which shows $\mathbf{D}_{\theta_b,\text{"front"},p}(\theta_a)$ for all p and θ_b. The fact that D is as strongest for the "front" position is expected, since the human

chest expands radially upon inhalation and is mostly pronounced in the frontal-, and to a lesser extent, backward direction. If the body is positioned such that the chest is turned toward an RX antenna, this then produces larger D values. If the chest is additionally illuminated by the TX antenna in LOS (i.e. no significant attenuation occurs from any adjacent body part), then such position is optimal. This is the case in particular for small θ_b, which explains why the peak detectability values are slightly larger for $\theta_b = -30°$ and $\theta_b = -15°$ than for $\theta_b = 45°$ and $\theta_b = 60°$. The aspect angles θ_a that produce significantly weaker D are those where the body parts (i.e. head, legs) attenuate significant amount of the illuminating energy. The attenuation can amount up to 35 dB, as can be seen from fig. 3.10 (a-d). However, it can be argued that part of the decrease in D can be attributed to smaller chest displacement and smaller reflective area for such θ_a. This effect is particularly pronounced if the bottom or the top part of the chest is facing a receive antenna, since the expansion of the chest is significantly less pronounced in those directions.

Whereas there seems to be little average difference in D between the two co-polarisations $p =$ "HH" and $p =$ "VV", it can be instantly observed from the figures that $p =$ "HV" results in tens of decibels weaker D than the other two antenna-pair polarisations. A possible reason might be that since the reflection from the body occurs mainly at the skin layer, i.e. the radiated waves do not penetrate the tissue to any significant levels, thereby avoiding any change in polarisation state due to phase shift. The fact that the cross-polarised responses are significantly weaker than the co-polarised ones can be highly useful in suppressing non-stationary clutter, in particular the moving scatterers that typically produce cross-polarised responses, such as rattling leaves and branches.

Detectability of respiratory motion responses when lying on the stomach

While observing the detectability figures for the "stomach" position, namely fig. 3.11 (a-d), the first obvious difference compared to the "front" position is that there are 9 detectability values missing, for all p. The reason is that the assumption of existence of symmetry for body resting on the stomach is invalid (the same applies for the "back" position). The reason is that for any two symmetric θ_a the illumination angle is different, thereby leading to different detectability values. However, this became clear only after processing the acquired data. Repeating the measurements was deemed not feasible. Lying on the stomach results in lower detectability values (10-15 dB) compared to the "front" position due to several reasons:

- The chest cavity does not have full freedom of expansion, as in the case of the "front" position.

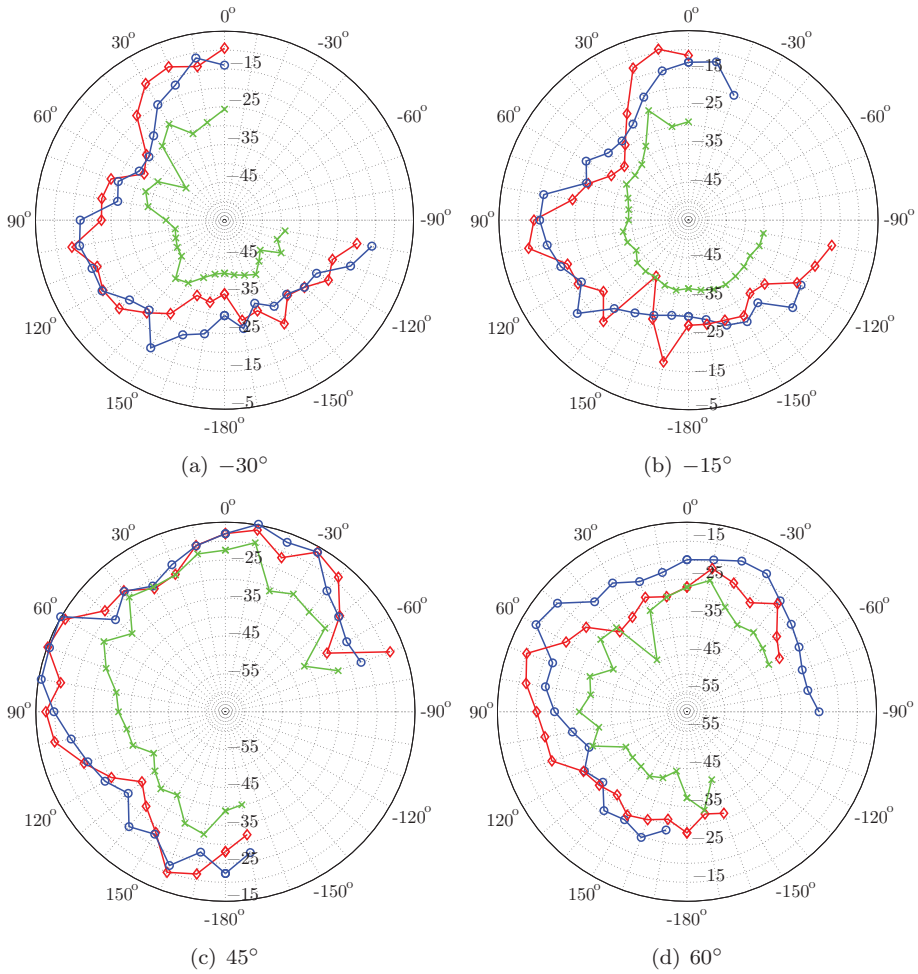

(a) $-30°$ (b) $-15°$

(c) $45°$ (d) $60°$

Figure 3.11: *Detectability as function of θ_a for the "stomach" body position and: (a) $\theta_b = -30°$, (b) $\theta_b = -15°$, (c) $\theta_b = 45°$ and (d) $\theta_b = 60°$; HH is described by the diamond-shaped marker, VV by the circular-shaped marker and HV by the cross-shaped marker.*

- The respiratory motion is mostly pronounced in the frontal direction of the chest and significantly less toward the sides.
- Lying on the stomach results in smaller reflective area.
- For the "stomach" position, the arms are attenuating parts of the illuminating energy and the reflected energy from the chest.

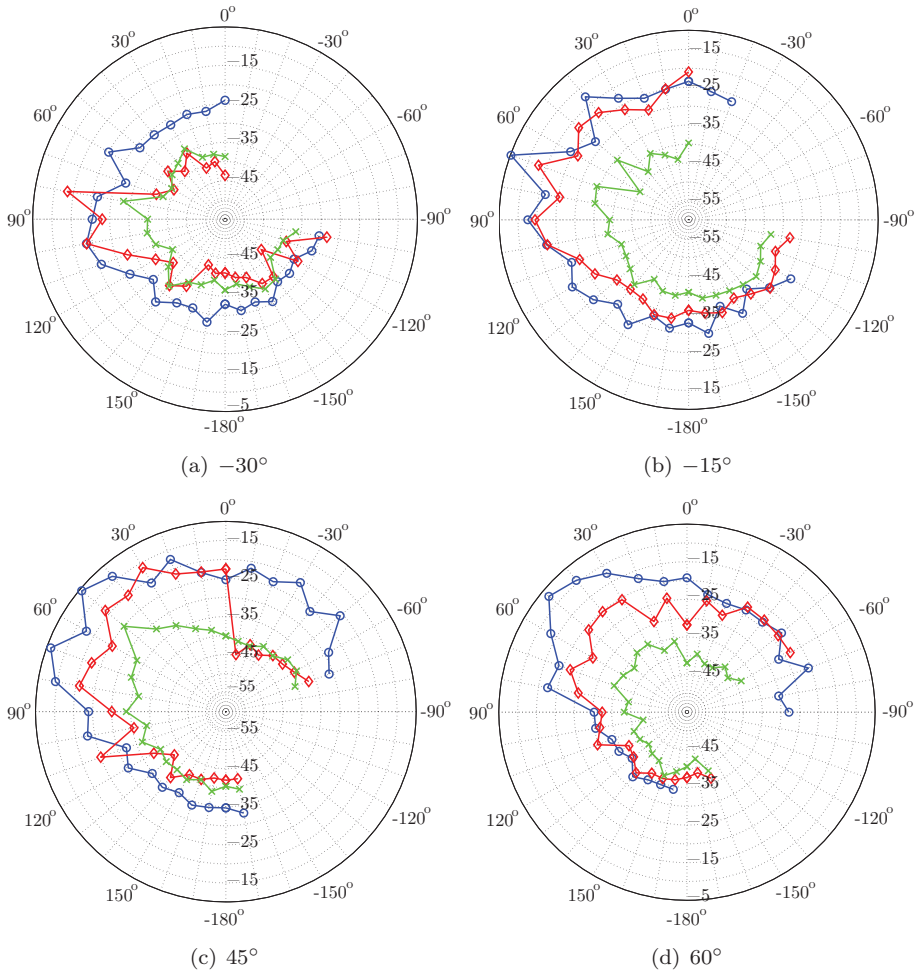

Figure 3.12: *Detectability as function of θ_a for the "back" body position and: (a) $\theta_b = -30°$, (b) $\theta_b = -15°$, (c) $\theta_b = 45°$ and (d) $\theta_b = 60°$; HH is described by the diamond-shaped marker, VV by the circular-shaped marker and HV by the cross-shaped marker.*

Aside from the lower detectability value for the "stomach" position, it is also evident that there is much less variation in the detectability pattern compared to the "front" position. This can be explained by the lack of full-LOS illumination of the chest for the "stomach" position. A further likely cause to the lower variation in the detectability pattern compared to the "front" position can be attributed to the fact that sideways chest displacement is less articulated com-

pared to the frontal direction.

Detectability of respiratory motion responses when lying on the back

The detectability pattern for the "back" position is in many ways very similar to the one of the stomach, although the "back" position seems to produce slightly lower detectability values than the "stomach" position, as can be seen from fig. 3.12 (a-d).

Statistical distribution of detectability values for HH, VV and HV antenna-pair polarisations

A qualitative insight into the effects of the antenna-pair polarisation on the detectability of respiratory motion responses under LOS conditions is given by comparison of the probability density function (PDF) and cumulative distribution function (CDF), respectively, of the respective detectability values for HH, VV and HV.

Fig. 3.13(a) shows the best fit of the PDF for the respective detectability values. The closeness of the fit can be visually inspected by observing the CDF in fig. 3.13(b). The probability distribution that fits the data best in maximum-likelihood sense is the generalised extreme value (GEV) distribution. The GEV distribution corresponds to the distribution of maxima of long, finite sets of random variables [1], as is the case here. The parameters that describe the distribution are: μ (mean value), σ (standard deviation) and ξ (skewness; measure of the asymmetry of the PDF). The respective parameters of the distribution for each p can be seen in table 3.3. The data shown both in the two figures and the table confirm that the co-polarised antenna pairs produce significantly higher detectability values than the cross-polarised equivalent. There is no large difference between HH and VV co-polarisation in terms of mean value, however, the variance of HH is slightly larger.

Parameters	**HH**	**VV**	**HV**
Location μ	-29.1	-26.9	-38.6
Scale σ	8.6	6.4	3.7
Skewness ξ	-0.193	$-77.9 \cdot 10^{-3}$	$15.8 \cdot 10^{-3}$

Table 3.3: *Parameter values in dB for the distribution of detectability values for the HH, VV and HV antenna-pair polarisation.*

3.4 Conclusion

This chapter presents a thorough experimental study on the only two potential target features for use in UWB-radar-based trapped-victim detection, which

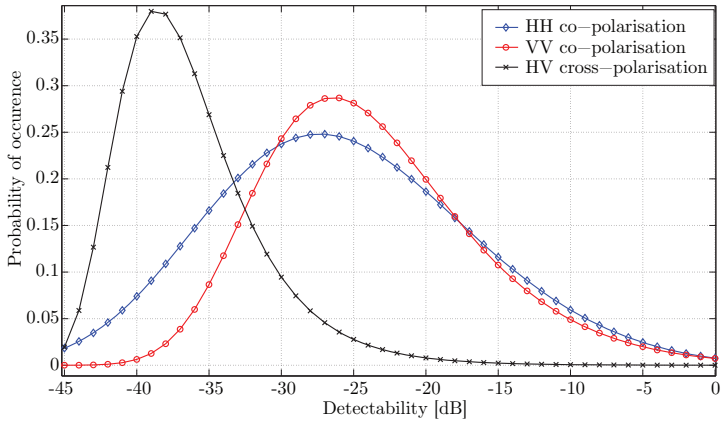

(a) The closest fit of the probability density function

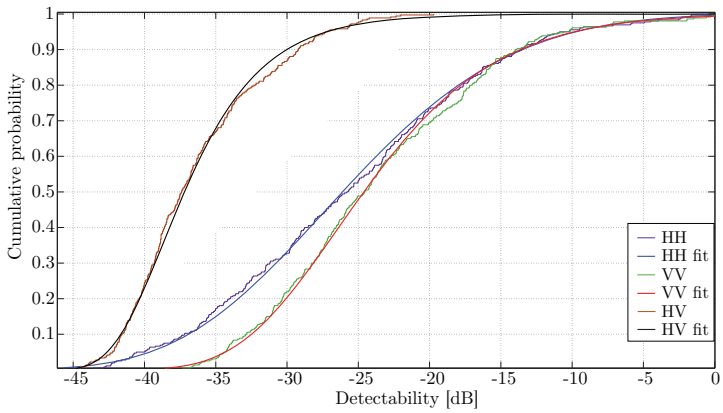

(b) Cumulative distribution function and the closest fit

Figure 3.13: *PDF and CDF of the detectability values for HH, VV and HV*

are respiratory- and cardiac motion. Two measurement campaigns provided high-quality data for the analysis. One of the first results to emerge was, quite expectedly, that respiratory motion responses are the sole target feature feasible for trapped-victim detection under real-life conditions (this holds if time-domain radar equipment is used), being in average 13 dB stronger then cardiac motion responses. The study further investigated the chest displacement due to both respiratory- and cardiac motion, for three body positions. It showed that the chest displacement due to respiratory motion varies from a half to 3 mm, whereas the SNR values were too low for the chest displacement due to cardiac motion to be assessed. The second measurement campaign provided a highly extensive

amount of data, which is unique in its scope and in the number of investigated parameters. Analysing the data in time domain by comparing a small number of waveforms belonging to the strongest obtained respiratory motion responses and their associated late-time responses, showed that there is some correlation between the investigated waveforms and the late-time responses. However, in order to make benefit of this fact by implementing an adaptive matched filter with the aim of maximizing the resulting SNR, requires a significant amount of additional research, which is out of scope of the research conducted in this thesis. Frequency domain analysis of the same data sets showed that a bandwidth of ca. 1 GHz centred at 1 GHz is an appropriate operational frequency band (for the particular antenna type used herein), both from the point of view of the spectrum of the responses, but also taking into account the typically lower rubble attenuation in that region of the spectrum. The most elaborate analysis involved assessment of the detectability of human respiratory motion responses as function of aspect angle, antenna-pair polarisation, body position and bi-static angle. Detectability is defined as the time-average value of the magnitude of the respiratory motion responses normalised to the highest obtained average value including all datasets. The obtained results of the detectability assessment show that:

- For the position in which the test person is resting on its side and facing the receive antenna, the respiratory responses are strongest, regardless of antenna-pair polarisation and bi-static angle. The other two positions, back and stomach, tend to be in average 10-15 dB weaker due to smaller chest displacement and smaller reflection area.
- All investigated bi-static angles exhibit comparable levels of detectability.
- The attenuation of the various body parts surrounding the chest (including unfavorable positions of the chest in relation to the receive antenna) can be severe and amount up to 35 dB.
- No considerable difference exists between the HH and VV co-polarisations, but it has been observed, however, that VV co-polarisation produces slightly higher levels of detectability, but somewhat smaller standard deviation. Cross-polarised antenna pairs, on the other hand, generally produce weak responses and should thus be avoided in real-life operational modes.
- Detectability values for each antenna-pair polarisation is distributed according to the generalised extreme value distribution.

The extent of the acquired database of human respiratory motion responses and the obtained results, represent a unique and highly novel approach to classify the respiratory motion responses as the most important target in UWB-radar-based trapped-victim detection operations. To the author's best knowledge, such extensive database is the first of its kind.

References

[1] E. Weisstein, “Extreme Value Distribution,” ”From MathWorld–A Wolfram Web Resource”, http://mathworld.wolfram.com/ExtremeValueDistribution.html, 2007-2008.

4

Operational frequency band

One of the most important questions that need to be answered in UWB-radar-based trapped-victim detection operations is: "what is the optimal operational frequency band?". Since the transfer function of the human body and the various materials that the rubble is comprised of is not completely flat across the operational bandwidth, the choice of centre frequency and bandwidth has an effect on the resulting SNR. Since SNR is a monotonic function of the probability of detection, the aim is to indicate the optimal operational frequency band such that it provides the largest average SNR value with high likelihood using commercially available radar equipment and antennas. In this chapter the approach to determine the most appropriate operational frequency band is to investigate the transfer function of various types of rubble and a reinforced concrete wall. Furthermore, the SNR values of the respiratory motion responses involving the use of such obstacles are evaluated as function of bandwidth and centre frequency.

4.1 Attenuation assessment of obstacles

Three common obstacles were analysed in terms of their attenuation as function of frequency: two piles of rubble and a 60 cm reinforced concrete wall (in this thesis commonly serving as an obstacle during indoor NLOS measurements). Although the data was acquired using different equipment (for details, see later), the approach to data processing was the same. The acquired data set consists of K_a range profiles $\mathbf{r}$ acquired such that the radiated electromagnetic waves have passed the obstacle under test. Additionally, K_a range profiles $\mathbf{r}_0$ have been acquired under LOS conditions, which serve as reference for the deconvolution operation. The magnitude of the transfer function $|\mathbf{H}[\mu]|$, i.e. the attenuation vs. frequency, is obtained by means of deconvolution in the frequency domain (the phase information is discarded):

$$|\mathbf{H}[\mu]| = 20 \cdot \log_{10} \left\{ \frac{|\mathbf{R}[\mu]|}{|\mathbf{R}_0[\mu]|} \right\} \quad \text{dB} \tag{4.1}$$

where $\mathbf{R}[\mu] = \mathrm{DFT}\left\{\sum_{k=1}^{K_a} \mathbf{r}_k[n]\right\}$ and $\mathbf{R}_0[\mu] = \mathrm{DFT}\left\{\sum_{k=1}^{K_a} \mathbf{r}_{0,k}[n]\right\}$. The reference range profiles $\mathbf{r}_0$ were acquired such that the transmit and receive antennas were resting on a concrete floor facing each other and were separated by the equal Tx-Rx distance as in the case of $\mathbf{r}$. The reason that the antennas were resting on the concrete floor is that the properties of an UWB antenna are dependent on the material with which the antenna is in direct contact with. This is the reason why it is deemed more favourable to perform the reference measurement such that the material under test covers the half space under the antenna instead of conducting it in complete absence of the material. Frequencies slightly higher than the lowest operating frequency of the antenna are avoided due to errors stemming from the near-field conditions.

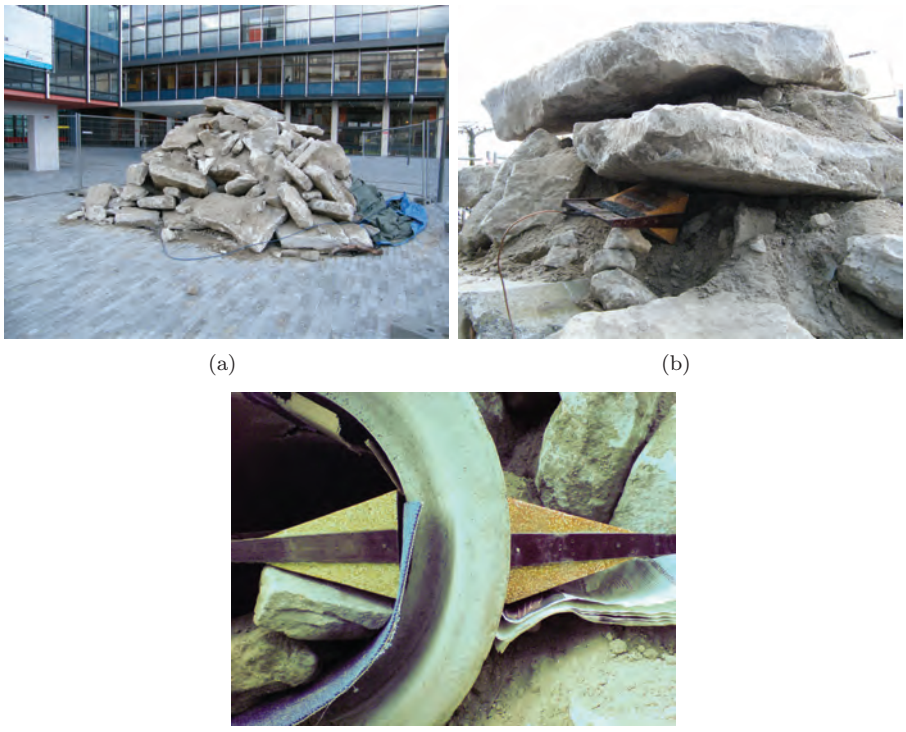

(a) (b)

(c)

Figure 4.1: *Obstacle 1: rubble made of randomly oriented and shaped sandstone blocks resting partly on a) the ground and b) a sewage shaft (seen in the lower left corner). Subfigure c) shows the antenna set-up for the sewer pipe attenuation assessment.*

4.1.1 Obstacle 1: sandstone rubble

The pile of rubble was constructed from randomly oriented and sized sandstone blocks, ca. 20 cm in thickness, mixed with slightly moist sand. The blocks were resting on top of a sewer shaft made of reinforced concrete, see fig. 4.1(b). Additionally, the attenuation of a sewer pipe with 50 cm inner diameter and 18 cm thick reinforced concrete walls was investigated. The used equipment included a HP 8753D VNA (see A.3.1) and a pair of dielectric wedge antennas (see fig. A.4.2).

The attenuation for each Tx-Rx distance as function of frequency can be seen in fig. 4.2(a). It is evident that the attenuation is less for lower frequencies, as expected, but that it rarely exceeds 10 dB. The periodically occurring ripples originate from the fact that the calibration of the VNA was performed without the addition of RF cable and antennas, as in paragraph 2.5.5. The fact that the reference measurements did not cancel out the ripples is most probably due to the fact that they were performed with a different length of the RF cables than during the through-rubble transmission measurements. As was the case with the results obtained in paragraph 2.5.5, the reason for the presence of notches was realised too late in order to redo the measurements with the same length of cables.

It is interesting to note that the attenuation is not largely dependent on rubble thickness. This is particularly evident for the Tx-Rx distance of 90 cm, which, contrary to the expectations, experiences larger attenuation than longer Tx-Rx distances. A possible explanation is that part of the electromagnetic wave propagated through the top of the sewage shaft, which results in higher attenuation than propagation only through sandstone. This is further supported by the attenuation curve for the Tx-Rx distance of 18 cm (the reinforced concrete sewer pipe). Despite this relatively short distance, the attenuation is larger than for larger distances for the case of sandstone material. This is best explained by considering the round geometry of the pipe and its composition, which makes the attenuation relatively high. During radar measurements for USAR purposes, one should therefore avoid placing the test person inside a sewage pipe due to its very high attenuation and the fact that it does not constitute a realistic obstacle.

4.1.2 Obstacle 2: reinforced 60 cm concrete wall

The second obstacle that was analysed in terms of its attenuation in frequency domain is a 60cm-thick, reinforced concrete wall located in the cellar of the Electrical Engineering building of Delft University of Technology. In the absence of real-life-like rubble, this wall was frequently used as an obstacle for various UWB radar measurements in this thesis.

The used measurement equipment was the same as for the previous set-up. The transmit antenna was in direct contact with the wall and resting on a 1m-

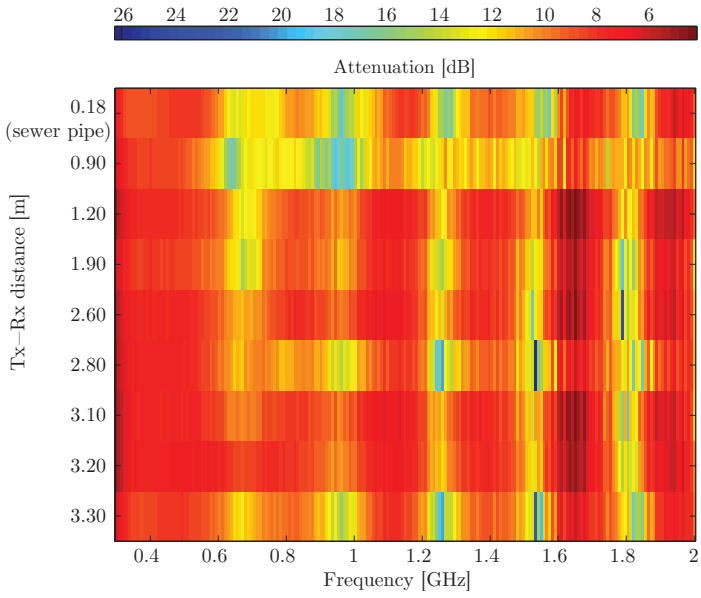

(a)

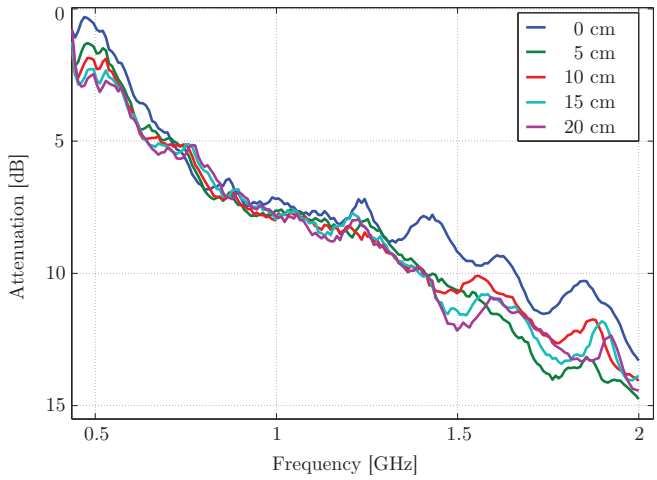

(b)

Figure 4.2: *(a) Attenuation vs. frequency of sandstone rubble and a sewer pipe for various Tx-Rx distances; (b) Attenuation vs. frequency of the 60cm-thick concrete wall for 5 distances between the receive antenna and the wall;*

high polystyrene foam. The receive antenna was placed on the opposite side of the wall at five different distances: from 0 cm to 20 cm with 5 cm increments relative to the wall surface. A single averaged range profile was acquired for each antenna position. The reference measurements were acquired for the same set of distances such that the antennas were resting on the floor.

The attenuation of the wall for the 5 Rx antenna positions can be seen in fig. 4.2(b). It is evident from the figure that the attenuation is regressing almost linearly, reaching in average ca 14 dB at 2 GHz. It is also evident that the distance of the Rx antenna from the wall does not have any large influence up to ca. 1.25 GHz. For frequencies higher than 1.25 GHz the attenuation becomes lower in case the Rx antenna is in direct contact with the wall. This fact is one of the strongest motivations for resting the antennas on the rubble during UWB-radar-based trapped-victim detection operations.

It is noteworthy to explain the reason for the absence of notches in the frequency domain for this particular measurement. The absence of the notches is due to the fact that the length of the RF cables was the same both during the through-wall transmission- and reference measurements, thus canceling them out.

4.2 Assessment of the optimal frequency band for various obstacles

Signal-to-noise ratio (SNR) of the respiratory motion responses depends both on the operational bandwidth and on the centre frequency. This is intuitive since the spectral noise power is proportional to the bandwidth. However, since the transfer function of the rubble and the human body are not constant across the operational frequency band, it is not clear at which frequency the operational bandwidth should be centred. This is investigated herein by means of an experimental study which involves common materials that rubble can be composed of, such as concrete blocks, and modeled as, such as a thick concrete wall.

4.2.1 Data acquisition and set-up

The set-up and the equipment that were used during the experimental study are as follows:

- **Rubble made of concrete slabs**
  A female test person was resting on the back facing two double-ridged horn antennas (see A.4.3) in a cavity 80 cm below the antennas. The obstacle was constructed from non-reinforced concrete plates and slabs, see fig. 4.3(a). Meodat m-sequence radar (see A.2) connected to a laptop was used for the data acquisition. A dataset of respiratory motion data was collected for a period of a couple of minutes.

- **Shelter constructed of reinforced concrete**
  A motionless male test person was resting on the floor with the chest facing up at two meters under the ceiling of a reinforced concrete shelter. The thickness of the concrete slab making up the roof of the shelter is 15 cm. Two double-ridged horn antennas (the same as during the previous set-up) were placed on top of a 20 cm reinforced concrete slab, which in turn was resting on top of the shelter and directly under the test person, see fig. 4.3(b). The test person was resting halfway between the antennas, with an angle of ca. 15° to the centre of each antenna. The same equipment was used as in the previous set-up.

- **60 cm reinforced concrete wall**
  The equipment that was used during the wall attenuation assessment study is a pair of dielectric-wedge antennas and the Geozondas SD-303NF sampling converter along with the GZ1117AN pulse generator (see A.1.3). A male test person was resting on a 1m-high polystyrene foam 1.2 m from the wall, at the same height as the antennas located at the other side of the wall. A dataset of respiratory motion data was collected for a couple of minutes.

(a) (b)

Figure 4.3: *a) Person resting under 80cm-thick layer of concrete slabs; b) Concrete shelter with a reinforced concrete slab resting on the roof of the shelter.*

4.2.2 Data processing

Prior to any further data processing, the acquired data sets were truncated to the same length (i.e. same K). The first step of processing involves stationary clutter removal, see section 5.4. A digital filter is then applied on each range profile in the dataset and the SNR is computed. The SNR is evaluated for the frequency range $f_c \pm B/2$, where $B \in \{0.4, 0.6, \ldots, 1.4\}$ GHz. All SNR values were normalised to the highest occurring SNR value for all evaluated combinations of f_c and B.

4.2.3 Results

The result for the case of the concrete shelter and the concrete rubble are fairly similar and can be seen in fig. 4.4(a) and fig. 4.4(b), respectively. The similarity is not surprising since the same set of equipment was used and somewhat similar obstacle material. The results show that with the use of the ridged horn antennas the relative SNR is the highest for $f_c = 500$ MHz and $B = 400$ MHz and drastically decreases for decreasing and increasing f_c and increasing B. The results for the case of the 60 cm reinforced concrete wall, seen in fig. 4.4(c), show that using dielectric wedge antennas the optimal frequency band is centred at higher f_c than in the case of the ridged horn antennas. This is explained by the fact that the used dielectric wedge antennas are not radiating efficiently for frequencies lower than ca. 300 MHz, which is not the case for the ridged horn antennas used in the previous two cases. One can also see that the SNR drop with increasing or decreasing f_c is not as sharp as in the case of the ridged horn antennas. This can be attributed to the ultra-wideband properties of the dielectric wedge antennas and the electromagnetic properties of the wall.

The three figures indicate that the value of the centre frequency should be lower than ca. 1 GHz in order to maximise SNR. This is further supported by fig. 4.2(a) and fig. 4.2(b), which show lower attenuation for lower frequencies. For the cases of high f_c and low B one notices a plateau in the range of ca. -12 to -14 dB. This plateau is the result of operating almost entirely on noise, since the energy of the backscattered responses is heavily attenuated in that frequency region.

Regarding the operational bandwidth, it is important to state that ultra-wide bandwidths are not necessary for resolving minute motion of concealed trapped victims. In fact, as seen from the results, the bandwidth of 400 MHz produced highest SNR value, which actually was the lowest investigated bandwidth. However, it is important to add that large bandwidths are needed for resolving non-stationary clutter from the respiratory motion response from the victim, as well as being able to separate two or more closely spaced trapped victims.

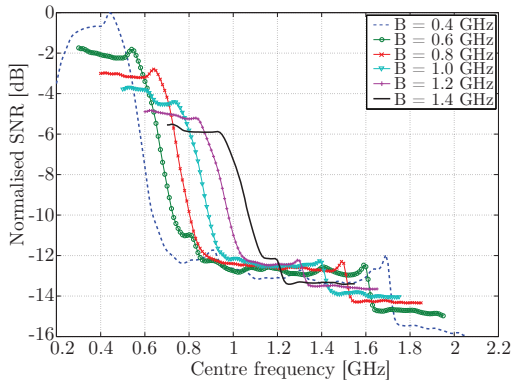

(a)

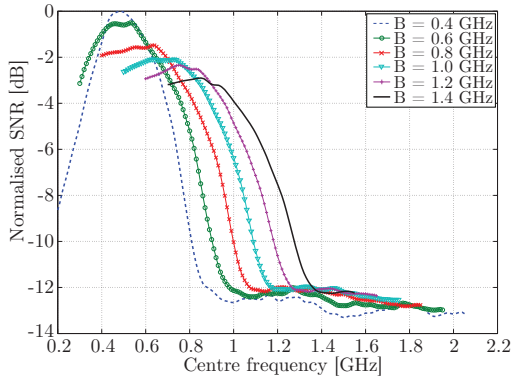

(b)

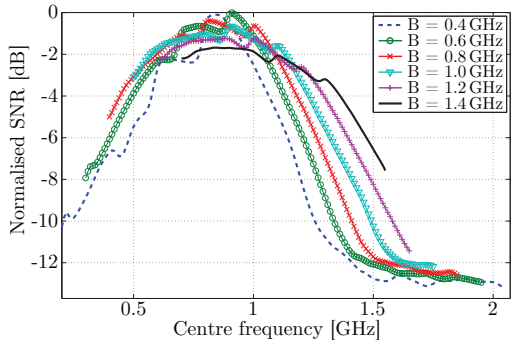

(c)

Figure 4.4: *Normalised SNR as function of centre frequency and operational bandwidth evaluated for a) concrete shelter b) concrete rubble site, and c) 60 cm concrete wall.*

4.3 Conclusion

In this chapter the focus was on the effects of bandwidth and centre frequency of an UWB radar for trapped-victim detection operations allowing for respiratory motion detection. The factors that have an influence on the choice of bandwidth and centre frequency are the reflective properties of the human body and the attenuation as function of frequency of various obstructing materials, such as walls or rubble. Furthermore, the used antennas have a large influence as well, but due to their dimensions and operational mode their influence is difficult to be removed. The aim of this experimental study is to select the frequency band such that it results in the highest SNR conditions. The study involves assessment on the attenuation of several types of rubble (which are considered challenging to penetrate) as well as the resulting SNR as function of bandwidth and centre frequency when using such rubble types. The results show that the attenuation for sandstone rubble and wall is ca 10-15 dB across the frequency range of interest. Although these values are not very high, it should be clear that realistic rubble thicknesses and types of rubble, which are typically even more challenging, can heavily increase the attenuation and thereby lower the probability of detection.

Analysis of the optimal centre frequency showed that the centre frequency well below 1 GHz (depending on the used antennas) gives rise to the highest SNR values. One should therefore strive to transmit as low frequencies as the antenna type and dimensions allow. This is in particular true for impulse radar, whose spectral power is concentrated in such frequency ranges. It was further shown that even bandwidths of ca. 400 MHz centred at frequencies below 1 GHz are enough for proper detection of respiratory motion and in fact give rise to higher SNR values than larger bandwidths. On the other hand, one should keep in mind the lack of resolving capabilities when using smaller bandwidths, which is an important feature of the radar in the presence of non-stationary clutter or multiple trapped victims.

Finally, it should be mentioned that the experimental study presented herein is performed on selected types of rubble and using specific equipment, which certainly differ from the real-life rubble types. Therefore, the presented results are approximate values and should merely serve as recommendations for future studies or system designs.

5

Human respiratory motion detection

The ultimate aim for a USAR team involved in radar-based trapped-victim detection operations is to obtain knowledge on (in the order of importance) the precise range, number and the medical state of the victims buried under the pile of rubble that is being searched. The conditions that commonly occur in such scenarios can be characterised by low signal-to-noise-and-clutter-ratio (SNCR) conditions, the cause of which has been detailed in the introductory chapter of this thesis. Since the rescue workers rely heavily on radar and dedicated software to assist them in this task, the development and evaluation of an efficient processing method for detection of respiratory motion under realistic conditions is the main aim of this chapter. Due to its impact and importance, it is therefore considered the cornerstone of the complete research performed in the thesis. The first section of this chapter will cover previous work that has been performed by other research groups in this field. In the second section we will explain the developed respiratory motion algorithm in a step-by-step approach. The third section will detail the measurement set-up and the used equipment for the acquisition of data, while the algorithm is tested in the fourth section. The performance of the algorithm for various conditions is put in comparison with an existing algorithm and the conclusion is drawn in the fifth section.

5.1 Previous work in the area of respiratory motion detection

There are two main approaches to respiratory motion detection that have been previously reported in the literature.

The first approach, detailed in a theoretical study conducted by Chernyak from the Moscow Aviation Institute, is based on removing all stationary responses (see section 5.4), summing the energy of each resulting range profile in the slow-time dimension and applying a threshold for automatic target detection [1]. In his study, carrier-based UWB sensing signals with low fractional bandwidth are used, thereby assuming that the respiratory motion response from the victim

exhibits large correlation with the sensing pulse. This assumption does not hold, however, for the case of implementing large fractional bandwidths, as used in our approach. Furthermore, his study disregards the presence of non-stationary clutter and is not complemented with an experimental verification phase.

A recent experimental study by Zaikov et al. [2] focuses on demonstrating the feasibility of UWB-radar-based trapped-victim detection operations under largely realistic conditions. The authors briefly discuss the used RMD algorithm (analogous to the conventional range/Doppler processing method [3]) and show satisfactory results for respiratory motion detection in additive white Gaussian noise (AWGN). The decision space is made up of three dimensions: amplitude, range and slow-time frequency (Chernyak uses only two). However, the authors do not implement any decision threshold during the detection stage nor do they elaborate more in detail on the performance of the RMD algorithm. Most importantly, the authors do not take into account the presence of non-stationary clutter.

5.2 Motivation and aim

The conclusion drawn from past studies on UWB-radar-based trapped-victim detection operations and from our own experience is that it is necessary to develop a post-processing method for respiratory motion detection in the presence of non-stationary clutter responses for low SNCR conditions as well as implementing a threshold for rejection of noise-like responses.

The main motivation of this work is to increase the probability of detection P_d of a trapped victim under a fixed probability of false alarm P_{fa} compared to the reference RMD algorithm used by Zaikov et al. [2]. The comparison is performed both by means of Monte Carlo simulation as well as an experimental study. Since matched filtering is not feasible (see 5.6), the approach is to apply filters and a subspace method in order to suppress the interference, while largely preserving the respiratory motion response energy. The aim is on detection and range estimation of a single trapped victim, but not on the angle-of-arrival estimation. The assumptions that are made on the target are presence of a single, buried, immobile victim resting in horizontal position and having a normal breathing rate.

The proposed RMD algorithm is not dependent on used UWB technology, radar configuration or spectral power levels. It is important to keep in mind that the algorithm is designed to operate under conditions that require some sort of control of the sources on non-stationary clutter such as moving people and machinery operating nearby, otherwise the probability of false alarm P_{fa} becomes unacceptably high.

5.3 Approach

The chosen approach for respiratory motion detection is based on the one used in [2]. Although the RMD algorithm in [2] is not elaborated mathematically, any reader that is familiar with the basic concepts of radar detection will nevertheless easily understand the approach. The algorithm is described in fig. 5.1 and in section 5.7. The approach of the proposed RMD algorithm, however, makes additional steps to combat non-stationary clutter and AWGN, as well as provides a decision threshold that is helpful for the radar operator. The proposed RMD algorithm is divided into three main steps:

1. stationary clutter- and linear-trend suppression,
2. SNCR improvement comprised of three subparts: filtering in range dimension, slow-time frequency-domain windowing and decomposition of non-stationary clutter returns,
3. threshold-based decision- and range estimation stage.

The flow chart showing the individual steps of the developed and the reference RMD algorithm is shown in fig. 5.1.

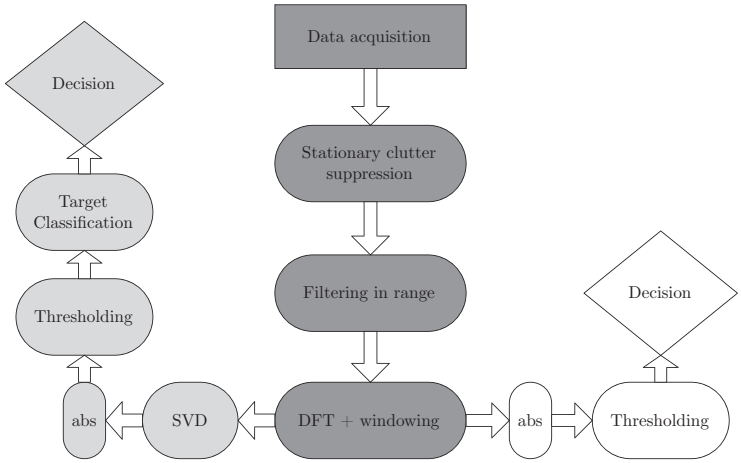

Figure 5.1: *Flow chart detailing the steps in the proposed RMD algorithm (centre and left side) and the reference RMD algorithm (centre and right side)*

5.4 Stationary clutter- and linear-trend suppression

Due to the immobility of the scatterers in the rubble, the resulting clutter is stationary as well and thus manifests itself as a DC component in the slow-

time dimension. However, real-life data acquisition is typically accompanied by instability of the time base (i.e. time drift and jitter caused by imperfections in the triggering unit of a radar device). The amplitude instability results in amplitude fluctuations in the slow-time dimension, but more often, in a linear and gradual change of amplitude with time (linear trend). In order to obtain as high probability of detection as possible, one should strive toward removal of all amplitude instabilities that do not originate from the victim. Amplitude fluctuations act as interference to the process of respiratory motion detection and are treated as non-stationary clutter and is treated in paragraph 5.7. However, linear trend is treated herein, as it is possible to remove its influence during the simultaneous removal of all stationary responses.

There are three types of stationary clutter suppression methods that are considered in this section:

1. range profile subtraction (RPS),

2. mean subtraction (MS) and

3. linear-trend subtraction (LTS).

This section investigates the performance of each method on measured data containing human target responses as well as linear trend originating in data acquisition equipment. The data set that is used for performance assessment is the data set acquired for the "front" position under LOS conditions, see paragraph 3.2.4. The performance assessment criteria are the resulting signal-to-noise-and-clutter ratio (SNCR) and the distribution of the resulting noise and linear trend, respectively.

It should be mentioned that although the stationary clutter suppression methods investigated herein are the most common ones used for the particular application, the number of available methods does not end with three. There exist statistical methods that are typically used for extraction of moving pixels in an otherwise stationary image [4] and [5] as well as methods which implement adaptive filter for background suppression [6] and [7]. However, the choice of stationary clutter suppression methods made by the author reflects their suitability and applicability for further data processing. Furthermore, the chosen methods and the comparison of performance of each method are, in the opinion of the author, highly interesting for any reader familiar with radar-based respiratory motion detection.

5.4.1 Range profile subtraction (RPS) method

The most basic and straightforward stationary clutter suppression approach is to simply subtract each range profile from the previous one, thereby canceling

out all the components that have not changed during the acquisition time t_a:

$$\begin{aligned} \breve{\mathbf{r}}_{k,\mathrm{rps}}[n] &= \mathbf{r}_k[n] - \mathbf{r}_{k-1}[n] \\ &= \breve{\mathbf{h}}_{k,\mathrm{rps}}[n] + \breve{\boldsymbol{\theta}}_{k,\mathrm{rps}}[n] + \mathbf{z}_{k,\mathrm{rps}}[n], \qquad k \in \{2,\ldots,K\} \end{aligned} \quad \boxed{5.1}$$

where $[\,\breve{\cdot}\,]$ denotes the stationary clutter suppression operation and $\mathbf{z}_k[n] = \mathbf{w}_k[n] + \mathbf{w}_{k-1}[n]$. The RPS method serves as a differentiator in the range dimension, thereby acting as a high-pass filter with the impulse response: $h[k] = \delta[k] - \delta[k-1]$, where $\delta[k]$ denotes the unit impulse function (Dirac delta function). The resulting waveform of the respiratory motion response is therefore a first-order derivative of the human target response $\mathbf{h}^*[n]$:

$$\breve{\mathbf{h}}^*_{k,\mathrm{rps}}[n] = \mathbf{h}^{*\,\prime}_k[n], \qquad k \in \{2,\ldots,K\} \quad \boxed{5.2}$$

where $(\cdot)'$ denotes the first-order derivative. Although any externally induced non-stationary clutter and internally induced fast amplitude jumps cannot be fully mitigated at this step (hence the presence of $\breve{\boldsymbol{\theta}}_{k,\mathrm{rps}}[n]$ in eq. 5.1), the slow-changing amplitude instability is typically brought to under the noise floor. If target detection is followed directly after the RPS step, one then obtains a moving target indicator (MTI).

5.4.2 Mean subtraction (MS) method

The best estimate of the stationary responses in the range dimension is obtained by averaging K acquired range profiles in the data matrix $\mathbf{R}[n,k]$. The estimate is then subtracted from each range profile $\mathbf{r}_k[n]$:

$$\begin{aligned} \breve{\mathbf{r}}_{k,\mathrm{ms}}[n] &= \mathbf{r}_k[n] - \frac{1}{K}\sum_{k=1}^{K}\mathbf{R}[n,k] \\ &= \breve{\mathbf{h}}_{k,\mathrm{ms}}[n] + \breve{\boldsymbol{\theta}}_{k,\mathrm{ms}}[n] + \mathbf{w}_k[n], \qquad k \in \{1,\ldots,K\} \end{aligned} \quad \boxed{5.3}$$

The mathematical expression of the respiratory motion response $\breve{\mathbf{h}}^*_{k,\mathrm{ms}}[n]$ can be obtained by considering the following:

$$\breve{\mathbf{h}}^*_{k,\mathrm{ms}}[n] = \mathbf{h}^*_k[n] - \mathbf{h}^*_k[n - \mu_{n^*}] \quad \boxed{5.4}$$

where $\mu_{n^*} = \mathrm{E}\{\Delta n^*\}$. Expanding, by means of Taylor expansion, the second term in the right-hand side of eq. (5.4) in any point n one obtains:

$$\begin{aligned} \mathbf{h}_k^*[n-\mu_{n^*}] &= \mathbf{h}_k^*[n] - \mu_{n^*}\cdot \mathbf{h}_k^{*\,\prime}[n] + \frac{(\mu_{n^*})^2}{2!}\cdot \mathbf{h}_k^{*\,\prime\prime}[n] - \\ &- \frac{(\mu_{n^*})^3}{3!}\cdot \mathbf{h}_k^{*\,\prime\prime\prime}[n] + \ldots + \sum_{p=0}^{\infty}\frac{(-\mu_{n^*})^p}{p!}\cdot \mathbf{h}_k^{*\,(p)}[n] \\ &\Longrightarrow \\ \mathbf{h}_k^*[n] - \mathbf{h}_k^*[n-\mu_{n^*}] &= \sum_{p=1}^{\infty}(-1)^{(p+1)}\frac{(\mu_{n^*})^p}{p!}\cdot \mathbf{h}_k^{*\,(p)}[n] \end{aligned} \qquad (5.5)$$

where $(\cdot)^{(p)}$ and $p!$ denote the p-th order derivative and factorial, respectively. Therefore:

$$\breve{\mathbf{h}}_{k,\mathrm{ms}}^*[n] = \sum_{p=1}^{\infty}(-1)^{(p+1)}\frac{|\mu_h|^p}{p!}\cdot \mathbf{h}_k^{*\,(p)}[n] \qquad (5.6)$$

5.4.3 Linear-trend subtraction (LTS) method

The LTS method is based on estimating the DC component and any potential linear trend in the slow-time dimension in the data matrix $\mathbf{R}[n,k]$ by means of a linear least-squares fit. The estimate is subsequently subtracted from $\mathbf{R}[n,k]$, resulting in:

$$\breve{\mathbf{R}}^T = \mathbf{R}^T - \mathbf{x}(\mathbf{x}^T\mathbf{x})^{-1}\mathbf{x}^T\cdot\mathbf{R}^T \qquad (5.7)$$

where $\mathbf{x} = \left[\frac{\mathbf{k}}{K}\ \mathbf{1}_K\right]$, $\mathbf{k} = [0,\ldots,K-1]^T$ and $\mathbf{1}_K$ is a $K\times 1$ vector containing unit values. The obtained waveform of $\breve{\mathbf{h}}_{k,\mathrm{lts}}^*[n]$ is the same as $\breve{\mathbf{h}}_{k,\mathrm{ms}}^*[n]$, with the addition of the factor $\boldsymbol{\Psi}[k,K]_n$ which denotes a compensation term for the linear trend in the slow-time dimension:

$$\breve{\mathbf{h}}_{k,\mathrm{lts}}^*[n] = \breve{\mathbf{h}}_{k,\mathrm{ms}}^*[n] + \boldsymbol{\Psi}[k,K,\boldsymbol{\delta}_k,\boldsymbol{\theta}_k], \qquad k\in\{1,\ldots,K\} \qquad (5.8)$$

5.4.4 Performance comparison of the stationary clutter suppression methods

The only advantage of the RPS method over the two other methods is that the amplitude instability- and/or non-stationary clutter responses are present only at the range at which they occur and do not have any effects on the remaining ranges. This is not the case, however, with the other two methods. In the most common case in which the non-stationary responses are not zero-mean in the slow-time dimension, the resulting linear trend after the use of the linear-trend subtraction method will either be increasing or decreasing with time. Subtracting the linear trend estimate will preserve the sloping and will thereby influence the whole matrix $\breve{\mathbf{R}}[n,k]$.

In the case of the MS method, as well as the LTS method, the shape and the extent of the amplitude fluctuations and the non-stationary clutter responses are preserved. However, since the decision on the presence of the respiratory motion response is done in the slow-time frequency domain (for more details, see sections 5.6 and 5.7), the performance of each method, therefore, needs to be assessed in that domain.

The RPS method has three major disadvantages compared to the LTS- and MS method:

- the variance of the AWGN is doubled, since

$$\sigma_z^2 = \sigma_{w_1}^2 + \sigma_{w_2}^2 = 2 \cdot \sigma_{w_1}^2 = 2 \cdot \sigma_{w_2}^2 \tag{5.9}$$

- the magnitude of $\breve{\mathbf{h}}^*[n]$, and thereby the SNR, is reduced. The effect can be seen in fig. 5.2(a), in which the slow-time vector before the stationary clutter suppression $\mathbf{r}_n[k]$ containing $\mathbf{h}_n^*[k]$ and the resulting slow-time, respiratory motion vectors $\mathbf{h}_{n,\text{lts}}^*[k]$ and $\mathbf{h}_{n,\text{rps}}^*[k]$ are compared. It is clearly seen from fig. 5.2(a) that:

$$\sigma_{h,\text{rps}}^2 < \sigma_{h,\text{lts}}^2 \tag{5.10}$$

  It can further be clearly observed that the LTS method does not affect the magnitude of $\mathbf{h}_n^*[k]$. The average energy ratio E_{lr} of the resulting respiratory motion responses after the LTS and RPS method:

$$E_{lr} = \frac{\mathrm{E}\left\{\breve{\mathbf{h}}_{k,\text{lts}}^{*\,2}[n]\right\}}{\mathrm{E}\left\{\breve{\mathbf{h}}_{k,\text{rps}}^{*\,2}[n]\right\}} = 11 \text{ dB} \tag{5.11}$$

- The use of the RPS method results in the occurrence of much stronger harmonic components of the respiratory motion responses compared to the LTS method (as well as the MS method), as seen from fig. 5.2(b). The figure shows the resulting respiratory motion responses in the slow-time domain, where the two responses are brought to the same peak amplitude for easier comparison.

- using the RPS method, the power spectral density of the resulting AWGN in the slow-time, frequency domain is not flat, but increases with frequency. This occurs due to the fact that the RPS method serves as a differentiator in time domain, thereby acting as a high-pass filter with the transfer function $H(z)$:

$$H[z] = \mathcal{Z}\left\{h[k]\right\} = 1 - z^{-1} = \frac{z-1}{z}, \qquad z \neq 0 \tag{5.12}$$

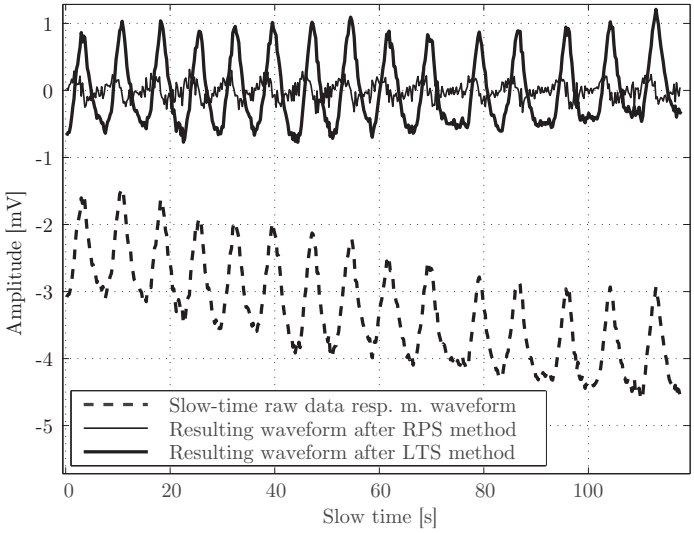

(a)

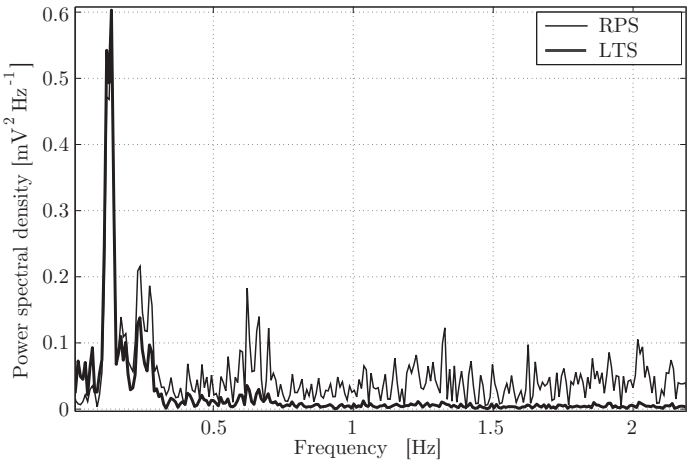

(b)

Figure 5.2: *The result of two stationary clutter suppression methods (range profile subtraction and linear-trend subtraction) in: a) slow-time domain and b) slow-time, frequency domain. Note the lower SNR and stronger harmonics resulting from the RPS method.*

where $\mathcal{Z}\{\cdot\}$ denotes the z-transform operation, $z = \exp\{i2\pi k/K\}$ and $i = \sqrt{-1}$. The PSD of the AWGN increases non-linearly with frequency

and reaches its maximum for $f = f_a/2$. The flatness of the AWGN in the decision space is imperative, as will become obvious later in the chapter.

The difference in performance between the MS and the LTS is not large, although a few major differences are obvious. The MS preserves the linear trend in the slow-time dimension that was present in the raw data set, thereby obtaining a ramp waveform. Applying FFT in the presence of a ramp, causes the

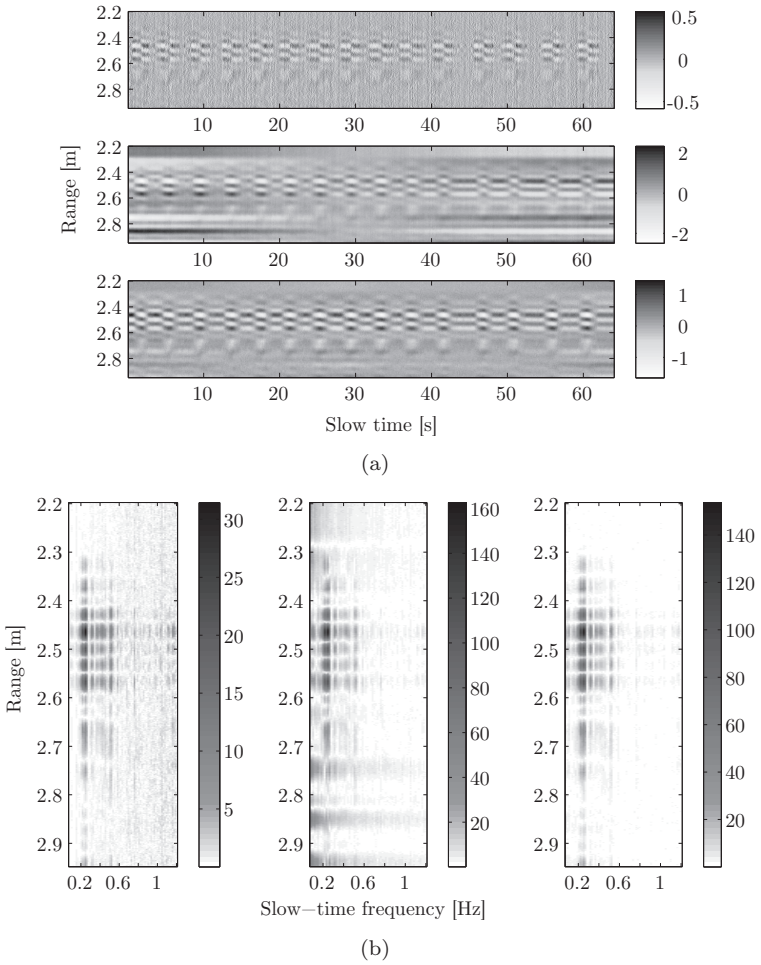

Figure 5.3: *The resulting respiratory motion responses in a) time domain and b) slow-time frequency domain after application of the three investigated clutter suppression methods. Note the presence of energy leakage originating at lower frequency range after the use of the MS method and the absence of the same for the other two methods.*

occurrence of parasitic responses in the spectrum originating at DC (commonly referred to as leakage), see second subfigure in fig. 5.3(b). The leakage risks to mask the weak respiratory motion responses and thereby cause missed detection. Using the LTS method, however, the leakage is heavily suppressed, since the LTS removes the linear trend.

Using the acquired data set, the difference in the obtained SNCR values after the application of the LTS and the RPS method (assessed in the frequency domain) is $\Delta SNCR_{lr} = 2.9$ dB and the LTS and the MS method $\Delta SNCR_{lm} = 2.7$ dB. The reason for the relatively poor performance of the MS method in terms of SNCR is attributed to the presence of parasitic responses due to amplitude instability. In the absence of it, the SNCR difference is expected to be nil or near nil.

The conclusion that is drawn from this study is that the range profile subtraction method should be avoided for the purposes of stationary clutter suppression in UWB-radar-based trapped-victim detection operations. Although it effectively suppresses amplitude instabilities in the slow-time dimension, it causes loss in signal energy, doubles the noise variance, causes non-linear noise floor in the slow-time dimension, as well as increases the magnitude of the higher-order harmonics. The most useful method is the linear-trend subtraction method, both in terms of preserving the SNR and suppressing linear amplitude instability. It outperforms the RPS and performs significantly better than the MS method in the presence of linear amplitude instability.

5.5 Filtering in range dimension

In case of a scenario where the respiratory motion response $\breve{\mathbf{h}}^*[n]$ is masked only by AWGN, such as (ideally) in our case after stationary clutter removal, the most straightforward way to improve SNR is to perform correlation of a template $\mathbf{g}[n] = \breve{\mathbf{h}}^*[-n]$ (i.e. reciprocal of $\breve{\mathbf{h}}^*[n]$) with $\breve{\mathbf{r}}_k$. However, in real life scenarios, $\breve{\mathbf{h}}^*[n]$ differs significantly from the radiated waveform. The reason is twofold: a) the waveform of $\breve{\mathbf{h}}^*[n]$ is frequency-, aspect angle- and body-position-dependent (see paragraph 3.3.4) and b) the transfer function of the obstacles in the scene is not a deterministic function in itself, and depends on a wide range of parameters, such as relative permittivity, metal content and dampness of the rubble material, antenna-pair polarisation etc. The proposed approach for further SNCR improvement is application of a finite impulse response (FIR) filter on each $\breve{\mathbf{r}}_k[n]$ in the range dimension, resulting in $\tilde{\mathbf{r}}_k[n]$, where $[\,\tilde{\cdot}\,]$ denotes the filtering operation. The filtering is performed in particular due to the presence of substantial high-frequency noise, which is a result of heavy oversampling of the backscattered waveforms. An example of the effect of linear filtering in range dimension can be seen in fig. 5.4(c).

5.6 Slow-time frequency-domain windowing

An additional way of improving SNCR is to make use of the fact that the respiratory motion has a periodical behaviour and that its frequency is confined within a narrow frequency window, as seen in paragraph 3.2.4. The approach is to window out components in the spectrum of $\tilde{\mathbf{r}}_n[k]$, i.e. in the slow-time dimension, that are not expected to contain the fundamental human respiratory frequency f_h and possibly the first harmonic component. A K_m-sized rectangular window $\boldsymbol{\nu}[\kappa]$ is applied in the frequency domain on each slow-time vector:

$$\mathbf{r}_n^{fd}[\kappa] = \boldsymbol{\nu}[\kappa] \odot \{\mathrm{DFT}\,\{\tilde{\mathbf{r}}_n[k]\}\}, \qquad \begin{matrix} \kappa & \in \mathcal{K}^*; \\ \mathcal{K}^* & = \{\kappa^*, \kappa^*+1, \ldots, \kappa^*+K_m-1\} \end{matrix} \tag{5.13}$$

where $[\cdot]^{fd}$ represents the windowing operation in the frequency domain; $\mathrm{DFT}\,\{\tilde{\mathbf{r}}_n[k]\}$ is the Discrete Fourier Transform (DFT) of $\tilde{\mathbf{r}}_n[k]$; index κ^* is a fixed, lowest value of the index κ contained within $\boldsymbol{\nu}[\kappa]$. The rectangular window $\boldsymbol{\nu}[\kappa]$ is set so that $\kappa_{\bar{f}_h} \in \mathcal{K}^*$, where $\bar{f}_h = \mathrm{E}\,\{f_h\}$ and $\mathrm{E}\,\{\cdot\}$ denotes the expected value operation. $\bar{f}_h$ is from obvious reasons not fully known a-priori, although a qualified estimate can be made based on previous observations. $K_m < K/2$ is an empirically derived value which is directly proportional to the probability of including $\bar{f}_h$ and inversely proportional to the SNCR gain. An example of $\left|\mathbf{R}^{fd}\right|$, where $\mathbf{R}^{fd} = \left[\mathbf{r}_1^{fd}[\kappa], \mathbf{r}_2^{fd}[\kappa], \ldots, \mathbf{r}_n^{fd}[\kappa]\right]^T$, $\kappa \in \mathcal{K}^*$, can be seen in fig. 5.4(d).

5.7 Non-stationary clutter suppression

Zaikov et al. base the decision on the presence of a response from a breathing victim by visual inspection of $\left|\mathbf{R}^{fd}\right|$. For reasonably high SNR conditions and absence of any non-stationary clutter responses, there is a clearly visible contrast between the response from a breathing victim and the noise, which allows for estimation of the range of the victim. However, it has been observed during field trials that part of the energy of $\boldsymbol{\theta}_n^{fd}[\kappa]$ is likely to appear in $\mathbf{R}^{fd}$ along with the respiratory motion response $\mathbf{h}_n^{*fd}[\kappa]$, thereby reducing the probability of detection. The aim of this final stage of the algorithm is to reduce noise, but most importantly, fragments of $\boldsymbol{\theta}_n^{fd}[\kappa]$ which were not removed during the previous stages, while striving to minimally affect the energy of $\mathbf{h}_n^{*fd}[\kappa]$. The approach is to decompose $\mathbf{R}^{fd}$ into a set of orthonormal matrices by means of the Singular Value Decomposition (SVD):

$$\mathbf{R}^{fd} = \mathbf{U} \cdot \boldsymbol{\Lambda} \cdot \mathbf{V}^H \tag{5.14}$$

where $[\cdot]^H$ denotes the complex conjugate transpose operation. The hanger matrix $\mathbf{U} = [\mathbf{u}_1, \mathbf{u}_2, \ldots, \mathbf{u}_{K_m}]$, $\mathbf{U} \in \mathbb{C}^{K_m \times K_m}$ is a unitary matrix. The columns

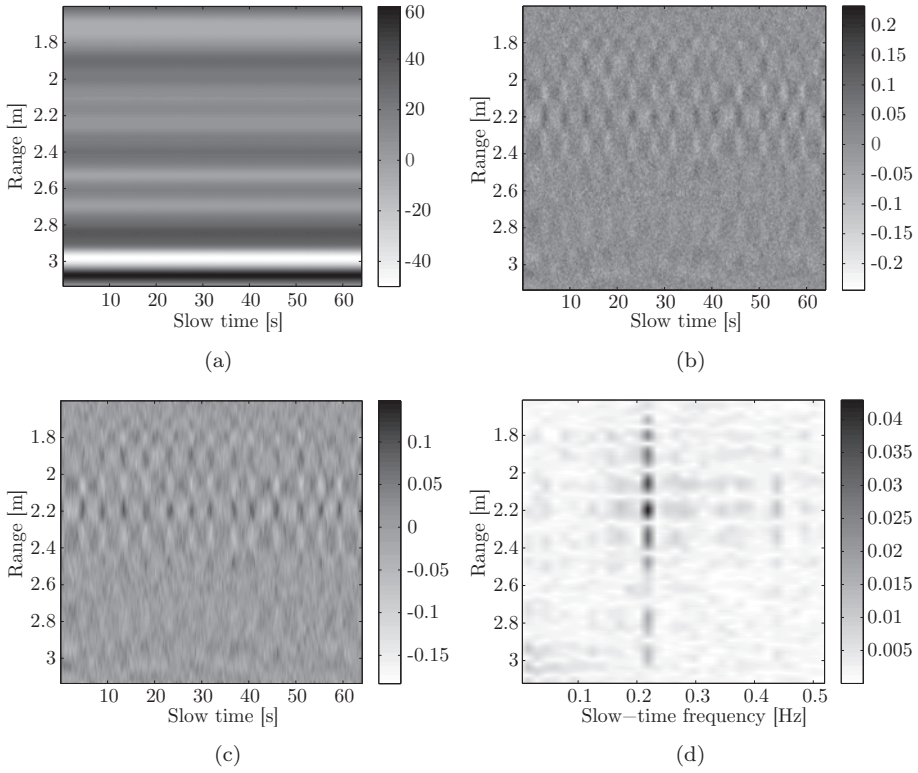

Figure 5.4: *Four stages in the processing scheme: a) The raw unprocessed dataset* $\mathbf{R}[n,k]$*; only strong stationary clutter visible; b)* $\breve{\mathbf{R}}[n,k]$*; respiratory motion barely discernible; noise dominates the image; c)* $\tilde{\mathbf{R}}[n,k]$*; respiratory motion more discernible due to suppression of noise; d)* $\left|\mathbf{R}^{fd}[n,\kappa]\right|$*; respiratory motion response is clearly visible.*

of $\mathbf{U}$ are called the left singular vectors, $\mathbf{u}_k \in \mathbb{C}^{K_m}$, and form an orthonormal basis for the slow-time vectors, meaning that $\mathbf{u}_i \cdot \mathbf{u}_j = 1$ for $i = j$, and $\mathbf{u}_i \cdot \mathbf{u}_j = 0$ otherwise. The aligner matrix $\mathbf{V} = [\mathbf{v}_1, \mathbf{v}_2, \ldots, \mathbf{v}_N]$, $\mathbf{V} \in \mathbb{C}^{N \times N}$ is unitary as well. The rows of $\mathbf{V}^H$ contain the elements of the right singular vectors, $\mathbf{v}_n$, and form an orthonormal basis for the range profiles. The stretcher matrix $\mathbf{\Lambda} \in \mathbb{R}^{K_m \times N}$ contains only diagonal, non-zero values (singular values), $\lambda_j \in \{\lambda_1 < \lambda_2 < \ldots < \lambda_{K_m}\}$, where $j \in \{1, \ldots, K_m\}$. Since there are K_m degrees of freedom in $\mathbf{R}^{fd}$, rank $\left\{\mathbf{R}^{fd}\right\} = K_m$. Assuming the presence of $\mathbf{h}^{*fd}$ in $\mathbf{R}^{fd}$, the majority of the energy of $\mathbf{h}^{*fd}$, as has been observed in experimental data, will be contained within one singular matrix,

$$\mathbf{D}_j = \lambda_j \cdot \mathbf{u}_j \cdot \mathbf{v}_j^H, \quad \mathbf{D}_j \in \mathbb{C}^{K_m \times N}, \; j = \{1, \ldots, K_m\} \tag{5.15}$$

and thus the rank of the useful signal subspace equals 1. This is explained by the fact that the slow-time behaviour of $\mathbf{h}_k^*[n]$ can be modeled as an amplitude-modulated sinusoid, since only the fundamental frequency component is the dominant one. Given the fact that an amplitude-modulated sinusoid can be stretched by a single basis function and that the waveform of $\mathbf{h}_k^*[n]$ does not change significantly during the observation time, the rank of the signal subspace therefore equals 1. The subsequent singular images that could potentially contain fractions of the energy of $\mathbf{h}_n^{*fd}[\kappa]$ are considered to experience too low SNR conditions for reliable detection and are thereby not useful.

5.7.1 Threshold-based detection and classification

This stage consists of two sub-stages: 1) provide indication whether any part of the data passes a threshold and in which singular matrix, 2) perform target classification and estimate the range of the victim.

Threshold implementation

Assuming the presence of a breathing victim, the index $j = j^*$ belonging to the singular matrix $\mathbf{D}_{j^*}$ is unknown a-priori and depends much on the magnitude and the amount of the remaining non-stationary clutter $\boldsymbol{\theta}_k^{fd}[\kappa]$, as well as the overall SNCR. The chosen approach to determine j^* is to consider only $J < K_m$ first singular matrices as decision spaces, where the integer J is empirically derived. Singular matrices corresponding to higher values are unsuitable for detection, since in the case of the fractions of the respiratory motion response contained in any of such matrices, its magnitude becomes comparable to the unwanted responses that fall into the same singular matrix (due to too low SNCR values). In order to discard the singular matrices that contain only noise and, in doing so, focusing the attention of the radar operator to the singular matrices that can potentially contain the respiratory motion response, a constant false

alarm rate (CFAR) threshold is applied on each decision matrix according to:

$$\gamma_{j^\dagger} = -\lambda_{j^\dagger} \cdot \frac{2 \cdot \log(P_{fa}/J)}{\pi \cdot \sqrt{N \cdot K_m}} \quad j^\dagger \in \{1, \ldots, J\} \tag{5.16}$$

For proof of eq. 5.16, see B. Hypothesis testing on whether potentially a victim is present or not is performed on decision matrices $\mathbf{D}_{j^\dagger}$:

$$\underset{j^\dagger=1,\ldots,J}{\arg} \mathbf{D}_{j^\dagger} \underset{H_0}{\overset{H_1}{\gtrless}} \gamma_{j^\dagger}$$

where H_0 denotes the null hypothesis (no victim present) and H_1 denotes the alternative hypothesis (a victim potentially present).

Target classification and range estimation

The only feasible and efficient method for determining whether there is a respiratory motion response present among all responses in the singular matrices that have passed the threshold is simply by visual inspection. In order to minimize falsely classified non-stationary clutter responses as respiratory motion responses, the operator needs to complement the visual image of the suspected respiratory motion response with $\left|\mathbf{R}^{fd}\right|$. Once the singular image containing the respiratory motion response has been identified, its range bin index n^* is determined according to:

$$n^* = \underset{n \in \mathcal{N}}{\arg\max} \left\{ \left| \mathbf{D}_{j^*}[n, \underset{\kappa \in \mathcal{K}}{\arg\max} \{|\mathbf{D}_{j^*}[n, \kappa]|\}] \right| \right\} \tag{5.17}$$

Finally, the range of the victim r^* is estimated according to:

$$r^* = \frac{n^* \cdot t_s \cdot c_0}{2 \cdot \sqrt{\tilde{\epsilon}_r}} \tag{5.18}$$

where $\tilde{\epsilon}_r$ is the estimate of the relative permittivity of the obstructing medium (rubble).

5.8 Experimental data acquisition

The aim of the experimental data acquisition was to obtain data that would serve as a platform for performance comparison between the developed and the reference RMD algorithms. A further aim was to acquire data in such a way that it models real-life-like scenarios as close as possible. This involves large attenuation of construction material and presence of moving objects in the vicinity of the scene of interest. The data acquisition involved an motionless human being resting in a concrete pipe placed under a pile of bricks.

5.8.1 Measurement set-up, scenarios and equipment

The data acquisition was performed at a building material dump. The dump site is located some 5 km from the main international airport in Sweden, outside Stockholm. The proximity to the airport radar and its communication facilities, as well the dump site being within the landing corridor of incoming aircraft, resulted in high exposure to narrowband interference from the airport and the incoming aircraft. Furthermore, there was a presence of loaders and heavy trucks operating in the vicinity. The rubble was artificially created by placing a ca. 1.2 m pile of standard-sized bricks mixed with moist soil on top of a previously unused sewer pipe made up of reinforced concrete and having 80 cm inner diameter and 10 cm wall thickness.

In paragraph 4.1.1 it has been found that a reinforced concrete sewer pipe is not a suitable object to use for placement of a test person due to too high attenuation. However, this fact is not relevant for this measurement since one of the aims of the experimental verification in this chapter to is to create low SNR conditions and not, for instance, to investigate the largest realistic thickness of rubble under which a motionless person can be detected using an UWB radar.

(a) (b)

Figure 5.5: *Measurement set-up during the experimental verification; a) two large-sized antennas were placed on top of a pile of bricks and a concrete pipe; b) test person lying inside the concrete pipe.*

Measurement equipment consisted of a Meodat 4.5 GHz M-sequence Evaluation Kit (see A.2). Two identical double-ridged horn antennas (see A.4.3), one used as transmit and the other as receive antenna, were placed on top of the brick pile, separated 3 m between their respective centres and each tilted ca. 10° towards each other, see fig. 5.5(a). There was a slight offset (ca. 40 cm) of one of the antennas from the central axis of the pipe, as can be seen in fig. 5.5(a), thereby lowering somewhat the SNR conditions. The height of the brick pile measured from the ground level up to the antennas was ca. 1.6 m. A female test person was resting on the back inside the sewer pipe with the chest placed roughly midway between the antennas, see fig. 5.5(b). The test person was breathing in a relaxed manner and not moving otherwise. Non-stationary clutter was caused by a large loader operating close-by.

5.9 Results

The evaluation of the performance of the proposed detection algorithm is threefold. The first performance measure, presented in paragraph 5.9.1, is evaluation of the probability of detection P_d as function of input SNR for constant probability of false alarm P_{fa}, obtained by means of a Monte Carlo simulation. The assessment of the detection performance of the developed RMD algorithm is put in relation to the performance of the reference RMD algorithm applied on the same dataset. The second performance measure, presented in paragraph 5.9.2, is comprised of comparing the amount of SNR improvement as function of input SNR of the proposed RMD algorithm with that of the reference RMD algorithm. The last performance measure, presented in paragraph 5.9.3, illustrates the non-stationary-clutter separation capabilities of the proposed RMD algorithm compared to the reference RMD algorithm using experimental data.

5.9.1 Detection performance in clutter-free environment

The increase in visual contrast (or SNR in this case), and thereby the probability of detection, is proportional to the observation time $T_{obs} = K \cdot T_a$. Fig. 5.6 shows the visual contrast after applying the developed RMD algorithm on the dataset consisting of measured $\mathbf{h}^*[n]$ and generated AWGN. The reason for the periodic variations in the contrast values is due to the periodicity of the respiratory motion. The dashed curve shows the non-linear trend as function of T_{obs}, following a logarithmic increase in contrast. The conclusion is that there is both a theoretical limit (an asymptotic value for high T_{obs}), but also a practical limit to the gain in visual contrast as function of observation time, namely increasing the likelihood of the presence of non-stationary clutter as well as computational time (shown on the upper x-axis). An advantage of the developed RMD is that it is not heavily computationally demanding, since even the processing of a large number of samples by a standard dual-core processor

for the case of $T_{obs} = 10$ min, the computational time is still only 1.78 s, as seen from fig. 5.6.

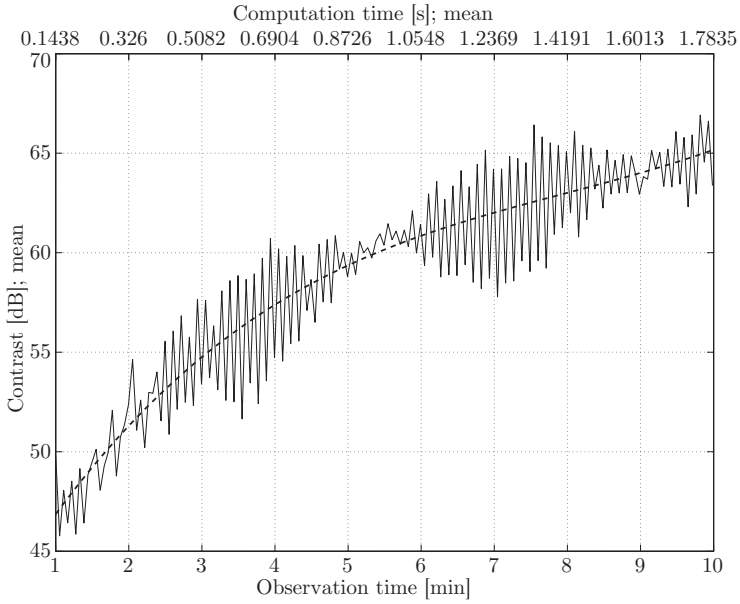

Figure 5.6: *Average contrast values as function of observation time (lower x-axis) and computational time (upper x-axis) - blue curve; trend - red curve*

The probability of detection P_d as function of input SNR for probability of false alarm $P_{fa} = 10^{-2}$ and $P_{fa} = 10^{-3}$, using the developed and reference RMD algorithm respectively, can be seen in fig. 5.7. The performance is evaluated by means of Monte Carlo simulations, assuming perfect knowledge of the breathing frequency as well as the range bin index n^*. The simulation parameters are detailed in Table 5.1. The respiratory motion response waveform as function of time has been acquired by means of measurements in high SNR conditions. The generated noise is AWGN, thus there is no presence of non-stationary clutter. The input SNR values are computed according to the following expression:

$$\mathrm{SNR}_{in} = 20 \cdot \log_{10} \left(\frac{\frac{1}{K} \sum_{k=1}^{K} \max_{n} \left| \tilde{\mathbf{h}}^*[n,k] \right|}{\bar{\sigma}_w} \right) \quad (dB) \qquad 5.19$$

where $\bar{\sigma}_w$ denotes the average standard deviation of the AWGN values. The respiratory motion response and the noise occupy the same bandwidth. During the detection stage, the alternative hypothesis H_1 was assumed only in the case of two range bins adjacent to n^* or more passing the threshold. This criterion is seen as a minimal one for distinguishing a respiratory motion response from

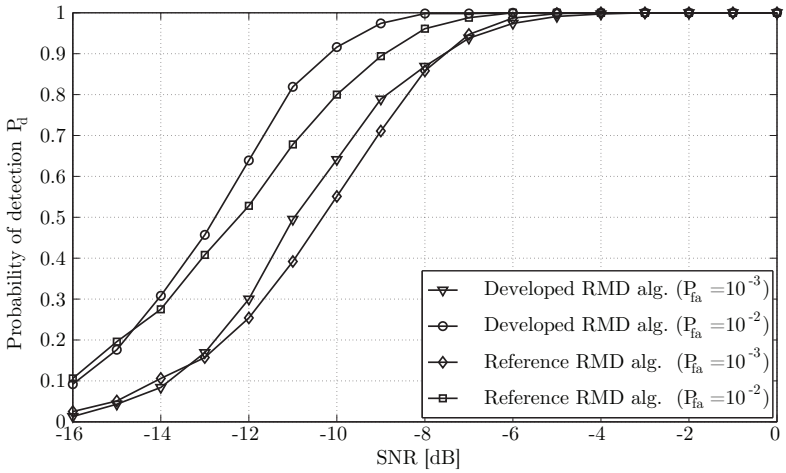

Figure 5.7: *Probability of detection as function of input SNR for $P_{fa} = 10^{-2}$ and $P_{fa} = 10^{-3}$ for the developed and the reference RMD algorithm.*

noise and thus this performance measure can be seen as the upper bound on the detection performance in AWGN for the respective RMD algorithm. As seen in fig. 5.7, the developed RMD algorithm performs slightly better than the reference RMD algorithm. For $P_{fa} = 10^{-2}$ the developed RMD algorithm exhibits $P_d = 0.8$ at -11.1 dB, whereas the reference RMD algorithm exhibits $P_d = 0.8$ at -10.0 dB, which is an improvement of 1.1 dB. For $P_{fa} = 10^{-3}$, the difference is even smaller (0.48 dB). These results suggest that the developed RMD algorithm is not significantly more efficient in clutter-free scenarios. Thus, its main strength does not lie in its application to clutter-free conditions, but in scenarios with overlapping non-stationary clutter, as shown by subsequent results.

5.9.2 SNCR-improving capabilities of the developed RMD algorithm

The ability of the algorithm to improve the SNCR conditions, or the visual contrast between the respiratory motion response and the interference (noise + non-stationary clutter), is demonstrated in this paragraph. Three distinct datasets were acquired at the same test site without any test person present in the concrete pipe. Non-stationary clutter, which is induced by a loader that was operating near-by, is present in all three datasets and its responses in each dataset are distinct. The respiratory motion response as function of time (the same as used in the previous paragraph) is added to each dataset. Its magnitude is varied in such a way that it corresponds to a range of input SNCR values.

Table 5.1: *Monte Carlo simulation and measurement parameters*

Parameter	**Value**
N	200
K	1024
T_{obs}	106 s
L	16
Nr. of datasets	20 for each dB value
J	3
Filter coefficients	**Value**
Lower -3dB cut-off frequency ω_{lo}	0.1 rad/s
Higher -3dB cut-off frequency ω_{hi}	0.35 rad/s
Filter length	66
f_{κ^*}	0.11 Hz
$f_{\kappa^*+K_m-1}$	0.24 Hz

The input SNCR values are computed in the same manner as in eq. 5.19. However, due to the presence of non-stationary clutter, the notion $\bar{\sigma}_w$ incorporates this time the values of all measured interference. The non-stationary clutter responses, which are not spread evenly across the decision matrix, mask the respective respiratory motion responses, making detection with this method very difficult, despite high output SNCR values. The result is high overall SNCR values, but low SNCR values in and around the respiratory motion response. The developed and the reference RMD algorithm are applied on each of the three datasets and for each individual input SNCR value, respectively. In the detection stage of the developed RMD algorithm, by careful analysis of each considered singular matrix (the value J was set to 4), it was made sure that the respiratory motion response was correctly identified instead of the non-stationary clutter response. The visual contrast-increasing (or SNCR improvement) capability of the developed RMD algorithm in relation to the reference RMD algorithm is shown in fig. 5.8.

The most important result that immediately becomes obvious by observing fig. 5.8 is that the developed RMD algorithm consistently achieves higher contrast values for each dataset. This is seen in particular for lower input SNCR values where the applicability of the developed RMD algorithm is highest. This performance measure shows that during the visual classification of the processed data, the probability of detection for a fixed P_{fa} is higher for the developed RMD algorithm. An interesting feature of the developed RMD algorithm manifests itself in dips in the contrast values. The dips originate from the fact that the energy of the respiratory motion response for certain input SNCR values becomes divided between two neighbouring singular matrices. The difference in behaviour of the contrast curve across the input SNCR among the three datasets

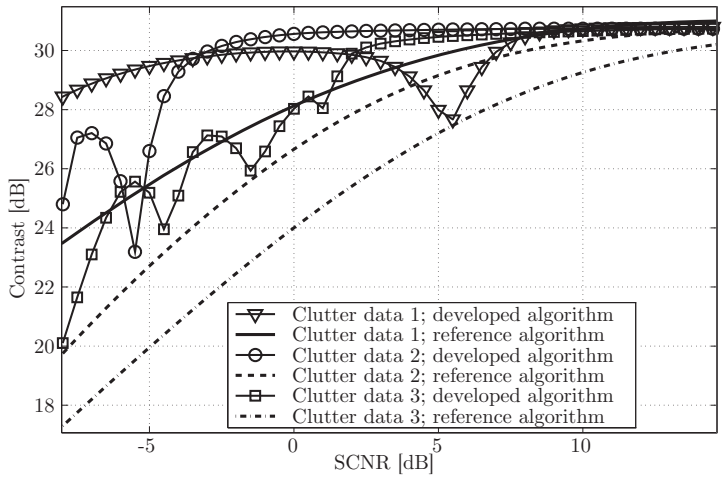

Figure 5.8: *Output SCNR as function of input SCNR for the developed and the reference RMD algorithm*

is attributed to the difference in the amount of presence and nature of measured non-stationary clutter responses. As the input SNCR values are increased and the respiratory motion response is found in the first singular matrix, a plateau is reached in the contrast curve. It is thereby obvious that there is little added value of using the developed RMD algorithm over the reference RMD algorithm for high input SNCR values. However, it should be noted that the input SNCR conditions during the detection of a breathing victim are typically quite low and precisely in the SNCR range in which the developed RMD algorithm performs better than the reference RMD algorithm in terms of increasing contrast.

5.9.3 Clutter separation capabilities of the developed respiratory motion detection algorithm using experimental data

The aim of this paragraph is to demonstrate the added value of implementing the developed RMD algorithm over the reference one in conditions where non-stationary clutter is overlapping with the respiratory motion response. This is shown for two cases, one where the non-stationary clutter is induced by the operating loader and the second one where it is induced by amplitude instability in the data acquisition equipment.

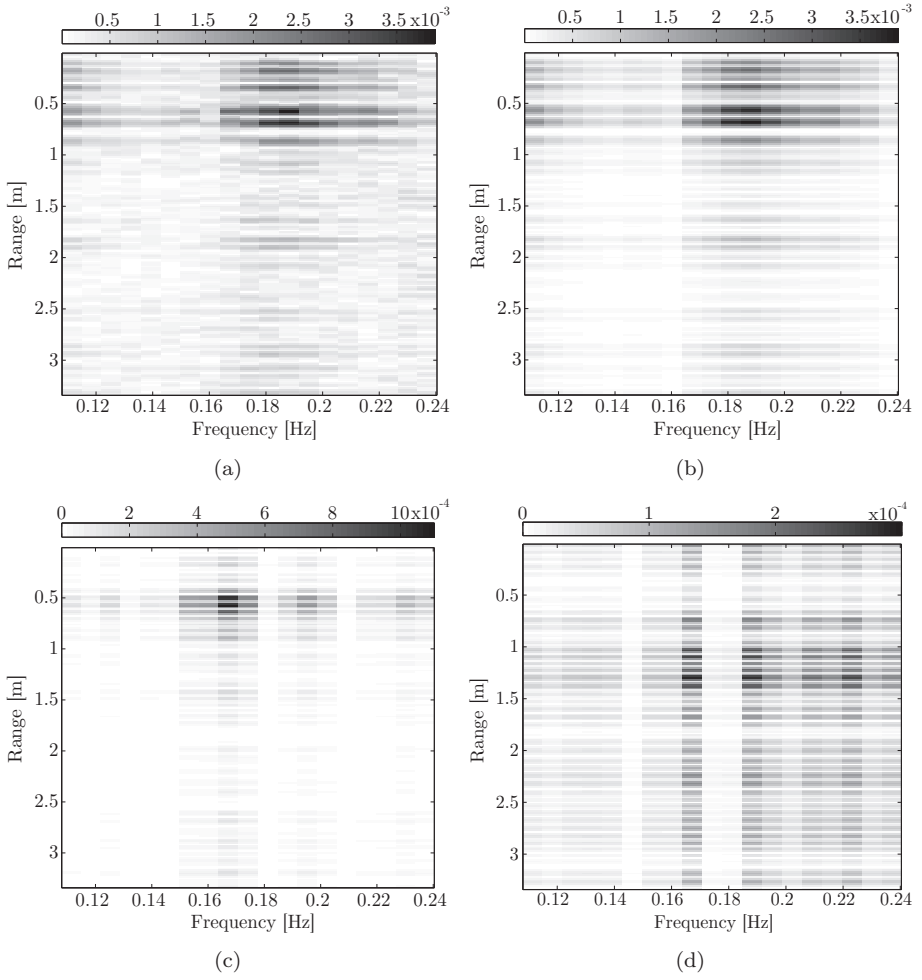

Figure 5.9: *Decision matrices for the case study I: a) reference RMD algorithm,* $\left|\breve{\mathbf{R}}^{fd}\right|$ *- respiratory motion response not discernible; b)* $|\boldsymbol{D}_1|$ *- non-stationary clutter and noise present only; c)* $|\boldsymbol{D}_3|$ *- respiratory motion response clearly discernible; d)* $|\boldsymbol{D}_4|$ *- non-stationary clutter and noise present only.*

Case study I

For the first case study, two datasets were acquired separately, one with high SNCR conditions and the other containing only non-stationary clutter. The measurement parameters have been specified in table 5.1. The unprocessed

datasets were added together, thereby forming the dataset on which the developed and the reference RMD algorithm, respectively, were applied on. The motivation for this approach is threefold: *i*) it is necessary to have complete and fully certain knowledge on the range and breathing frequency of the test person, *ii*) there were no fully appropriate candidates found among the acquired datasets such that non-stationary clutter and the respiratory motion response are overlapping, and *iii*) the addition of two unprocessed data is a fully justifiable operation from physics point of view.

Fig. 5.9(a) shows $\left|\breve{\mathbf{R}}^{fd}\right|$, i.e. the resulting image after post-processing using the reference RMD algorithm. Due to the presence of strong non-stationary clutter, the visible responses in $\left|\breve{\mathbf{R}}^{fd}\right|$ are spread in both range and frequency, thus suggesting to the radar operator than only non-stationary clutter responses are present. The actual fact is that the non-stationary clutter responses are masking the respiratory motion response. The decision that would be made by the radar operator in this case would therefore result in a missed detection. However, the result of the application of the developed RMD algorithm is that a clear respiratory motion response at range 0.5 - 0.7 m (c_0 assumed) and breathing frequency 0.17 Hz is visible in fig. 5.9(c). Three out of four considered singular matrices passed their respective thresholds (the value of the thresholds being $\gamma_1 = 3.0 \cdot 10^{-3}$, $\gamma_2 = 7.7 \cdot 10^{-4}$, $\gamma_3 = 4.3 \cdot 10^{-4}$ and $\gamma_4 = 2.7 \cdot 10^{-4}$, for $P_{fa} = 10^{-2}$). The respiratory motion response is located in the third decision matrix $|\mathbf{D}_3|$. The first and the fourth decision matrices, which passed their respective thresholds (in the fourth one only a few values are larger than the threshold), are depicted in fig. 5.9(b) and fig. 5.9(d), respectively. It is fairly obvious from the spread of the responses in the two figures that they belong to that of the non-stationary clutter.

Case study II

In the second case study, the developed RMD algorithm is applied on a dataset which experiences large and sudden amplitude variations in slow-time dimension, see fig. 5.10.

Although the input SNR conditions are fairly high, the presence of the amplitude variations makes the SCR conditions low, thus making the detection using the reference RMD algorithm impossible, see fig. 5.11(a). The developed RMD algorithm, on the other hand, is able to separate the respiratory motion response and the non-stationary clutter in a satisfactory manner, as demonstrated in fig. 5.11(b). Coincidentally, as in the previous case, the third decision matrix contains the respiratory motion response and the second decision matrix did not pass the threshold.

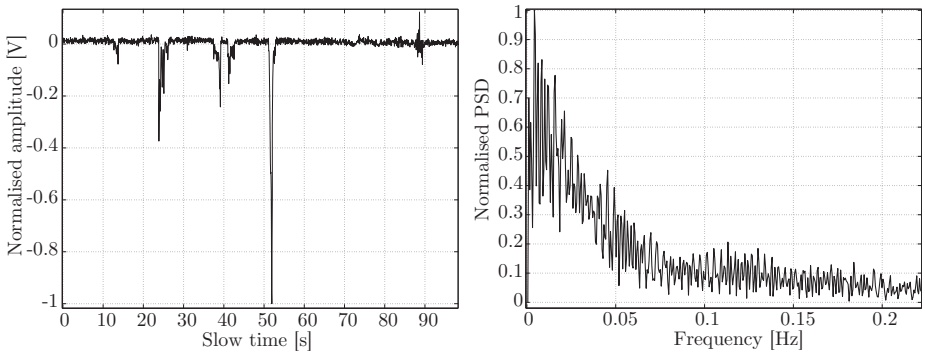

Figure 5.10: *A slow-time vector $\boldsymbol{r}_n[k]$ illustrating sudden amplitude jumps originating in the data acquisition equipment (left) and its power spectrum $\left|\boldsymbol{r}_n^{fd}[\kappa]\right|$ (right).*

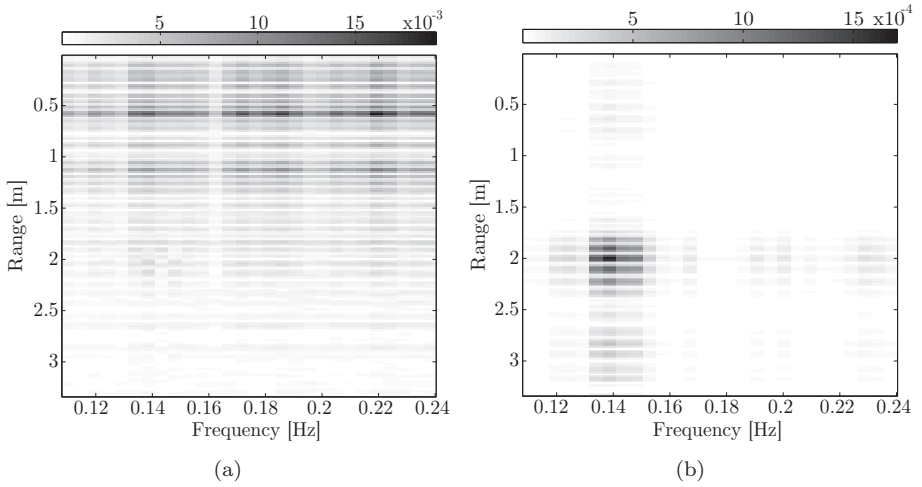

Figure 5.11: *Decision matrices for the case study II: a) reference RMD algorithm, $\left|\check{\mathbf{R}}^{fd}\right|$; b) $|\boldsymbol{D}_3|$ - strong respiratory motion response visible.*

5.10 Conclusion

This chapter investigates the performance of three stationary-clutter subtraction methods: range profile subtraction (RPS), mean subtraction (MS) and linear-trend subtraction (LTS) method. It has been shown that the MS method should be avoided since it increases the AWGN power and acts as a differentiator, thereby resulting in frequency-dependent noise floor. The RPS and LTS method

show identical performance in the absence of any amplitude instability. However, in the presence of amplitude instability the LTS method performs better and since amplitude instability is common under real-life scenarios, the preferred method for use in UWB-radar-based trapped-victim detection operations is therefore the LTS method. However, the main contribution of this chapter is presentation of a novel human respiratory motion detection algorithm for use in UWB-radar-based trapped-victim detection operations. The novelty of the chosen approach assumes complete lack of knowledge of the respiratory motion response waveform, thus making the implementation of matched filter not feasible, but assuming the knowledge of the average breathing frequency. The main novelty, though, is to consider the presence of non-stationary clutter and low SNCR that have been shown to commonly occur in real-life situations. The algorithm separates the respiratory motion response from the non-stationary clutter and applies a threshold for a decision making process. The performance of the RMD algorithm is assessed both by means of Monte Carlo simulation as well as on data acquired under realistic conditions using an UWB pseudo-random noise radar. Its performance is compared to that of a previously reported RMD algorithm by Zaikov et al. The results of the performance comparison study show a significant increase in performance of the developed RMD algorithm over the reference RMD algorithm in terms of its denoising capabilities, but most significantly, non-stationary clutter separation. This invariably leads to a significantly higher detection rate in low SNCR conditions than for the reference RMD algorithm, as demonstrated both by means of simulation and experimental verification. The developed RMD algorithm is computationally efficient as the computational time (using a standard dual-core processor) of a dataset acquired during 10 minutes is less than 2 seconds. The developed RMD algorithm is the first of its kind that is able to separate the non-stationary clutter from the respiratory motion response, complemented with a semi-automatic target decision functionality. The obtained results that confirm this statement ultimately indicate that the USAR crews will have significantly higher chances of saving lives of trapped human beings if using the developed RMD algorithm compared to any existing RMD algorithm, regardless of used (baseband-)UWB radar technology and other hardware.

References

[1] V. Chernyak, "Signal processing in multisite UWB radar devices for searching survivors in rubble," in *Proc. EuRad 2006*, Sep. 2006, pp. 190-193.

[2] J. Sachs, M. Aftanas, S. Crabbe, M. Drutarovsky, R. Klukas, D. Kocur, T. Nguyen, P. Peyerl, J. Rovnakova, and E. Zaikov, "Detection and tracking of moving or trapped people hidden by obstacles using ultra-wideband pseudo-noise radar," in *Proc. EuRad 2008*, Oct. 2008, pp. 408–411.

[3] W. Shrader and V. Gregers-Hansen, *MTI Radar*, ser. Radar Handbook. McGraw Hill, 2008, vol. 3, pp. 2.1–2.9.

[4] C. Stauer and W. Grimson, "Adaptive background mixture models for real-time tracking," in *Proc. of CVPR '99*, 1999, pp. 246–252.

[5] K. Toyama, J. Krumm, B. Brumitt, and B. Meyers, "Wallflower: Principles and Practice of Background Maintenance," in *Proc. of Int. Conf. on Computer Vision (ICCV '99)*, Sep. 1999, pp. 256–261.

[6] R. Zetik, S. Crabbe, J. Krajnak, P. Peyerl, J. Sachs, and R. Thom, "Detection and localization of persons behind obstacles using M-sequence through-the-wall radar," in *SPIE Defense and Security Symposium*, Apr. 2006, pp. 6201–6219.

[7] C. Wren, A. Azarbayejani, T. Darrell, and A. Pentland, "Pfinder: Real-time tracking of the human body," *IEEE Trans. on Patt. Anal. and Machine Intell.*, vol. 19, no. 7, 1997, pp. 780–785.

6

Narrowband interference suppression

A major contribution to a decrease in SNR conditions is attributed to the interference from external radio transmitters, also called narrowband interference (NBI). The term NBI encompasses any unwanted, externally transmitted modulated or unmodulated sinusoidal waveform having a fixed carrier frequency and bandwidth which is a fraction of the bandwidth of the UWB signal. Due to the implementation of stroboscopic sampling in impulse radar and pseudo-random noise radar used for sensing, NBI is randomised into coloured Gaussian noise. Although NBI can be suppressed by means of an analogue notch filter, such approach introduces undesired ringing of the human target response from the victim, which further results in deterioration of the down-range resolution. There is therefore a strong need for NBI suppression methods in time-domain radar, with the aim of causing minimal effect on the waveform and the energy of the backscattered response from the victim.

6.1 Motivation and aim

The frequency spectrum within and slightly below the UHF band, which is of largest interest for any search-and-rescue radar system, is, e.g. in the USA, densely occupied by various radio services (TV broadcasting, mobile, aeronautical navigation etc.) [1]. It is of highest importance for such radar system to remove any interference which might reduce its performance, including narrowband interference from the radio services operating within the same frequency spectrum. Given the fact that time-domain radar technology is the most widely used UWB radar technology for UWB-radar-based trapped-victim detection operations and the fact that such radar systems almost exclusively implement stroboscopic sampling, the resulting NBI manifests itself as wideband, coloured Gaussian noise, due to heavy undersampling of the NBI, see section 6.3. The increase in noise floor over the used range of frequencies results in lower SNR conditions. There is therefore a need to develop signal processing methods for suppression of NBI in UWB search-and-rescue radar systems.

6.2 Previous approaches to NBI suppression in UWB radar

An approach to suppress the narrowband interference consists of determining the direction-of-arrival of the interferer followed by beamforming at the receiver side. A null is placed in the direction-of-arrival of the interferer, thus resulting in reduced received signal level of NBI. This approach is not applicable, however, for UWB-radar-based trapped-victim detection purposes since beamforming requires antenna arrays, which are of no practical use for UWB signals at lower frequencies due to their large size.

Another approach relies on simple NBI mitigation scheme for UWB signals using multiple receive antennas [2]. The low spatial fading characteristic of UWB signals is exploited to provide "interference diversity" by selecting the signal with the lowest received power among multiple antennas. Although this approach is perfectly feasible for UWB communication purposes, it is, however, not feasible for use in UWB-radar-based victim detection since the signals from all deployed antennas need to used. One simply cannot afford to implement a multi-static radar configuration only to use the signal coming from a single antenna.

A novel approach proposed by Miller et. al makes use of prior information to achieve better results than existing algorithms in a fraction of the computational time [2]. The NBI suppression in UWB (impulse) synthetic aperture radar (SAR) is achieved by the use of the estimate-and-subtract method. The algorithm estimates the UWB target returns which are subtracted from the receive radar data record. Then, the algorithm estimates high energy sinusoidal interference terms and subtracts them from the original data record. This basic principle of the method is used in one of the proposed methods herein. It is noteworthy, however, that the sampling method of the backscattered returns in [2] is real-time sampling and not stroboscopic sampling. The result is that the waveform of the interferers is preserved in the receive radar data record, thus facilitating their parameter estimation.

The most straightforward method for NBI suppression is filtering out the NBI by means of a bandstop filter. Although it is very efficient in this respect, it is nevertheless not a feasible solution due to creation of ringing in the human target response $\mathbf{h}^*[n]$, thereby worsening the down-range resolution of the radar. The ringing is a result of the so called Gibbs phenomenon which states that discontinuous functions in a wide frequency band will have slowly decaying Fourier coefficients causing Fourier series to converge slowly [3].

6.3 Randomisation of non-coherent waveforms

To realise how narrowband interference is transformed into coloured Gaussian noise we first observe that periodically sampled narrowband signal with sampling frequency f_s has a spectrum according to [4]:

$$S[f_d] = S_x[f_d] + \sum_{k=-\infty}^{\infty} \left[S_x\left[k \cdot f_s + f_d\right] + S_x^*\left[k \cdot f_s - f_d\right]\right] \qquad \boxed{6.1}$$

where $S_x(f_d)$ and $S_x^*(f_d)$ are the spectra of the original signal and its complex conjugate, respectively, and f_d denotes a discrete frequency. We see that replicas of the spectra $S_x(f_d)$ and $S_x^*(f_d)$ are repeated with fixed intervals of f_s in increasing and decreasing frequency direction, respectively. Thus, if $B_i > f_s/2$, where B_i is the bandwidth of the NBI, overlapping of replicas occurs (aliasing). The overlapping of spectra in frequency domain results in distortion of the signals in time domain, depending on the degree of overlapping. However, the majority of the distortion (and thereby randomisation) of the NBI arises from the use of averaging on aperiodic and incoherent signals. The result is an increase of noise floor over the whole frequency range of interest (although not uniformly). The frequency content of the resulting interference is translated to ultra-wide frequency bands since the effective sampling frequency is several orders of magnitude larger than the actual sampling frequency of the NBI (equal to the PRF of the radar device).

A measured example of such randomisation effect can be seen in fig. 6.1 which shows normalised power spectral density of a randomised signal coming from a GSM mobile phone unit, placed in the boresight direction of the receive antenna, as recorded by a stroboscopic sampler with pulse repetition frequency $f = 1/T = 10$ MHz, effective sampling time $t_s = 5$ ps, averaging value $L = 256$ and no UWB signal energy present. The shape of the randomised signal in the frequency domain can be described by the Gaussian distribution, having a mean value of ca. 3.5 GHz and standard deviation in the order of a few GHz. The mean and the standard deviation are function of the acquisition parameters, as well as the parameters of the interfering signal.

6.4 Proposed NBI suppression methods

In this section we suggest four methods for NBI suppression. We have focused on two diametrically different approaches to solve the problem. The first approach is to extract the narrowband interference, sample it stroboscopicly and subtract the result from the data. The other approach relies on filtering out the narrowband interference by means of an analogue bandstop filter and, after analogue-to-digital (AD) conversion, filling-up the spectral notch created

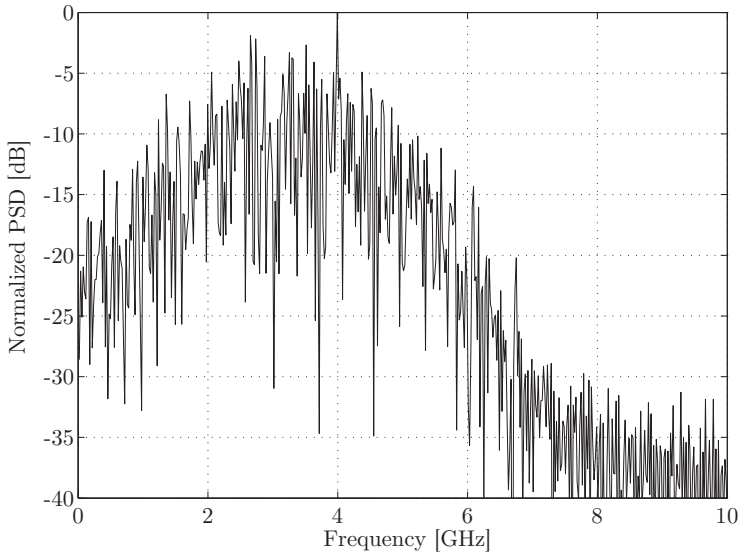

Figure 6.1: *Normalised PSD of randomised interference coming from a GSM mobile phone unit*

by the filter in order to reduce ringing. In this section we present two variations of both approaches and compare the performance of all the four methods in terms of NBI suppression, ringing suppression (where applicable), as well as signal energy and waveform preservation. All following methods apply low-pass filtering in order to suppress high-frequency out-of-band noise.

6.4.1 Extract-and-Subtract (EandS) method

Extract-and-Subtract (EandS) method is based on the idea of extracting sampled NBI, $\mathbf{i}_l[n]$, and subtracting it from each l-th sampled range profile $\mathbf{r}_l[n]$. EandS method does not treat the NBI as disturbance of the $\mathbf{h}_l^*[n]$; instead it treats $\mathbf{h}_l^*[n]$ and $\mathbf{c}[n]$ as unwanted disturbances to $\mathbf{i}_l[n]$.

Fig. 6.2 shows the block scheme of the EandS method. The range profile before AD-conversion, $r(t)$, is divided into two branches. In the first branch, $r^{(1)}(t)$ is bandpass-filtered using an analogue bandpass filter, which is tuned to the centre frequency and the bandwidth of $i(t)$; it then is stroboscopicly sampled resulting in:

$$\tilde{\mathbf{r}}_l^{(1)}[n] = \mathbf{f}_a[n] * \mathbf{r}_l^{(1)}[n] = \tilde{\mathbf{h}}_l[n] + \tilde{\mathbf{c}}[n] + \mathbf{i}_l[n] + \tilde{\mathbf{z}}_l^{(1)}[n] \qquad (6.2)$$

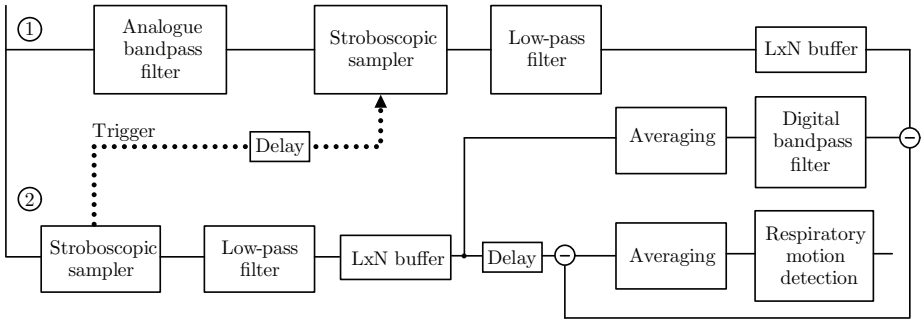

Figure 6.2: *Block scheme of the Extract-and-Subtract method*

where

$$\mathbf{h}[n] = \begin{cases} 0 & \text{if } 1 \le n \le n^* - 1 \\ \mathbf{h}^*[n] & \text{if } n^* \le n \le n^* + N^* - 1 \\ 0 & \text{if } n^* + N^* \le n \le N \end{cases}$$

$[\,\tilde{\cdot}\,]$ denotes a bandpass-filtered waveform; $\mathbf{c}[n]$ and $\mathbf{f}_a[n]$ respectively denote the stationary clutter and the digitised impulse response of the analogue bandpass filter. $\tilde{\mathbf{r}}_l^{(1)}[n]$ is stored in an $L \times N$ buffer for further processing. In order to extract $\mathbf{i}_l[n]$ from $\mathbf{r}_l[n]$, the influence of $\tilde{\mathbf{h}}_l^*[n]$ and $\tilde{\mathbf{c}}[n]$ needs to be estimated and removed. The best estimate of $\mathbf{h}_l^*[n]$ and $\mathbf{c}[n]$ is achieved by applying averaging:

$$\begin{aligned} \hat{\mathbf{h}}_l[n] + \hat{\mathbf{c}}[n] &\stackrel{def}{=} \mathbf{r}_k[n] = \frac{1}{L}\sum_{l=1}^{L} \mathbf{r}_l[n] \\ &= \mathbf{h}_k[n] + \mathbf{c}[n] + \mathbf{i}_k[n] + \mathbf{z}_k[n] \end{aligned} \qquad (6.3)$$

where $[\,\hat{\cdot}\,]$ denotes estimation. Digital bandpass filtering and subsequent removal of $\tilde{\mathbf{h}}_l^*[n]$ and $\tilde{\mathbf{c}}[n]$ results in the estimate of $\mathbf{i}_l[n]$:

$$\begin{aligned} \hat{\mathbf{i}}_l[n] &= \tilde{\mathbf{r}}_l^{(1)}[n] - \mathbf{f}_d[n] * \mathbf{r}_k[n] \\ &= \tilde{\mathbf{h}}_l[n] + \tilde{\mathbf{c}}[n] + \tilde{\mathbf{i}}_l[n] + \tilde{\mathbf{z}}_l^{(1)}[n] \\ &- \left(\tilde{\mathbf{h}}_k[n] + \tilde{\mathbf{c}}_k[n] + \tilde{\mathbf{i}}_k[n] + \tilde{\mathbf{z}}_k[n]\right) \\ &= \mathbf{i}_l[n] + \tilde{\mathbf{i}}_k[n] + \tilde{\mathbf{z}}_k[n] + \tilde{\mathbf{z}}_l^{(1)}[n] \end{aligned} \qquad (6.4)$$

where $\mathbf{f}_d[n]$ is the impulse response of the digital bandpass filter having the same characteristics as its analogue counterpart. In the second branch $r^{(2)}(t)$ is sampled using a stroboscopic sampler which is synchronised using the triggering pulse from the stroboscopic sampler in the first branch. The triggering pulse is delayed corresponding to the time group delay of the analogue bandpass filter in

the first branch. The estimate of the NBI, $\hat{\mathbf{i}}_l[n]$, is subtracted from the obtained range profile in the second branch, $\mathbf{r}_l^{(2)}[n]$, thereby obtaining:

$$\begin{aligned}\mathbf{r}_{l,\mathrm{proc}}[n] &= \mathbf{r}_l^{(2)}[n] - \hat{\mathbf{i}}_l[n] \\ &= \mathbf{h}_k[n] + \mathbf{c}[n] + \tilde{\mathbf{i}}_k[n] + \tilde{\mathbf{z}}_k[n] + \tilde{\mathbf{z}}_l^{(1)}[n] + \mathbf{z}_l^{(2)}[n] \\ &= \mathbf{h}_k[n] + \mathbf{c}[n] + \mathbf{w}_{l,\mathrm{proc}}[n] \end{aligned} \quad (6.5)$$

where the index "proc" denotes processed range profile and $\mathbf{w}_l[n]$ is the resulting noise term vector. This results in the variance $\mathrm{var}\{\mathbf{w}_{l,\mathrm{proc}}\} < \mathrm{var}\{\mathbf{w}_l\}$ since the influence of $\mathrm{var}\{\mathbf{i}_l\}$ has been removed and $\mathrm{var}\{\tilde{\mathbf{z}}_k\} \ll \mathrm{var}\{\tilde{\mathbf{z}}_l^{(1)}\} \ll \mathrm{var}\{\mathbf{z}_l^{(2)}\}$. The processed range profile $\mathbf{r}_{l,\mathrm{proc}}[n]$ is averaged and stored in a matrix for the purpose of respiratory motion detection.

6.4.2 Extract-and-Subtract Least Square Estimate (EandS-LSE) method

Implementation of the Extract-and-Subtract Least-Square Estimate (EandS-LSE) method is based on the assumption that the NBI can be regarded as a sinusoid, which can be fully described by its parameters: frequency, amplitude and phase. For a short period of time, in the order of a few periods around the sampling points of $r(t)$, $T_s = n \cdot (T + t_s)$, these three parameters are assumed to be time-invariant and can be determined using an estimator. The implementation of the EandS-LSE method consists of two branches, see fig. 6.3. The upper branch in fig. 6.3 is used for down-conversion to baseband as well as real-time sampling of the bandpass-filtered NBI. The sampled baseband NBI, $\mathbf{i}_b[n]$, is expressed as:

$$\begin{aligned}\mathbf{i}_b[n] &= a\cos(\omega_b n + \phi) + \mathbf{y}_b[n] + \mathbf{z}_b[n] \\ &= \alpha_1 \cos(\omega_b n) + \alpha_2 \sin(\omega_b n) + \mathbf{y}_b[n] + \mathbf{z}_b[n] \end{aligned} \quad (6.6)$$

where $\mathbf{y}_b$ denotes the baseband (down-converted) UWB-waveform residuals and $\mathbf{z}_b$ denotes baseband AWGN; $\alpha_1 = a\cos(\phi)$, $\alpha_2 = -a\sin(\phi)$, a, ϕ and ω_b denote the amplitude, the modulated baseband angular frequency and the phase of $\mathbf{i}_b[n]$, respectively. A short segment of $\mathbf{i}_b[n]$, $\mathbf{i}_b'[n]$, where $n' = \{1, \ldots, N'\}$ and $N' < N$, is acquired around the sampling points T_s. The sampling points are obtained from the time-of-arrival of the delayed triggering pulse from the stroboscopic sampler in the second branch. Next, the amplitude a and the phase ϕ of $\mathbf{i}_b[n]$ need to be estimated. Estimates of a and ϕ of $\mathbf{i}_b[n]$, which is a nonlinear function of ϕ, can be obtained by a change of parameters, according to:

$$a = \sqrt{\alpha_1^2 + \alpha_2^2} \quad (6.7)$$

$$\phi = \arctan\left(\frac{-\alpha_2}{\alpha_1}\right). \quad (6.8)$$

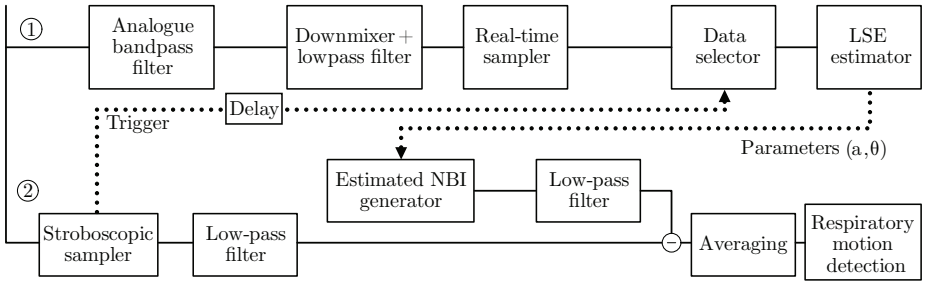

Figure 6.3: *Block scheme of the Extract-and-Subtract Least-Squares Estimate method*

$\boldsymbol{\alpha} = [\alpha_1, \alpha_2]^T$ can be estimated for a given frequency (which is assumed to be known) using a least-squares estimator:

$$\hat{\boldsymbol{\alpha}} = (\mathbf{A}^T\mathbf{A})^{-1}\mathbf{A}^T\mathbf{i}_b[n] \qquad 6.9$$

where

$$\mathbf{A} = \begin{bmatrix} 1 & 0 \\ \cos(\omega_b) & \sin(\omega_b) \\ \vdots & \vdots \\ \cos((N-1)\omega_b) & \sin((N-1)\omega_b) \end{bmatrix}$$

Next, $\hat{a}$ and $\hat{\phi}$ are used for generating an estimate of the stroboscopicly sampled NBI, $\hat{\mathbf{i}}[n]$, obtained at each sampling point T_s. In the lower branch in fig. 6.3, $\mathbf{r}_l[n]$ is obtained by stroboscopicly sampling $r^{(2)}(t)$ and low-pass filtering it in order to remove high-frequency AWGN. The obtained estimate of the NBI, $\hat{\mathbf{i}}_l[n]$, is subtracted from $\mathbf{r}_l[n]$, resulting in:

$$\begin{aligned} \mathbf{r}_{l,\mathrm{proc}}[n] &= \mathbf{r}_l[n] - \hat{\mathbf{i}}_l[n] \\ &= \mathbf{h}_k[n] + \mathbf{c}[n] + \mathbf{i}_l[n] + \mathbf{z}_l[n] - (\mathbf{i}_l[n] + \mathbf{w}_l[n]) \\ &= \mathbf{h}_k[n] + \mathbf{c}[n] + \mathbf{z}_l[n] + \mathbf{w}_l[n] \end{aligned} \qquad 6.10$$

where $\mathbf{w}_l[n]$ incorporates the noise terms originating from the down-conversion of the UWB signal, mismatch in modeling and AWGN.

6.4.3 Filter-and-Restore (FandR) method

The Filter-and-Restore (FandR) method, see fig. 6.4, suppresses the $i(t)$ using a bandstop filter, which, as mentioned in previous paragraph, introduces ringing in the remaining $\mathbf{r}_k[n]$.

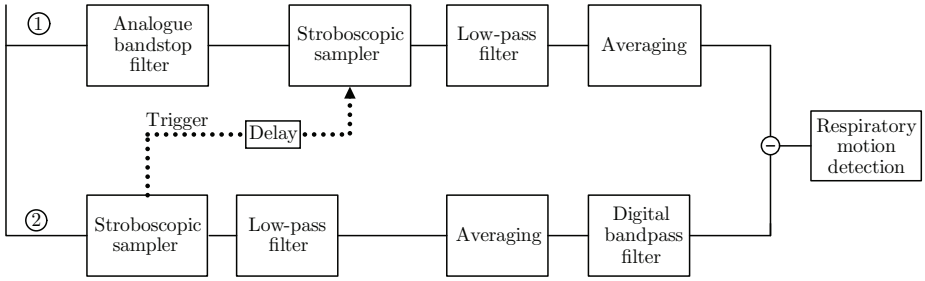

Figure 6.4: *Block scheme of the Filter-and-Restore method*

In order to restore $\mathbf{r}_k[n]$ to its original shape, the power spectrum of $\mathbf{r}_k[n]$ is used to extract the missing spectral data. Although $\mathbf{r}_k[n]$ contains randomised NBI, $\mathbf{i}_k[n]$, the frequency band needed from this signal to fill the spectral gap will contain only a small part of the original NBI energy. In the first branch, $r^{(1)}(t)$ is first bandstop-filtered to suppress the NBI and then stroboscopicly sampled (triggered by the delayed triggering pulse from the sampler in the second branch), lowpass-filtered and averaged. In the second branch, $r^{(2)}(t)$ is stroboscopicly sampled, lowpass-filtered and averaged. A bandpass filter is then applied, which is tuned to the same centre frequency and having the same bandwidth as the corresponding analogue band-stop filter in the first branch. The time-domain representation of the extracted spectrum, $\mathbf{g}_k[n]$, is expressed as:

$$\mathbf{g}_k[n] = \tilde{\mathbf{h}}_k[n] + \tilde{\mathbf{c}}[n] + \tilde{\mathbf{i}}_k[n] + \tilde{\mathbf{z}}_k^{(2)}[n] \qquad \boxed{6.11}$$

The ringing in $\mathbf{r}_k^{(1)}[n]$ is mitigated by the addition of $\mathbf{g}[n]$, which is equivalent to filling up the missing spectrum in the frequency domain, thus resulting in $\mathbf{r}_{k,\mathrm{proc}}[n]$, given by:

$$\begin{aligned} \mathbf{r}_{k,\mathrm{proc}}[n] &= \mathbf{r}_k^{(1)}[n] + \mathbf{g}_k[n] \\ &= \check{\mathbf{h}}_k[n] + \check{\mathbf{c}}[n] + \check{\mathbf{z}}_k^{(1)}[n] + \tilde{\mathbf{i}}_k[n] + \tilde{\mathbf{z}}_k^{(2)}[n] \\ &= \check{\mathbf{h}}_k[n] + \check{\mathbf{c}}[n] + \mathbf{w}_{k,\mathrm{proc}}[n]. \end{aligned} \qquad \boxed{6.12}$$

where $[\ \check{\cdot}\ ]$ denotes the bandstop filtering operation and $\mathbf{w}_{k,\mathrm{proc}}[n]$ is the resulting noise term vector. As in the case of the EandS method, the variance $\mathrm{var}\{\mathbf{w}_{\mathrm{proc}}\} < \mathrm{var}\{\mathbf{w}\}$, since the influence of NBI has been suppressed. The processed range profile $\mathbf{r}_{k,\mathrm{proc}}[n]$ is stored in a matrix for the purpose of respiratory motion detection.

6.4.4 Linear-Interpolation-based Filter-and-Restore (FandR-LI) method

The approach of the Linear-Interpolation-based Filter-and-Restore (FandR-LI) method to suppress the NBI is to interpolate the spectrum of the bandstop-filtered and averaged range profile $\tilde{\mathbf{r}}_k[n]$ in the frequency region of the applied bandpass filter.

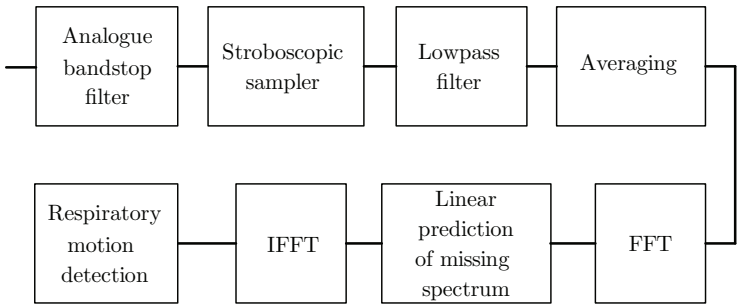

Figure 6.5: *Block scheme of the Filter-and-Restore Linear Interpolation method*

The sampled and averaged range profile in the frequency domain, $\boldsymbol{\mathcal{R}}[k,\mu]$, where $\mu = \{0,\ldots,N-1\}$ represents discrete frequency sample points, can be written in its polar coordinates, $\boldsymbol{\rho}[\mu]$ and $\boldsymbol{\theta}[\mu]$:

$$\boldsymbol{\mathcal{R}}[\mu] = \mathbf{X}[\mu] + i\mathbf{Y}[\mu] = \boldsymbol{\rho}[\mu]\cdot[\cos(\boldsymbol{\theta}[\mu]) + i\sin(\boldsymbol{\theta}[\mu])] \tag{6.13}$$

where $\mathbf{X}[\mu] = \Re\{\boldsymbol{\mathcal{R}}_k[\mu]\}$, $\mathbf{Y}[\mu] = \Im\{\boldsymbol{\mathcal{R}}_k[\mu]\}$, $i = \sqrt{-1}$, $\boldsymbol{\rho}[\mu]$ and $\boldsymbol{\theta}[\mu]$ are the magnitude and phase, respectively, given by:

$$\boldsymbol{\rho}[\mu] = \sqrt{\mathbf{X}^2[\mu] + \mathbf{Y}^2[\mu]} \tag{6.14}$$

$$\boldsymbol{\theta}[\mu] = \tan^{-1}\left(\frac{\mathbf{Y}[\mu]}{\mathbf{X}[\mu]}\right). \tag{6.15}$$

The magnitude $\boldsymbol{\rho}[\mu]$ is linearly interpolated by calculating the values on a straight line between the boundary points of the gap. This is achieved by:

$$\hat{\boldsymbol{\rho}}[\mu] = \boldsymbol{\rho}[\mu_l] + \mu\cdot\left(\frac{\boldsymbol{\rho}[\mu_h] - \boldsymbol{\rho}[\mu_l]}{\mu_h - \mu_l}\right) \tag{6.16}$$

where μ_l and μ_h are respectively the lowest and highest frequency sample points outside the filtering process and therefore not attenuated by the filter. The phase cannot be interpolated in exactly the same way, since the spectral gap influences $\boldsymbol{\theta}[\mu]$ differently then $\boldsymbol{\rho}[\mu]$. Therefore, $\boldsymbol{\theta}[\mu]$ is linearly extrapolated using the first phase value $\boldsymbol{\theta}[0]$ and the last non-extrapolated phase value $\boldsymbol{\theta}[\mu_l]$ according to:

$$\hat{\boldsymbol{\theta}}[\mu] = \boldsymbol{\theta}[\mu_l] + \mu\cdot\frac{\boldsymbol{\theta}[\mu_l] - \boldsymbol{\theta}[0]}{\mu_l} \tag{6.17}$$

where $\hat{\boldsymbol{\theta}}[\mu]$ is the value of the extrapolated phase at frequency point $\mu > \mu_l$. The corresponding values of restored $\boldsymbol{\mathcal{R}}_{k,\mathrm{proc}}[\mu]$ are computed using eq. 6.13. The IFFT operation is used for transferring $\boldsymbol{\mathcal{R}}_{k,\mathrm{proc}}[\mu]$ back into time domain. The resulting processed range profile $\mathbf{r}_{k,\mathrm{proc}}[n]$ is stored in a matrix for the purpose of respiratory motion detection.

6.5 Simulations

In this section the simulation parameters, performance criteria and approach to model $i(t)$ are presented and elaborated.

6.5.1 Waveform generators

The human target response vector $\mathbf{h}^*[n]$ used for simulation is shown in fig. 6.6 as a thick line and having normalised amplitude. It is a measured response from the chest area of an actual standing person in line-of-sight conditions using the UWB impulse radar. Clutter is not included in the simulation process, since it is regarded uniteresting for the performance assessment of the proposed NBI suppression methods. Generating a discrete-time vector $\mathbf{i}$, which models the analogue NBI, $i(t)$, for the duration of one range profile, requires generation of $(T/\delta t) \cdot N \cdot L = 6.4 \cdot 10^8$ points, where the parameters follow from table 6.1.

Table 6.1: *Simulation parameters*

Parameter		**Value**
Time resolution	δt	5 ps
Pulse repetition interval	T	100 ns
Sampling time	t_s	5 ps
Number of samples	N	2000
Averaging value	L	16
Number of range profiles	K	1
Sample index of $\mathbf{h}^*[n]$	n^*	1150
Signal-to-Noise Ratio	(SNR)	15 dB
Interference-to-Noise Ratio	(INR)	48 dB
Bandwidth	B_i	150 MHz
Bandpass filter order		330
Bandpass filter passband	(in GHz)	1.75 - 1.90
Bandstop filter order		1670
Bandstop filter stopband	(in GHz)	1.75 - 1.90
Lowpass filter order		544
Lowpass filter passband	(in GHz)	5
Lowpass filter stopband	(in GHz)	6

Generating such a vector is highly time and memory consuming and is therefore not feasible for the simulation purposes using a standard PC. Instead, $\mathbf{i}$ is generated having $1.5 \cdot N \cdot (T/\delta t) = 6 \cdot 10^7$ points. For each obtained $\mathbf{r}_l$, vector $\mathbf{i}_l$ with random starting point is "sampled" from $\mathbf{i}$ according to the parameters in table 6.1. A factor of "1.5" is subjectively chosen as a trade-off between independence of $\mathbf{i}_l$ vectors and the order of complexity. $\mathbf{i}$ is modulated as a GSM signal. A normal, single channel GSM signal occupies only 200 kHz, but a number of GSM channels located within the bandwidth of 150 MHz constitute the actual GSM interference signal. However, since it is highly time consuming to generate multiple GSM signals, as would be more realistic, only a single GSM signal with a bandwidth of 150 MHz is therefore generated. A signal having bandwidth of 150 MHz is typically considered a wideband signal and not narrowband. However, 150 MHz constitutes a fraction of the bandwidth of the human target response and can be considered narrowband in relation to it. Furthermore, the methods to suppress narrowband interference signals presented herein are equally applicable in the case of moderately wideband signals.

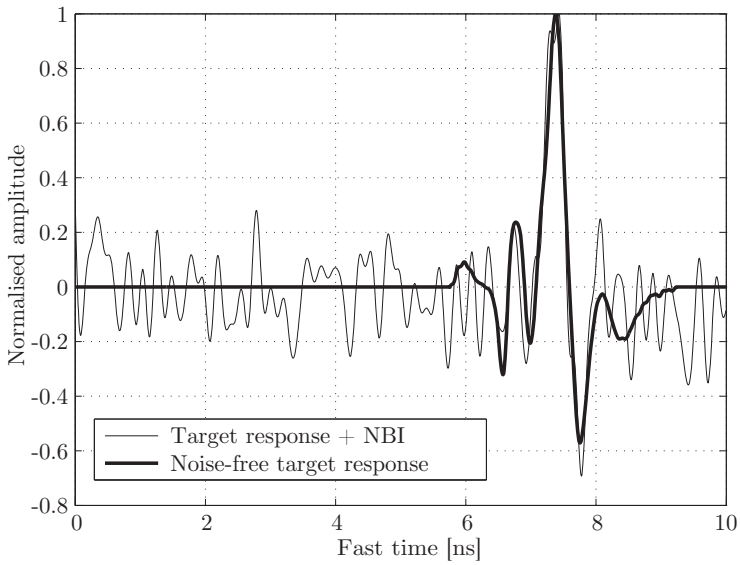

Figure 6.6: *Range profile prior to processing. Noise-free human target response is shown with thick line.*

6.5.2 Simulation parameters

A least squares FIR band-pass filter of order 330 with a passband ranging from 1.75 - 1.90 GHz is used both as the analogue and digital band-pass filter. A minimum order equiripple FIR band-stop filter of order 1670 with stop-band ranging from 1.75 - 1.90 GHz is used as implementation of the band-stop filter. The low-pass filter used is minimum order equiripple FIR low-pass filter with order 544 and $f_{pass} = 5.0$ GHz and $f_{stop} = 6.0$ GHz. Table 6.1 provides the used simulation parameters during the simulation process.

6.5.3 Performance criteria

The simulation results are compared on:

- Amount of NBI suppression (R)
- Amount of ringing suppression (R_{ring}) (where applicable)
- Preservation of waveform (W)
- Preservation of signal energy (E_{diff})

The improvement factor R is measured as the increase in Signal-to-Noise-and-Interference Ratio (SNIR) and is given by:

$$R = SNIR_{\text{proc}} - SNIR_{\text{orig}} \tag{6.18}$$

where SNIR is obtained from:

$$SNIR = 20 \log_{10} \left(\frac{\max\{|\mathbf{r}|\}}{\sigma_r} \right) \quad dB \tag{6.19}$$

where σ_r is the standard deviation of the first half of the range profile, i.e. the region where human target response is not present. The interference and noise have the same bandwidth. The ringing improvement factor R_{ring} is defined as:

$$R_{ring} = 20 \log_{10} \left(\frac{\sigma_r}{\sigma_{r_{\text{proc}}}} \right) \quad dB \tag{6.20}$$

In order to obtain a fair estimate of the parameters W and E_{diff}, the simulation and subsequent evaluation of the parameters were done in the noise- and interference-free case. W is defined as:

$$W = \frac{\|\mathbf{r}_{\text{proc}} - \mathbf{r}\|}{\|\mathbf{r}_{k,\text{proc}}\| + \|\mathbf{r}\|} \cdot 100\% \tag{6.21}$$

where $\| \cdot \|$ denotes the Euclidean norm. The preservation of signal energy is given as $E_{\text{diff}} = ((E_{\text{proc}}/E) - 1) \cdot 100\%$, where $E_{\text{proc}} = \sum_{n=1}^{N} \mathbf{r}_{\text{proc}}^2[n]$ and $E = \sum_{n=1}^{N} \mathbf{r}^2[n]$, denote the energy of the processed and unprocessed range profile, respectively.

6.6 Simulation results

Simulation results are given in table 6.2 which shows the SNIR and ringing improvement factors, preservation of waveform and preservation of signal energy of each of the four investigated methods.

Table 6.2: *Simulation results*

Parameter	EandS	EandS-LSE	FandR	FandR-LI
R	7.7 dB	4.4 dB	9.1 dB	12.9 dB
R_{ring}	N/A	N/A	3.0 dB	7.1 dB
W	4.7%	10.6%	10.0%	7.7%
E_{diff}	-7.2%	-7.0%	-1.8 %	-4.9%

The EandS-LSE method, with 4.4 dB reduction in NBI, performs worst of all four methods. This method has also the highest influence on the waveform, as seen in fig. 6.7(b). The results can be attributed to the estimation and subtraction of a part of the backscattered target response, degrading its waveform and energy. With an NBI reduction of $R = 7.7$ dB, the EandS method performs second worst in terms of reduction, but shows the best preservation of waveform of all methods (see fig. 6.7(a)), although it does affect the signal energy more than any of the other methods. EandS method is suited as a method for NBI suppression, mainly because of the waveform preservation capabilities. However, the need of an extra AD converter and buffers increase the hardware costs and power consumption of this method.

The FandR method performs better in terms of reduction of NBI compared with the EandS method, and is even simpler to implement. However, it is not capable of effectively removing the ringing because of a phase difference, see fig. 6.7(c). Furthermore, this method does not exhibit very good preservation of the waveform, although it affects the signal energy the least. The FandR-LI method is best capable of suppressing the NBI, performs best in terms of signal energy preservation and second best in preserving the waveform, see fig. 6.7(d) and table 6.2. It is much better capable of suppressing ringing then the FandR method. This method is the only method which only needs one channel, saving hardware costs and power consumption. The FandR-LI method is therefore the best suited method for narrowband interference suppression in stroboscopic samplers.

6.7 Conclusion

In this chapter we have analysed the performance of four developed methods for narrowband interference suppression implemented in stroboscopic samplers and used in trapped-victim detection applications. The Extract-and-Subtract

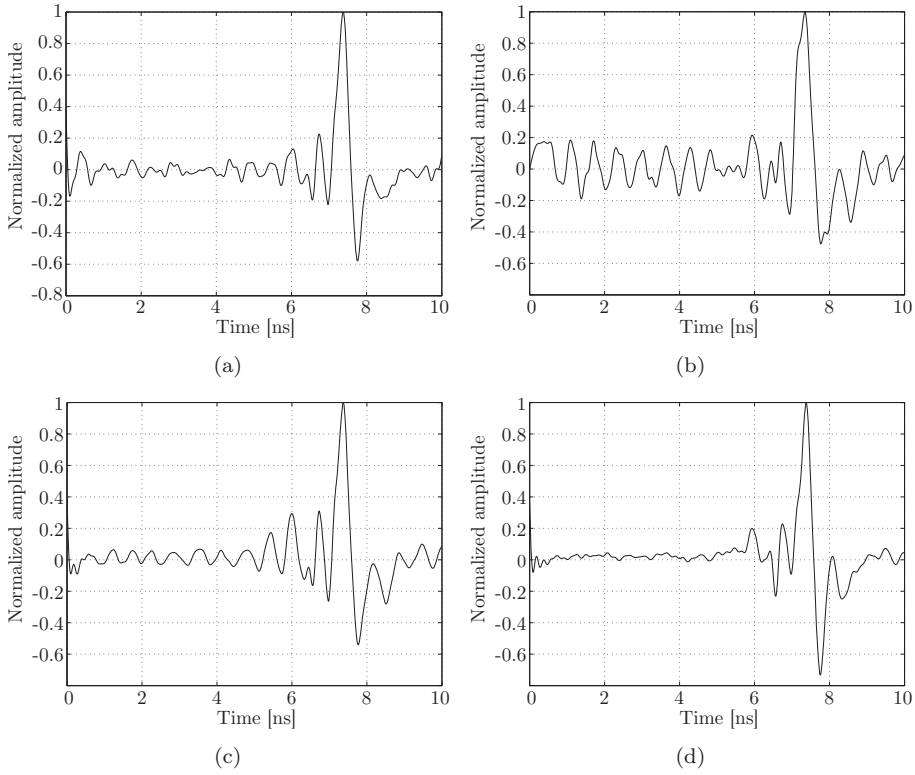

Figure 6.7: *Obtained range profile using: a) Extract-and-Subtract method; b) Extract-and-Subtract Least-Square Estimate method; c) Filter-and-Restore method; d) Filter-and-Restore Linear Interpolation method.*

Least-Squares-Estimate method performed worst both in terms of preservation of signal energy and waveform, but also in amount of NBI suppression. The Extract-and-Subtract method shows the best waveform, whereas its improvement factor $R = 7.7$ dB and signal energy preservation capability E_{diff} are not its strong points. Furthermore, its hardware requirements are the highest of all four methods. Filter-and-Restore method does exhibit good NBI suppression capabilities, and performs better than both of the previous two methods, although its overall performance is out-shadowed by Filter-and-Restore Linear Interpolation method. FandR-LI is the most suitable method for suppressing narrowband interference in stroboscopic samplers. It shows an improvement factor of 12.9 dB in NBI suppression and manages to preserve the signal waveform and energy very well. We showed that there is potentially a substantial improvement in performance of any human being detection algorithm if narrowband interference suppression methods are implemented as well, since the SNR is increased and the waveform is preserved to a large extent. Future research should focus on multiple interferers having varying bandwidths and signal strengths, but most importantly, testing the performance of the methods in real-life scenarios for a high number of different human targets.

References

[1] National Telecommunications and Information Administration. (2003) United States Frequency Allocations - The Radio Spectrum. [Online]. Available: http://www.ntia.doc.gov/osmhome/allochrt.pdf

[2] T. Miller, L. Potter, and J. McCorkle, "RFI suppression for ultra wideband radar," *IEEE Trans. Aerosp. Electron. Syst.*, vol. 33, Oct. 1997.

[3] R. Lyons, *Understanding digital signal processing.* Prentice-Hall, 2004.

[4] I. Bilinskis, *Digital alias-free signal processing.* Wiley, 2007.

7

Conclusions and recommendations for future work

One of the applications of the ultra-wideband (UWB) technology is UWB radar for detection of trapped victims in collapsed buildings due to e.g. an earthquake. The motivation for using UWB for such an application is mainly due to its high resolution capabilities which allows for detection of small-scale movements produced by the victim, such as the respiratory motion. It has furthermore larger ability, compared to narrowband radar, to separate the respiratory motion responses from the non-stationary clutter. Despite the large potential of UWB radar for victim search application, there are several major challenges that need to be tackled for successful employment in real-life conditions:

- low signal-to-noise (SNR) ratios which are the result of high material attenuation, low reflectivity of the human body, highly limited movements of the victim and low spectral power emissions,
- presence of narrowband interference and
- presence of non-stationary clutter originating from moving objects in the vicinity of the rubble site (rescue workers, radar operators, rattling leaves, construction machines etc.).

At the time of these research studies, very little was known about the main target feature used for detection: periodic radar reflections from a breathing human being. All feasibility studies in this particular field performed by other research groups were focused mainly on a single body position, which is laying down and facing the radar. However in real-life conditions, a multitude of other body positions are likely to be faced. Therefore, much more needed to be known about the nature of the human respiratory motion, not only as function of position, but also as function of aspect angle, antenna-pair polarization and antenna placement. More attention should be paid to the feasibility of using heartbeat responses for the detection in challenging conditions. Highly simplified conditions which were not likely to be faced in real-life conditions were

nevertheless commonly assumed, such as reasonably high SNR, absence of both non-stationary clutter and narrowband interference. There was an absence of suggested methods of how these problems might be tackled. There were furthermore no indications on the optimal frequency band for use in rubble made up of randomly-oriented concrete slabs or thick concrete walls. The research presented herein attempted to answer these questions and tackle the abovementioned issues.

7.1 Main results and novelties of the research

The main achieved results are summarized below:

- An experimental study with the aim to provide a guideline for the best choice of UWB radar technology for the purpose of detection of trapped victims, showed that impulse radar manufactured by Geozondas along with a high-end low-noise-amplifier provides the highest SNR values of the respiratory motion responses. The performance comparison involved a state-of-the-art pseudo-random noise radar and a high-end vector network analyzer (VNA). A high-dynamic-range radar device, such as VNA, shows great potential in resolving even the minute movements of the human body, such as cardiac motion. However, VNA cannot be used as a radar device due to the need of proper calibration procedure to suite this particular usage. The novelty of the results lies in the fact that never before had such a comparison between various UWB radar technologies been reported for the purpose of detecting respiratory motion under NLOS conditions.

- An experimental study on the feasibility of using only two target features for UWB-radar-based trapped-victim detection operations, e.g. cardiac- and respiratory motion, showed that the respiratory motion responses are in average 13 dB stronger than cardiac motion responses. Under challenging non-line-of-sight conditions, the respiratory motion responses were shown to be the only feasible target feature for use in the UWB-radar-based trapped-victim detection operations if using commercially available time-domain radar equipment.

- Detectability of the human respiratory motion was assessed experimentally using time-domain impulse radar. The detectability was investigated for four aspect angles (-15°, -30°, 45° and 60°), three antenna-pair polarizations (HH, VV and HV), as well as for three body positions (laying on the stomach, back and side). The importance of the results is the full charac-

terization of the main target feature for UWB-radar-based trapped-victim detection operations and is the first of its kind so far.

- A highly efficient respiratory motion detection algorithm has been developed for detection of trapped victims in low SNR conditions and in presence of non-stationary clutter. The novelty of the algorithm lies in its ability to largely separate the non-stationary clutter from the radar data. The performance of the algorithm was assessed both by means of Monte Carlo simulation and under quasi-real-life conditions. Its performance was shown to be higher than a previously reported algorithm, in particular in terms of clutter rejection. The impact of this research is that the rescue crews stand higher chances of finding trapped survivors if using this detection algorithm, thereby potentially saving more lives in post-disaster scenarios.

- A study has been conducted which compared the performance of three stationary-clutter subtraction methods and assessed their use in UWB-radar-based trapped-victim detection operations. The study used an experimentally acquired data set containing linear amplitude instability (linear trend) originating from the equipment itself. It was shown that the linear-trend subtraction method, which removes the DC and any potential linear trend in the slow-time dimension, performs better than the mean-subtraction- and range-profile subtraction methods.

- The optimal operational frequency band was investigated experimentally using real-life-like sandstone rubble and a concrete wall. It was shown that the frequency ranges below 1 GHz are most suited for UWB-radar-based trapped-victim detection operation. The study, although not a thorough one, is nevertheless useful since it provides an indication on the most appropriate frequency range based on experimental results. To our knowledge, it is the first study of its kind involving real-life-like rubble.

- The influence of narrowband interference can potentially be reduced as a result of development and performance assessment of four narrowband interference suppression algorithms. The algorithms were tailored for use in impulse radars employing the stroboscopic sampling method. The method of filtering out narrowband interference by means of a notch filter and subsequently interpolating the missing spectrum, proved to be the preferred method since it efficiently removes narrowband interference while having only a minor influence on the backscattered waveform from the trapped victim.

7.2 Recommendations for future work

The recommendations for future work in this particular field can be divided into two parts. The first part includes signal processing, algorithm design and experimental studies, i.e. the fields that were the main topics of this PhD thesis. The second part, although out-of-scope of the research work presented herein, is nevertheless very important and deals with all the hardware aspects of UWB-radar-based trapped-victim detection operations. The suggestions and recommendations for future work are presented below.

7.2.1 Signal processing

The effect of bandwidth on the effective down-range resolution
The experimental study on the optimal operational frequency band did not take into account how the resolvability of two or more closely spaced victims or non-stationary clutter is affected by the choice of bandwidth. Although the bandwidth of 400 MHz resulted in the highest relative SNR it does not, however, provide much information on how it affects the afore-mentioned aspects of victim detection. Therefore, another detailed experimental study should focus on investigating the lowest acceptable bandwidth centred below 1 GHz that provides sufficient resolving capabilities.

Attenuation assessment of real-life like rubble
During the course of my research studies, there were no ample opportunities to perform assessment on the attenuation of the type of rubble which is more commonly found at real-life rubble sites. This includes, for instance, randomly oriented reinforced concrete blocks of various thicknesses and shapes. Therefore, future studies should aim for attenuation assessment of more challenging and real-life-like rubble types then investigated in this thesis.

Assessment on the required dynamic range for use of two target features
One should investigate how large dynamic range is typically required for extracting both target features (i.e. respiratory- and cardiac motion) in UWB-radar-based trapped-victim detection. The study should involve real-life-like rubble and various orientations and positions of the body.

Signal processing for multi-static radar operational mode
The multi-static radar operational mode has many more advantages over the bi-static one and no disadvantages, aside from increased computational burden. In this thesis, it was shown that the detectability of a trapped victim depends, among others, on the position and on the orientation of the victim with respect to the antennas. It is therefore expected that implementing more receive

antennas with slight spacing from each other and processing the data coherently, heavily increases the probability of detection of trapped victims. Future research work should therefore develop the most efficient method for coherent processing of the acquired data sets and evaluate the optimal placement of the receive antennas and their mutual distance.

Victim localisation
A natural extension of the multi-static radar operational mode is in using the antennas for determining the exact range and location of the trapped victim. Several methods for victim localisation should be developed and their performance compared under real-life-like conditions.

Polarisation diversity
In chapter 3 it was shown that the human body produces significantly weaker cross-polarised responses than co-polarised ones. This fact can be used during the typically low SNR conditions for partial suppression of non-stationary clutter by means of cross-polarised antenna pairs. It is expected that the cross-polarised responses of non-stationary clutter will be significantly larger than those of the human body, thereby enabling the range of the non-stationary clutter to be determined. Future work should look into the ratio between cross-polarised responses of a human body and of typical non-stationary clutter.

7.2.2 Hardware design

It is expected that a significant part of the SNR improvement in UWB-radar-based trapped-victim detection operations can come from development of dedicated hardware. Of particular interest is the development of a state-of-the-art UWB radar for this purpose. A fast, highly stable, high-dynamic range system with variable transmit power and pulse repetition frequency is desired. More dynamic range is needed in order to improve the SNR conditions. The data acquisition should be much faster than for available systems since in that case higher averaging can be implemented, which results in further increase in the SNR conditions. The range and magnitude of the non-stationary clutter can vary highly depending on various conditions in the area of interest. Variable pulse repetition frequency is seen as a useful feature since it directly affects the unambiguous range. Having a long unambiguous range is advantageous since it enables range gating of the non-stationary clutter responses. However, it also reduces the highest possible averaging value and thereby SNR. Lastly, dedicated antennas with improved matching to typical rubble, low-frequency operation and low dispersion should be developed.

A

Appendix A

A.1 Time-domain impulse radar equipment

The main components of the time-domain impulse radar system that we used are: a sampling precision converter, sampling head, pulse generator main frame, pulse generator head, antennas and triggering-, RF- and data cables. Following devices can be added for increased performance: an analogue filter for out-of-band-noise- and narrowband interference suppression, low-noise amplifier for amplification of incoming electromagnetic waves and/or attenuators for decreasing the power of the generated electromagnetic waves in order not to saturate the receiver electronics. Two different types of time-domain impulse radars were used for data acquisition: a 3-channel Geozondas SD-303NF [1] and an 8-channel Geozondas SD10806 [2] time-domain precision converter. The role of a sampling precision converter is to trigger the pulse generator as well as the sampling unit. It further collects the sampled data from the sampling unit and forwards it to the PC, most commonly using a USB interface. The pulse generators that we have used consist of a pulse generator mainframe and a separate pulse generator head. A pulse generator mainframe relays the triggering pulse from the sampling converter to the pulse generator head, which fires an ultra-short electromagnetic pulse, and feeds it with power.

A.1.1 Geozondas SD-303NF digital sampling converter

Due to its high performance and state-of-the-art technology, this sampling converter was the most widely used one for data acquisition during measurements and various experiments. The specifications of the SD-303NF can be found in table A.1. The two sampling units that were used during the radar measurements are Geozondas SU-4126NF and SU-3126M, a 3- and 2-channel sampling device, respectively. Their role is to sample the incoming electromagnetic waves and forward it to the sampling converter for analogue-to-digital conversion.

A.1.2 Geozondas SD10806 digital sampling converter

Although the PRI of the SD10806 converter, and thereby the maximal practically usable value of averaging, is a factor of 20 lower than the one of the SD-303NF converter, the main advantage of SD10806 is the number of available input channels (eight), see fig. A.1(b). This allows for more antennas to be connected at the same time. The specifications of the Geozondas SD10806 digital sampling converter can be found in table A.1.

(a)

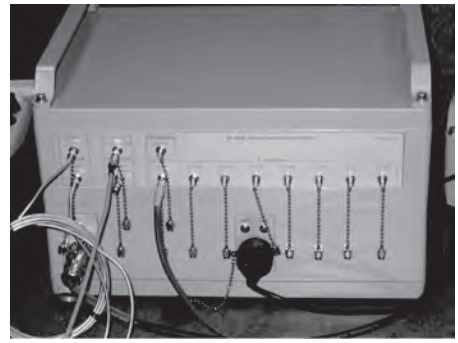

(b)

Figure A.1: *Sampling converters that were used for data acquisition: a) Geozondas SD-303NF sampling precision converter; b) Geozondas SD10806 sampling converter*

Parameter	**SD-303NF** [1]	**SD10806** [2]
Number of channels	3	8
Bandwidth	DC to 26 GHz	0.1-6 GHz
Bit resolution	12 bits	12 bits
Dynamic range	65 dB (meas.)	53 dB (meas.)
Input voltage range	±1	±1
RMS noise factor	1.2 mV (0.49 mV meas.)	1.5 mV (2.7 mV meas.)
RMS jitter	1.5 ps (0.77 ps measured)	2.6 ps (1.7 ps meas.)
Time base	0.002-10 ns/div	20 ns (max)
Time meas. accuracy	±3 ps +2%	±(10 + 0.001)ps
PRF	10 MHz (10.4 MHz meas.)	500 kHz
Number of samples	4-16384	4096 (max)
Input impedance	50±0.5 Ω	50±1 Ω
Averaging	1-4096	<1024

Table A.1: *Technical specifications for SD-303NF and SD10806 sampling converters*

Parameter	Value
Waveform	Gaussian-like (GZ1117AN); Ramp (GZ1117DN-25)
Amplitude	>40 V (GZ1117AN); >25 V (GZ1117DN-25)
Polarity	negative
Pulse width	<30 ps
Maximal PRF	10 MHz
Input impedance	50 Ω
Insertion jitter of output pulses (RMS)	<2.5 ps
Type of HF connector	SMA socket

Table A.2: *Technical Specifications for GZ1117AN [3] and GZ1117DN-25 [4]*

A.1.3 Geozondas GZ1117AN and GZ1117DN-25 pulse generator heads

External pulse generator heads GZ1117AN [3] and GZ1117DN-25 [4] operate independently or together with pulse generator mainframe GZ1105DLP (see fig. A.2(a) and fig. A.2(b), respectively) and are designed for generation of negative high-speed electrical pulses with short duration in different applications. The time domain waveform acquired using the SD-303NF, GZ1117AN and a pair of dielectric wedge antennas and its power spectral density (PSD) can be seen in fig. A.3. The technical specifications can be found in table A.2.

(a) (b)

Figure A.2: *a) GZ1117DN-25 pulse generator head; b) Pulse generator mainframe GZ1105DLP*

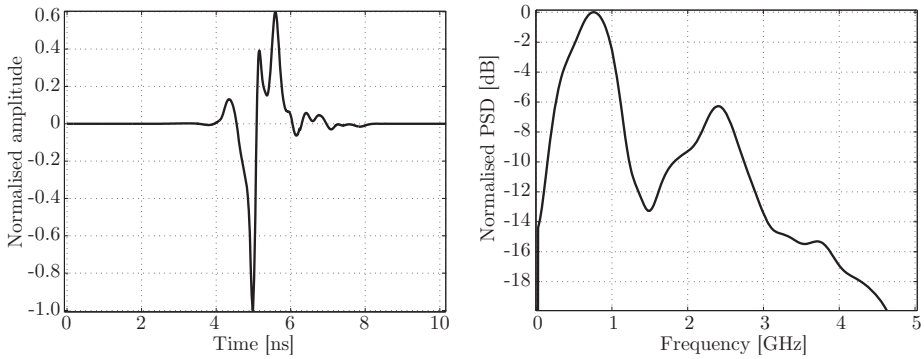

(a) (b)

Figure A.3: *a) Time domain waveform acquired using SD-303NF, GZ1117AN and a pair of DWAs; b) the normalised spectrum of the time domain waveform.*

A.2 M-sequence radar equipment

Meodat 4.5 GHz M-sequence Evaluation Kit is a two-channel pseudo-random noise radar radar having 4.5 GHz clock frequency [5], see fig. A.4(b). Its operational frequency range is from DC to 2.25 GHz and its output power is ca. 6 dBm. Its sample interval t_s= 222 ps and the number of samples per range profile $N = 511$. The communication with the PC is done using an Ethernet cable.

A.3 SFCW radar equipment

Two vector network analysers were used for two different purposes and are listed below.

A.3.1 HP 8753D

HP 8753D Vector Network analyzer [6] was used for measurements of the wall and sandstone rubble attenuation. The main motivation is its high dynamic range as well as its time- and amplitude stability. Its technical specifications are summarised bellow [6]:

- 30 kHz to 6 GHz frequency range.
- Integrated S-parameter test set.
- Integrated 1-Hz resolution synthesized source.

(a) (b)

Figure A.4: *a) Geozondas SU-4126NF sampling unit; b) Meodat 4.5 GHz M-sequence Evaluation Kit*

- Optional time-domain and swept-harmonic measurements.
- Up to 110 dB of dynamic range.
- Group delay and deviation from linear phase.

A.3.2 Agilent E8364B

This state-of-the-art vector network analyzer was only available for a short period of time. It was used only for the performance comparison to the PRN radar and the impulse radar. The specifications of this vector network analyzer can be found in [7].

A.4 UWB antennas

Three types of antennas were used for experimental verification measurements:

A.4.1 Vivaldi-type antenna

Exponential Tapered Slot Antenna (ETSA), commonly known as Vivaldi antenna, was used as transmit antenna during the detectability assessment measurements. The antenna consists of a sandwich of five dielectric layers (epoxy,

foam, duroïd, foam, epoxy). Metallic sheets are printed on both epoxy and duroïd layers, as shown in fig. A.5(a). The technical specifications of the antenna can be found in table A.3 [8] and the measured gain of the antenna in fig. A.5(b).

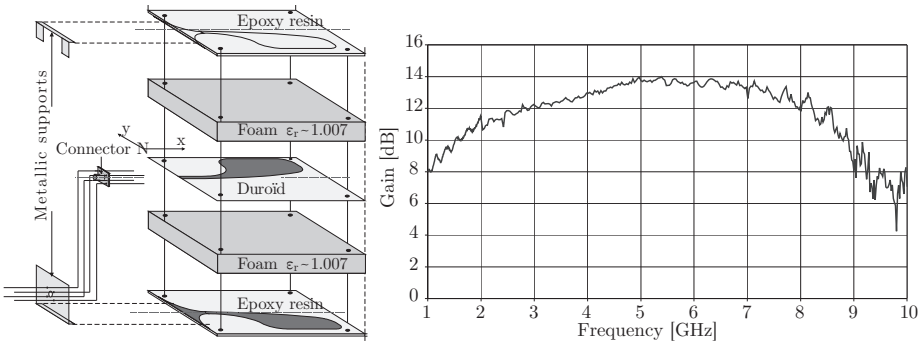

Figure A.5: *a) Structure of the Vivaldi antenna; b) Gain vs. frequency of the Vivaldi antenna*

A.4.2 Dielectric wedge antenna

A dielectric wedge antenna (DWA) [9] was most frequently used and can be seen in fig. A.6(a) with its gain vs. frequency in fig. A.6(b). The parameters of DWA can be seen in table A.3.

Figure A.6: *a) Dielectric wedge antenna; b) Dielectric wedge antenna gain vs. frequency.*

A.4.3 Double-ridged horn antenna

Two double-ridged waveguide horn antennas [10] were used for acquisition of data for the performance assessment of the respiratory motion detection algo-

Parameter	ETSA	DWA	Ridged horn
Frequency range [GHz]	0.47 - 8	0.80 - 10	0.20 2.2
Return loss (avg.) [dB]	11	15	15.5
Weight [kg]	0.3	5	15.8
Dimensions (LWH) [cm]	29.5×27×1.1	16×16×25.25	99.7×99.8×77.3
Electrical connection	SMA	SMA	N female

Table A.3: *Technical specifications for the Vivaldi (ETSA), DWA and ridged-horn antenna*

rithm as well as during the operational frequency band assessment. The used antenna is seen in fig. A.7(a) and its gain vs. frequency in fig. A.7(b). The large weight and dimensions of the antennas (see table A.3) enabled efficient radiation of frequencies down to 180 MHz, in order to decrease the overall attenuation. Due to their large dimensions, such antennas are not feasible for use in real-life scenarios, only for experimental verification. The parameters of the double-ridged horn antenna can be seen in table A.3.

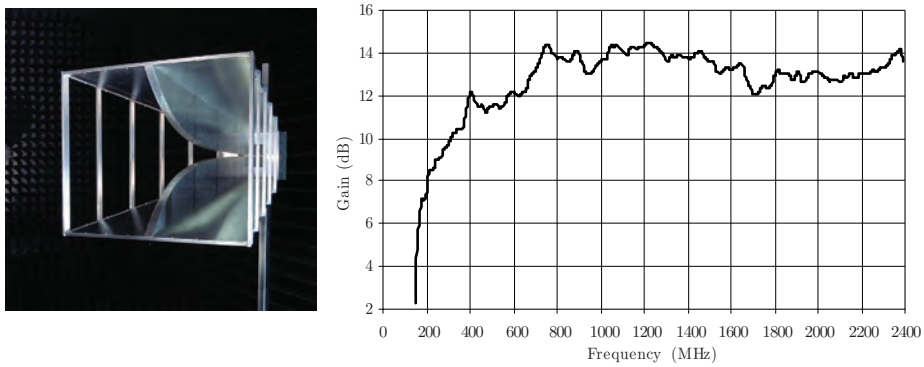

Figure A.7: *a) Double-ridged horn antenna; b) Gain vs. frequency of double-ridged horn antenna.*

A.5 Auxiliary equipment

Due to overhead in terms of dynamic range in the receiver that was often not fully used, there was a need to amplify the analogue signal before digitisation, thus resulting in significantly higher SNR conditions. The amplification was done by means of a high-end LNA (Miteq, model AFS4-00101200-22-10P-4 [11]) having 30±2 dB gain (measured) in the frequency band of interest. However, since the LNA has an invariable gain, there was often a need to use attenuators (typically 6 dB) in order not to overload the receiver circuitry. In certain

situations we faced strong interference at the low frequency range of the used receive antennas (at ca 170 MHz), that was even able to propagate thick concrete walls. This prompted us to use a high-end analogue high-pass filter (Mini Circuits, model SHP-400 [12]) that has a -3dB cut-off frequency at 360 MHz. By doing so, not only strong narrowband interference was removed, but also a significant amount of low-frequency noise, while at the same time not significantly affecting the waveform of the backscattered response from the victim.

B
Appendix B

B.1 Proof of equation 5.16 in paragraph 5.7.1

A $j^{\dagger}$-th singular matrix $\mathbf{D}_{j^{\dagger}}[n,\kappa] = \mathbf{D}_{j^{\dagger}}$ is obtained by:

$$\mathbf{D}_{j^{\dagger}} = \lambda_{j^{\dagger}} \cdot \mathbf{u}_{j^{\dagger}} \cdot \mathbf{v}_{j^{\dagger}}^{H}$$

Assuming AWGN, the singular vectors $\mathbf{u}_{j^{\dagger}} \in \mathcal{N}(0,\sigma_u)$ and $\mathbf{v}_{j^{\dagger}} \in \mathcal{N}(0,\sigma_v)$, where σ_u and σ_v are the standard deviation of the vectors $\mathbf{u}$ and $\mathbf{v}$, respectively. Since $\mathbf{u}$ and $\mathbf{v}$ have unitary energy, i.e. $\sum_{k=1}^{K_m} \mathbf{u}_k^2 = 1$ and $\sum_{n=1}^{N} \mathbf{v}_n^2 = 1$, leads to $\sigma_u = 1/\sqrt{K_m}$ and $\sigma_v = 1/\sqrt{N}$. The values in $|\mathbf{D}| = \left|\mathbf{u}_j \cdot \mathbf{v}_j^H\right|$ have been found to be distributed according to the exponential distribution with mean:

$$\mu_{|D|} = \sqrt{2/\pi} \cdot \sigma_u \sigma_v = \frac{2}{\pi\sqrt{K_m \cdot N}}$$

The scaling factor $\sqrt{2/\pi}$ originates from the fact that the mean of a half-normal-distributed variable (absolute value of a zero-mean normally distributed variable) is $\sqrt{2/\pi}$ for unit standard deviation. The threshold γ is obtained from the inverse survival function [13] of the exponential distribution function: $\gamma = -\mu \log\left\{P_{j^{\dagger},fa}\right\}$. If J singular matrices are considered as decision matrices, than the probability of false alarm for each singular matrix is $P_{j^{\dagger},fa} = P_{fa}/J$, where P_{fa} is the total probability of false alarm. Ultimately, the threshold needs to be scaled by the respective singular value $\lambda_{j^{\dagger}}$, thus obtaining:

$$\gamma_{j^{\dagger}} = -\lambda_{j^{\dagger}} \cdot \frac{2 \cdot \log(P_{fa}/J)}{\pi \cdot \sqrt{N \cdot K_m}}$$

References

[1] Geozondas. SD-303NF digital sampling precision converter. [Online]. Available: http://www.geozondas.com/Sd203/SD203.htm

[2] ——. Digital sampling converter SD10806. [Online]. Available: http://www.geozondas.com/SD10806/SD10806.htm

[3] ——. External pulse generator unit GZ1117AN. [Online]. Available: http://www.geozondas.com/Pulse_Gen_New/Units/Pulse_Generator_Unit_GZ1117AN.htm

[4] ——. External pulse generator unit GZ1117DN-25. [Online]. Available: http://www.geozondas.com/Pulse_Gen_New/Units/Pulse_Generator_Unit_GZ1117DN-25.htm

[5] M. GmbH. UWB 9GHz Evaluation Kit. [Online]. Available: http://www.meodat.com/publications/UWB_EvalKit.pdf

[6] H. Packard Company, *User's Guide HP 8753D Network Analyzer*, December 1997. [Online]. Available: http://cp.literature.agilent.com/litweb/pdf/08753-90257.pdf

[7] Agilent Technologies Inc., *Agilent PNA Microwave Network Analyzers*, February 2009. [Online]. Available: http://cp.literature.agilent.com/litweb/pdf/5988-7988EN.pdf

[8] E. Guillanton, J. Y. Dauvignac, C. Pichot, and J. Cashman, "A new design tapered slot antenna for ultra-wideband applications," *Microwave and Optical Technology Letter*, vol. 19, 1998, pp. 286–289.

[9] A. Yarovoy, L. Ligthart, A. Schukin, and I. Kaploun, "Dielectric wedge antenna for ground penetrating radar," vol. 2, Jun. 2003, pp. 247–250.

[10] RFspin s.r.o. Model DRH200 Double Ridged Waveguide Horn. [Online]. Available: http://www.rfspin.cz/en/antennas/drh200.php

[11] M. Inc., *Miteq AFS4-00101200-22-10P-4*, Apr. 2008. [Online]. Available: http://amps.miteq.com/datasheets/01-12_01.PDF

[12] Mini-Circuits, *Coaxial High Pass Filter SHP-400+*. [Online]. Available: http://www.minicircuits.com/pdfs/SHP-400+.pdf

[13] "Related distributions: Inverse survival function," NIST/SEMATECH e-Handbook of Statistical Methods, 2003. [Online]. Available: http://www.itl.nist.gov/div898/handbook/eda/section3/eda362.htm

Summary

Rescue dogs are commonly used during the urban search-and-rescue (USAR) operations for the initial indication on the presence of trapped victims after the collapse of man-made structures. However, dogs are not able to inform the rescue crews whether the trapped victims are alive or not and where exactly they are located. Other complementary tools, such as acoustic- and audio-visual equipment, are prone to inaccuracy, interference and inadequate range of operation. Ultra-wideband (UWB) radar is considered a promising tool for more exact assessment on the range of trapped victims. However, implementation of UWB radar for trapped-victim detection faces challenges such as low signal-to-noise ratio (SNR) conditions, interference from non-stationary clutter, residues due to amplitude instability originating in the equipment as well as narrowband radio interference. There are four commercially available UWB radar technologies and it is not clear which radar technology is the most suited one for the purpose of detecting trapped victims. There is very little available knowledge on the two target features that enable detection of a trapped human body using radar (respiratory- and cardiac motion). In need of further investigation is the choice of the optimal operational frequency band as well as assessment on the amount of attenuation of a few obstacles that represent, to various accuracy, real-life rubble.

Chapter 2 introduces the reader with the basic principles of generation, sampling and pre-processing of UWB signals for the four available UWB radar technologies. It investigates the applicability of two time-domain- and the continuous-wave (CW) UWB radar technology for the purpose of trapped-victim detection, both based on the inherent properties as well as by means of an experimental verification study evaluated under as similar measurement conditions as possible. The results of both the theoretical and experimental verification indicate that the CW UWB radar technology is to prefer over the time-domain radar technologies due to generally higher dynamic range, better use of the designated spectrum and higher transmit power as well as that it enables the extraction of two target features, as opposed to only one (respiratory motion). The study is not definitive nor final and should serve as guidelines for further studies and/or system design.

Chapter 3 investigates in detail the time-domain and frequency-domain behaviour of the two available target features for various body positions. It shows that the respiratory motion responses are in average 13 dB stronger than the cardiac motion responses. The position such that the chest is turned toward the receive antenna produces strongest respiratory motion responses due to larger chest displacement and reflective area than the other positions. Detectability of respiratory motion responses as function of aspect angle was investigated under line-of-sight conditions for three body positions, four bi-static angles and three antenna-pair polarisations using a single test person. It showed that there is no considerable difference in detectability among the investigated bi-static angles

and co-polarised antenna pairs. However, it was concluded that cross-polarised antenna pairs should be avoided in real life as they produce significantly lower detectability values.

The attenuation as function of frequency of two types of obstacles (piles of sandstone blocks and a 60-cm concrete wall) was investigated in chapter 4. The results show that the attenuation for both materials is ca 10-15 dB across the frequency range of interest. However, realistic rubble thicknesses and types of rubble can heavily increase the attenuation and thereby lower the probability of detection. Measurements involving a test person resting under 80-cm concrete rubble pile and behind two concrete walls, showed that the centre frequency well below 1 GHz gives rise to highest SNR values. Bandwidths of ca. 400 MHz centred at frequencies below 1 GHz give rise to higher SNR values than larger investigated bandwidths. On the hand, lower bandwidths result in poorer down-range resolution, which is necessary for resolving non-stationary clutter responses or multiple trapped victims.

One of the fundamental tasks of this thesis is the development of a respiratory motion detection algorithm. Chapter 5 details a novel and computationally efficient algorithm which is able to improve SNR conditions and better suppress non-stationary clutter compared to an existing algorithm, assessed both experimentally and in a simulated environment. The algorithm further incorporates a threshold which aids in the decision making process by the operator. The performance of three common stationary-clutter suppression methods is investigated on a single measured data set containing respiratory motion and linear amplitude instability (linear trend). It was shown that the linear-trend removal method, which removes any potential linear trend and DC level in the slow-time dimension, is the preferred approach to stationary-clutter suppression.

Narrowband interference (NBI) results in increase of noise floor and thereby worsens the probability of detection, when using stroboscopic sampling (such as in impulse radar). Chapter 6 analyses the performance of four developed methods for NBI suppression implemented in stroboscopic samplers. The most suitable method for NBI suppression in stroboscopic samplers is to filter out the NBI in the analogue domain and, after sampling, implements linear interpolation of the missing spectrum in order to avoid ringing of the backscattered waveforms from the victim, is regarded the most suitable method. It shows an improvement factor of 12.9 dB in noise reduction and manages to preserve the signal waveform and energy very well.

The thesis is completed by the conclusions and recommendations for future studies.

Samenvatting

Reddingshonden worden gewoonlijk gebruikt tijdens de zoek- en reddingsoperaties (USAR operaties) in stedelijk gebied voor verkrijgen van eerste indicaties over de aanwezigheid van opgesloten slachtoffers na de ineenstorting van door mensen gemaakte objecten. Echter, honden zijn niet in staat om de reddingsteams te informeren of de opgesloten slachtoffers nog in leven zijn of niet en waar zij zich precies bevinden. Andere aanvullende instrumenten, zoals akoestische- en audiovisuele apparatuur, hebben tijdens reddingsoperaties onnauwkeurigheden en onvoldoende bereik en zijn interferentie gevoelig. Ultrabreedband (UWB) radar wordt beschouwd als een veelbelovend instrument voor meer precieze schatting van de afstand tot de opgesloten slachtoffers. Echter, om UWB radar voor de detectie van de opgesloten slachtoffers in te zetten moeten eerst uitdagingen zoals lage signaal-ruisverhouding (SNR) condities en interferentie afkomstig van niet-stationaire clutter worden aangepakt, alsmede de residuen als gevolg van amplitude instabiliteit afkomstig van de apparatuur en van smalband radio-interferentie. Er zijn vier commercieel beschikbare UWB radartechnologien en het is niet duidelijk welke radartechnologie het meest geschikt is voor de opsporing van opgesloten slachtoffers. Er is heel weinig kennis beschikbaar over twee beoogde functies (ademhaling, hartslag), waarmee detectie van een onder puin opgesloten persoon met behulp van radar mogelijk wordt. Vanwege de noodzaak voor nader onderzoek is het van belang om tot een juiste keuze te komen voor een optimale operationele frequentieband alsmede een evaluatie te maken van de demping van radargolven veroorzaakt door de aanwezige obstakels en van de uiteindelijke meetnauwkeurigheid, met andere woorden van het echte puin na het instorten van gebouwen.

Hoofdstuk 2 introduceert het belang van basisprincipes, het opwekken van de zendsignalen, het bemonsteren en het pre-verwerken van UWB signalen voor de vier beschikbare UWB radartechnologien. De toepasbaarheid van de tijd-domein en de 'continuous wave' (CW) UWB radartechnologie wordt onderzocht met als doel het opgesloten slachtoffer te detecteren. Beide technologien krijgen aandacht op basis van hun inherente eigenschappen evenals door het uitvoeren van een experimentele verificatiestudie waardoor evaluatie onder zo veel als mogelijk vergelijkbare meet omstandigheden mogelijk wordt. Uit de resultaten van zowel de theoretische als de experimentele verificatie blijkt dat de CW UWB radar-technologie is te verkiezen boven de tijd-domein radar technologie. Dit komt door een groter dynamisch bereik, een beter gebruik van het toegewezen frequentie spectrum en een hoger zendvermogen, maar ook omdat de extractie van twee eigenschappen van de te meten persoon mogelijk wordt. Dit laatste in tegenstelling tot het meten van slechts een eigenschap (zoals bij meting van alleen ademhalingsbeweging). Deze studie is nog niet afgerond, maar kan dienen als leidraad voor verdere studies en / of systeemontwerpen.

In Hoofdstuk 3 wordt het tijd-domein en frequentie-domein gedrag van de twee beschikbare karakteristieke eigenschappen van de te meten persoon voor

verschillende lichaamposities in detail onderzocht. Het blijkt dat de bewegingsreacties bij de ademhaling gemiddeld 13 dB sterker zijn dan de bewegingreacties van het hart. De positie met de borstkas in de richting van de antenne produceert de sterkste ademhalingsreacties. Dit komt omdat de borstverplaatsing en het reflecterende oppervlakte voor deze positie groter is dan bij andere posities. Detecteerbaarheid van ademhalingsreacties als functie van de aspecthoek is onderzocht onder 'direct radar zicht' condities voor drie lichaamposities, vier bi-statische hoeken en drie antennepolarisatie combinaties. De metingen zijn verricht aan een enkele proefpersoon. Daaruit is gebleken dat er geen aanzienlijk verschil is gemeten in detecteerbaarheid voor de onderzochte bi-statische hoeken en voor verschillende polarisaties in geval er gelijke polarisaties (co-polar) in de antenne paren worden toegepast. Echter, de conclusie is dat orthogonale polarisaties (cross-polar) in de antenne paren vermeden moeten worden bij echte toepassingen, omdat dan reflectie waarden worden gemeten met beduidend lagere detecteerbaarheid.

De demping als functie van de frequentie van twee typen obstakels (palen van zandsteen blokken en een 60-cm betonnen muur) is onderzocht in hoofdstuk 4. De resultaten tonen aan dat de demping voor beide materialen ca. 10-15 dB bedraagt over het frequentiebereik van belang in UWB radar. Echter, realistische puin diktes en puin typen kunnen de demping sterk verhogen en daardoor de kans op detectie verlagen. Uit metingen, waarbij een proefpersoon zich onder een 80-cm betonnen paal van puin en achter twee betonnen muren bevindt, is gebleken dat voor centrale frequenties beduidend lager dan 1 GHz de hoogste SNR waarden worden verkregen. Bandbreedtes van ca. 400 MHz rondom centrale frequenties beneden 1 GHz geven hogere SNR waarden dan grotere onderzochte bandbreedtes. Evenwel, de lagere bandbreedtes resulteren in slechtere afstands(diepte-)resolutie nodig voor het herkennen van niet-stationaire clutter responsies of voor het onderscheiden van meerdere opgesloten slachtoffers.

Een van de fundamentele opgaven van dit proefschrift is de ontwikkeling van een bewegingsdetectie-algoritme van de ademhaling. Hoofdstuk 5 geeft in detail een nieuw en rekentechnisch-efficint algoritme dat in staat is om SNR condities te verbeteren en een betere niet-stationaire clutter onderdrukking te realiseren; dit in vergelijking met een bestaand algoritme. Bovendien is het nieuwe algoritme beoordeeld zowel experimenteel als in een gesimuleerde omgeving. Het algoritme bevat verder een drempel die helpt bij de besluitvorming door de radar operator. De prestaties van drie algemene stationaire-clutter onderdrukkingsmethoden worden onderzocht op een enkelvoudig gemeten dataset waarin aanwezig zijn ademhalingsbewegingen en lineaire amplitude instabiliteiten (d.w.z. een lineair verlopende trend). Er is aangetoond dat de methode voor verwijdering van alle lineaire trends en langzame veranderingen in het DC-niveau de beste aanpak is voor stationaire-clutter onderdrukking. Smalbandige interferentie (NBI) leidt tot een toename van de ruis 'vloer'; daardoor verslechtert de detectiekans bij het gebruik van stroboscopische bemonstering (zoals in

impuls radar).

Hoofdstuk 6 analyseert de prestaties van de vier ontwikkelde methoden voor NBI onderdrukking uitgevoerd in stroboscopische monsternemers (samplers). De meest geschikte methode voor NBI onderdrukking in stroboscopische samplers is de NBI uit te filteren in het analoge domein en lineaire interpolatie van het dan ontbrekende spectrum toe te passen na bemonstering. Dit wordt gedaan om signaalverlenging van de terugverstrooide golfvormen afkomstig van het slachtoffer te voorkomen. De methode toont een verbetering in ruisonderdrukking van 12,9 dB. Verder is de methode in staat de signaal golfvorm en de energie goed te houden.

Het proefschrift wordt afgesloten met conclusies en aanbevelingen voor toekomstige studies.

List of Abbreviations and Symbols

Abbreviations

AD	-	Analogue-to-Digital (conversion)
AWGN	-	Additive White Gaussian Noise
CW	-	Continuous Wave
DFT	-	Discrete Fourier Transform
EandS	-	Estimate-and-Subtract
EandS-LSE	-	Estimate-and-Subtract Least-Squares Estimate
FandR	-	Filter-and-Restore
FandR-LI	-	Filter-and-Restore Linear Interpolation
FCC	-	Federal Communications Commission
FDTD	-	Finite-Difference Time-Domain
FIR	-	Finite Impulse Response
FMCW	-	Frequency Modulation Continuous Wave
HH	-	Horizontal-Horizontal (antenna co-polarisation)
HV	-	Horizontal-Vertical (antenna cross-polarisation)
IDFT	-	Inverse Discrete Fourier Transform
IF	-	Intermediate Frequency
LNA	-	Low-Noise Amplifier
LOS	-	Line-of-Sight
NBI	-	NarrowBand Interference
NLOS	-	Non-Line-of-Sight
PRF	-	Pulse Repetition Frequency
PRI	-	Pulse Repetition Interval
PRN	-	Pseudo-Random Noise
RF	-	Radio Frequency
RMD	-	Respiratory Motion Detection
SAR	-	Synthetic Aperture Radar
SFCW	-	Step-frequency continuous wave
SME	-	Small and Medium Enterprises
SNR	-	Signal-to-Noise Ratio
SNCR	-	Signal-to-Noise-and-Clutter Ratio
SNIR	-	Signal-to-Noise-and-Interference Ratio
SVD	-	Singular Value Decomposition
TUD	-	Delft Technical University
USAR	-	Urban Search-And-Rescue
USB	-	Universal Serial Bus
USGS	-	United States Geological Survey
UWB	-	Ultra-Wideband
VNA	-	Vector Network Analyzer
VH	-	Vertical-Horizontal (antenna co-polarisation)
VV	-	Vertical-Vertical (antenna co-polarisation)

Scalars

δt	-	Time resolution.
ϵ_r	-	Relative permittivity of the obstacle.
ϕ_h	-	Human respiratory motion phase.
γ	-	CFAR threshold.
κ	-	Slow-time frequency index.
κ^*	-	Fixed, lowest index of κ within $\boldsymbol{\nu}[\kappa]$.
λ_j	-	Singular value of the j-th singular matrix.
μ	-	Fast-time frequency index.
θ_a	-	Aspect angle.
θ_b	-	Bistatic angle.
τ_m	-	Time-of-arrival of the m-th multipath reflection.
$\Delta\phi$	-	Phase difference.
Δf	-	Frequency step in PNA.
Δn^*	-	Difference in time-of-arrival of the target response.
Δt	-	Time difference.
ΔR	-	Chest displacement.
a	-	Scaling factor.
a_h	-	Human respiratory motion amplitude.
c_0	-	Speed of light.
c_m	-	Speed of the electromagnetic pulse in the propagation medium.
f_a	-	Acquisition frequency.
f_b	-	Beat frequency.
f_c	-	Centre frequency.
f_d	-	Discrete frequency.
f_h	-	Human respiratory motion frequency.
f_s	-	Effective sampling frequency.
j^*	-	Index of the matrix containing respiratory motion response.
$j^\dagger$	-	Index of the decision matrices.
k	-	Index of an averaged range profile.
l	-	Index of an acquired range profile.
m	-	Index of a reflected multipath.
n	-	Index of samples in fast time.
n^*	-	Index of the range bin of the human target response.
p	-	Antenna-pair polarisation.
r	-	Range.
r^*	-	Physical range of the victim to the antenna.
r_{max}	-	Unambiguous range.
r'	-	Physical range of the scatterers outside r_{max} appearing at r^*.
$s(t)$	-	Pulse train.
t_s	-	Effective sampling time.
$u(t)$	-	Generated pulse.
v	-	Index of the reflected multipath from the victim.

B - Operational bandwidth.
B_i - Bandwidth of the narrowband interference.
E_{diff} - Preservation of signal energy.
E_{rc} - Respiratory-to-cardiac-motion-response energy ratio.
H_0 - Null hypothesis.
H_1 - Alternative hypothesis.
J - Number of considered singular matrices.
K - Number of acquired range profiles.
K_m - Size of $\boldsymbol{\nu}[\kappa]$.
J - Number of singular values.
L - Averaging value.
M - Number of multipaths.
N - Number of samples per range profile.
N^* - Size of the human target response.
N_v - Range bin size.
P_d - Probability of detection.
P_{fa} - Probability of false alarm.
R - Amount of NBI suppression.
R_{ring} - Amount of ringing suppression.
T - Pulse repetition interval.
T_a - Acquisition time.
T_h - Human respiratory motion period.
T_{obs} - Observation time.
T_s - Sample point.
T_w - Time window.
W - Preservation of waveform factor.

Vectors
$\boldsymbol{\delta}[k]$ - Respiratory motion in slow-time dimension.
$\boldsymbol{\nu}[\kappa]$ - Rectangular window in the slow-time frequency domain.
$\boldsymbol{\theta}[\kappa]$ - Non-stationary clutter response.
$\boldsymbol{\Psi}[k, K]$ - Compensation term for the linear trend.
$\mathbf{c}[n]$ - Stationary clutter.
$\mathbf{h}^*[n]$ - Human target response.
$\breve{\mathbf{h}}^*[n]$ - Respiratory motion response.
$\mathbf{h}_n^{*fd}[\kappa]$ - Respiratory motion response in the slow-time frequency domain.
$\mathbf{i}[n]$ - Sampled narrowband interference.
$\mathbf{r}_l[n]$ - l-th sampled range profile.
$\bar{\mathbf{r}}_k[n]$ - k-th averaged range profile.
$\mathbf{u}_k$ - Left singular vector.
$\mathbf{v}_n$ - Right singular vector.
$\mathbf{w}[n]$ - Additive white Gaussian noise.
$\mathbf{D}[\theta_a]$ - Detectability of human respiratory motion.

Matrices

$\mathbf{\Lambda}$	-	Stretcher matrix.
$\mathbf{H}$	-	Resulting data matrix after SVD.
$\mathbf{R}$	-	Data matrix.
$\mathbf{U}$	-	Hanger matrix.
$\mathbf{V}$	-	Aligner matrix.

List of Figures

List of Tables

Biography and list of publications

Amer Nezirović was born in Doboj, Bosnia and Herzegovina in 1980. He attended secondary school in the field of mathematical- and natural sciences first in Norrköping and later Stockholm, Sweden.

In 2005, he received the M.Sc. degree in electrical engineering from the Royal Institute of Technology in Stockholm, Sweden. The topic of his M.Sc. studies was digital wireless communications and signal processing. In 2003, as part of a project course in communication theory and signal processing, his group was awarded the 2003 Nokia Prize for its implementation and successful demonstration of a MIMO system. During the spring semester of 2004, he was an Erasmus exchange student with Delft University of Technology in The Netherlands, where his interest in ultra-wideband technology arose. The topic of his M.Sc. thesis was investigation of appropriate modulation and forward error correcting schemes in UWB impulse radio.

Between March 2005 and March 2009 he was formally working toward the Ph.D. degree in the field of detection of trapped human beings in post-disaster scenarios using UWB radar in the International Research Centre for Telecommunications and Radar, Delft University of Technology. The focus of the PhD studies was on development and improvement of experimental methods for detecting trapped victims buried under rubble using UWB radar.

His interests are UWB radar signal processing, UWB wireless communications (physical layer), as well as detection and probability theory. He is a student member of the IEEE society since 2006.

Publications

- Nezirovic, A., Yarovoy, A.G., Ligthart, L.P.; *Signal Processing for Improved Detection of Trapped Victims Using UWB Impulse Radar*; *(to be published in the IEEE Transactions on Geoscience and Remote Sensing in the April or May issue of 2010.)*.

- Nezirovic, A., Tesfay, S., Amaldoss, S.E., Yarovoy, A.G.; *Experimental Study on Human Breathing Cross Section using UWB Impulse Radar*; EuRAD 2008, Oct. 2008.

- Harmer, D., Yarovoy, A.G., Schmidt, N., Witrisal, K., Russell, M., Frazer, E., Bauge, T., Ingram, S., Nezirovic, A., Lo, A., Xia, L., Kull, B., Dizdarevic, V.; *An Ultra-Wide Band Indoor Personnel Tracking System for Emergency Situations (Europcom)*; EuRAD 2008, Oct. 2008.

- Harmer, D., Russell, M., Frazer, E., Bauge, T., Ingram, S., Schmidt, N., Kull, B., Yarovoy, A., Nezirovic, A., Xia, L., Dizdarevic, V., Witrisal, K.; *EUROPCOM: Emergency Ultrawideband RadiO for Positioning and COMmunications*; ICUWB 2008. Sept. 2008, pp. 85-88.

- Nezirovic, A., Damen, I.J.P., Yarovoy, A.G.; *Narrowband Interference Suppression in UWB Impulse Radar for Human Being Detection*; ICUWB 2007, Sept. 2007, pp. 56-61.

- Nezirovic, A., Yarovoy, A.G., Ligthart, L.P.; *Experimental Verification of Human Being Detection Dependency on Operational UWB Frequency Band*; ICUWB 2007, Sept. 2007, pp. 305-310.

- Nezirovic, A., Liu, M., Yarovoy, A.G.; *Modelling of reflections of uwb pulses from trapped human beings*; Ultra-wideband, short-pulse electromagnetics, 8; 2007, pp.227-232.

- Nezirovic, A., Yarovoy, A.G., Ligthart, L.P.; *Experimental study on human being detection using UWB radar*; IRS 2006; May 2006, pp.1-4.

Acknowledgments

As with any large undertaking or venture carried out by a single individual, so were my doctorate studies influenced and affected by a number of other individuals. I would hereby like to express my gratitude to those who in one way or another have helped me along this long and somewhat winding road toward a PhD degree.

Firstly, I would like extend my deepest gratitude to my supervisor and co-promoter, Prof. Alexander Yarovoy, whom I first met during my Erasmus studies at TU Delft in 2004. Towards the end of a course in ultra-wideband technology that he was giving, he spotted in me a potential PhD candidate for a position at the IRCTR. He offered me the position on victim search, an action which I found very flattering and encouraging, and the PhD position which I would eventually accept. Naturally, this would not have occurred had not Prof. Leo P. Ligthart, the head of the IRCTR at the time and my subsequent promoter, agreed to grant the position to me. I feel very fortunate to have conducted my research studies under the promotership of Prof. Ligthart and supervision of Prof. Yarovoy, both highly regarded figures in their fields. My sincerest thanks go to both of them for believing in me and supporting me along the track. I feel very blessed to have gotten the opportunity to work on a topic with such a high humanitarian value.

There are a number of individuals who have not been directly involved with my research studies, but who have, nevertheless, had strong influence on the outcome of my studies. I would like to extend a big thanks to Pascal Aubry, but also the other technicians in the IRCTR, who were always very helpful and happy to help. Even though they were probably one of the most sought-after staff members of the IRCTR, they managed somehow to squeeze you into their busy schedule and provide the much needed help. Pascal, thanks for acting as a test person on so many occasions and spending so many hours with me doing the measurements down in the noisy and yellowishly-dusty cellar of the EWI building. Our lives might become a few minutes shorter due to that, but we can live with the hope that those efforts might one day help save and prolong other people's lives. Thanks to the lovely members of the IRCTR secretariat for their assistance with certain matters, which would in contrary have taken tremendous effort to get done. For all the suggestions and discussions that I have had on tough problems during my studies a big thanks goes to Timofey Savelyev, Seva Kovalenko, Zoubir Irahhauten, Ludvík Lidický, Oleg Krasnov and others from the IRCTR, as well as Michael Newman from TRT UK, David Daniels from ERA Technologies and the victim-search measurements group in the Radiotect project. I need to further express my gratitude to the following M.Sc. students that I have mentored and that have helped me to various degrees in my work: Imre Damen, Solomon Tesfay, Shenario Ezhil Amaldoss,

Sorina Baldea and Mingying Liu. Thanks also to those newspapers, radio- and TV stations for their coverage of the demonstration of my research work, as well as the marketing officials from TU Delft for helping out. This paragraph would not be complete if I would not acknowledge the frequent interactions and lovely, long discussions that I have had throughout the years with my former office mates Massimiliano Simeoni, Alexander Vorobyov and Diego Caratelli. Thanks for being such great colleagues, sharing with you your thoughts, but not the least, for replenishing my frail knowledge on antenna theory.

Obviously, my life in Delft was not only about research. There was also some beer drinking involved. A big shout-out goes to the IRCPR crew and the traditional Wednesday after-works in the city centre. That's a fantastic habit that we had and which should be kept alive and nurtured by future generations of PhD students at the IRCTR. And not to mention the even stronger tradition that we maintained of enjoying an Italian-style coffee after lunch. *Grande ragazzi (e ragazza)!* Now that I've come to the point of mentioning all the lovely people that I've met and became friends with in The Netherlands, I don't want to step into the typical trap of listing everyone by name and thereby risking not to mention someone. Instead, I'll just mention some keywords and hopefully you'll recognise yourselves: climbing (Monte Cervino, The Globe, France, Luxembourg), beers (Beestenmarkt, Dourak), trips (Berlin, Prague, Central & Eastern Europe, Croatia, Bosnia), Easter lunches, Mladi BiH, wine tasting, parties (with themes), BBQs, bike trips and many, many more events that bring back happy memories. Thanks a bunch, guys!

I cannot finish the acknowledgments without mentioning my family, as well as my relatives, for their unconditional love and support during all these years, and in particular during the time that I was unemployed. I don't know what I would've done without your support. Words written on this sheet of paper are not enough to show my love and gratitude. Thanks from the bottom of my heart.

Amer Nezirović,

January 18, 2010,
Stockholm.